Materials Advances

Accepted Manuscript

This article can be cited before page numbers have been issued, to do this please use: R. khaki, M. Moradi, G. H. Bordbar, H. Kazemi, S. Davatolhagh and M. Pazoki, *Mater. Adv.*, 2025, DOI: 10.1039/D5MA00876J.

ROYAL SOCIETY OF CHEMISTRY

rsc.li/materials-advances

View Article Online
DOI: 10.1039/D5MA00876J

Data availability

Data availability is not applicable to this article as no new data were created or analyzed in this study.

View Article Online
DOI: 10.1039/D5MA00876J

Bismuth Selenide Topological Insulator Materials for Green Energy Devices: Prospects and Applications

Razieh Khaki, Mahmood Moradi, Gholam Hossein Bordbar, Hana Kazemi, Saeid Davatolhagh and Meysam Pazoki**

Physics Department, College of Sciences, Shiraz University, Shiraz 71946-84795, Iran.

ABSTRACT

Bismuth selenide topological insulator material emerged as prototype three-dimensional topological insulator and have been the center of attention for the new generation related devices. Theoretical and experimental characterization of underlying physical phenomena together with proper evaluation of the current picture is essential to design, foresee and engineer Bi_2Se_3 for important realized device applications. Furthermore, these and presented characterization methodologies can be adopted for similar three-dimensional topological insulator counterpart materials such as bismuth telluride and antimony selenide. Herein, we summarize recent research advancements on bismuth selenide both theoretically and experimentally and drawing a perspective for future applications i.e. in spintronic and quantum computing devices as well as other green energy based scientific accomplishments. Different synthesis methods, physical properties and occurrence of quantum mechanical phenomena, and calculations, device applications and characterization methods implemented for bismuth selenide so far are classified and comprehensively reviewed. Future prospects addressing the challenges and opportunities are highlighted at the end.

Keywords: Bismuth Selenide, Bi_2Se_3, Topological Insulator, Device Application, Device Characterization

View Article Online
DOI: 10.1039/D5MA00876J

Table of Contents

DOI: 10.1039/D5MA00876J

. Introduction

Emerging materials pave the routes for the advancement of health and wealth in our future life wherein new qualifications are needed based on our demands. Nanostructured functional materials and topological insulators are among examples of materials where one can engineer the properties and reach specific potential capabilities that have been absent previously. Recently emerged topological insulator materials family have shown quantum phenomena such as spin- polarized sensing and quantum spin Hall effect, anomalous Hall effect and Majorana fermions, along with their special optoelectronic properties making them candidates for near-future quantum computing, sensing, detecting and other device applications. Here, to develop the related technologies, extend and engineer the material properties and design new device efficiencies, one needs to deeply lucubrate the fundamentals of topological insulator physical properties with the help of quantum calculations and experimental material/device characterization techniques. Bismuth selenide is an important example presenting a prototype from the three-dimensional topological insulator family which is mostly investigated so far and is the topic of the present article. Mazumder and Wang in separate review articles [1,2] investigated and collected the data from recent experimental efforts considering bismuth selenide, material synthesis and applications. However, the aim of current manuscript is to present an extensive perspective review wherein one can find the theoretical basis and the connections to experiment, quantum calculations and experimental device characterizations together with the above mentioned which are still missing and herein we aim to present such a picture. In section two an introduction about bismuth selenide will be presented, section three investigates the quantum mechanical phenomena and fundamentally interesting experiments related to future quantum computing and spintronics. Section four is devoted to density functional theory (DFT) calculations and understanding the experimental data from ab-initio calculations. Material synthesis, characterization methods, device applications and their drawback/benefits are presented in section five, six and seven, respectively. The final comments and concluding remarks come at the end in section eight. Scheme 1 illustrates a schematic summary sketch from the scientific questions presenting and discussing in the current work based on the current research status to draw and present a picture.

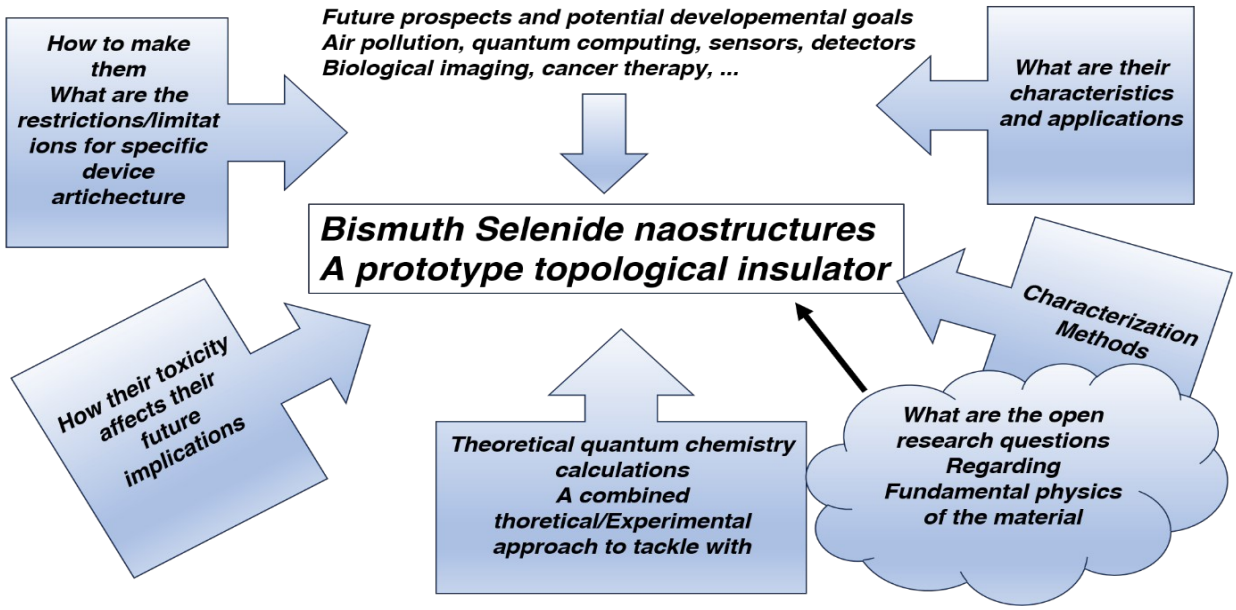

Scheme 1. A summary sketch of the outline and mentioned aims.

View Article Online
DOI: 10.1039/D5MA00876J

2. Bismuth Selenide

Bismuth selenide is a semiconductor with bandgap 0.3 eV which has been known as a prototype 3-dimensional topological insulator and have been the centre of attention for quantum mechanical studies for topological insulators since many years as the most investigated one so far. Here selenium vacancies are thermodynamically favourable in the growth making it as a n-type semiconductor with excess electron charge carriers. The bulk electronic structure shows insulating behaviour with a narrow band gap and topologically protected surface states (a Dirac cone within the bandgap electronic structure) behave as metallic. Although it was theoretically predicted earlier, experimental observation of this Dirac cone in electronic structure was evidenced in 2009 [3]. Since then, many quantum mechanical phenomena such as quantum spin Hall effect, quantum anomalous Hall effect, Majorana fermions, and spin-momentum locking evidenced. As a consequence, the recent ongoing research continues for the advancement of future spintronic and quantum computing devices.

3D topological insulators are very decent thermoelectric materials, and the first studies on bismuth selenide and its alloy with its counterpart bismuth telluride, Bi_2Te_3, [4] were devoted to thermoelectric applications. Therefore, different synthesis approaches for single crystals, bulk and nanostructures have been pursued (section 5) and at the same time material characterization (section 6) studies on Bi_2Se_3 comes to accomplish device fabrication and theoretical explanations.

Here, the basis is spectacular physical properties of bismuth selenide which lead to its diverse capabilities in different green energy applications in medicine, engineering, and basic science and in the direction of sustainable development goals of United Nations for the human future. Many theoretical calculations, experimental characterizations, device fabrications and joint theoretical-experimental research have been devoted to bismuth selenide materials and the ground work is still ongoing. For example, one very interesting and fundamental topic is Majorana fermions which are the basis of quantum bits for future quantum computing advances. Moreover, in order to make use of the topologically protected surface states, one can reduce the bulk contribution in the electronic states via reducing the bulk carriers by doping or having smaller structures with high surface to volume ratio. **Table 1** presents a summary of selected physical properties of bismuth selenide. Inspired by this, in this article we aim to probe theoretical and experimental explorations and relate them in a joint theoretical-experimental approach. it is to draw a picture from recent status and mentioning prospects for future potential studies.

Table 1. Bismuth Selenide physical properties

Property	Value/Status	Reference(s)
Appearance	Gray- light dark	2
Melting/Boiling point	710/2360 ^{O}C	2
Density	6.82 gcm^{-1}	2
Solubility	Insoluble in water and week acids	
Toxicity	A level of toxicity for human and marine life	
Crystal structure room temperature	R$\bar{3}$m Rhombohedral space group 166	5
Thermal conductivity at room temperature	1 Wm^{-1}K^{-1}	6

View Article Online
DOI: 10.1039/D5MA00876J

Refractive Index	3.88	7
Hall coefficient	$0.14x10^{-6}$ Ω m/tesla	8
Electron effective mass	0.13 m_0	9
Dielectric constant	29.8	10
Plasma frequency ω_p	$1.36x10^{-14}s^{-1}$	10
Semiconducting state	n-type with inherently selenium vacancies	
Bulk-Band gap	300 meV	
Doping state	Cu , Sb, Ca, Cd, Pb, Zn, Fe,Cr, In, Mn, Ni …	10–15
Carrier Density-nanostructured	10^{17}-10^{19} cm^{-3}	
Absorption coefficient	$4.4x10^5$ cm^{-1}	7
Ionization Energy	4.45 eV	16
Electron-hole lifetime at 300K	50 ps	17
Surface states density	$4x10^{13}$ cm^{-2}	1
Superconducting state	Superconductor at 3.8 K, Cu doping	18
Hall resistivity	4 mΩ.cm	19
Mobility	500-700 cm^2/VS	20
Thermoelectric properties, typical values at room temperature		21
a. Figure of Merit	a. 0.01	
b. Seebeck coefficient	b. $1.15 X 10^{-4} VK^{-1}$	
c. Thermal conductivity	c. $0.75 Wm^{-1}K^{-1}$	

Therefore, for many of the reported green energy devices, the interaction of light and matter and its photo-physics plays the key role, wherein the concepts can be extended to a wide range of possible technological implications, as well as similar topological insulator materials. The bulk and surface broadband optical properties of bismuth chalcogenides have been widely investigated via different characterization methods (section 6), and the corresponding details and values are reported, for example, for refractive index, absorption spectra, etc, in the literature[22–25]. For bulk Bi_2Se_3, the main optical transitions happen between the selenium 4p states and the hybridized Se(4p)-Bi(6p) states at valence/conduction band edges. However, promising optical properties stemming from surface electronic structure, which are related to preservation of time reversal symmetry in 3D topological insulators, the spin-momentum lock, spin-orbit coupling effects, together with massless electrons in the Dirac cone. Such effects cause novel potential applications to be quantum mechanically possible, *i.e.,* the helicity preserving PL [26]with chiral spin-momentum textures and polarizability dependent photocurrent[27].

View Article Online
DOI: 10.1039/D5MA00876J

The detection of incoming light polarization for infra-red light at very low temperatures has thus been reported for Bi_2Se_3 -based photo-detectors (See Ref[27] **Fig.** 3) as a phenomenon which is not plausible in typical infra-red detectors. Bismuth selenide unconventional room temperature photoluminescence in the range 1.8-2.4 eV, has yet to be evidenced and attributed to confined surface excitons. Kung et al. have observed the polarization preservation for the electronic transition between the Bi_2Se_3 surface states to be related to chiral excitons[26]. They have found that polarization of chiral exciton PL is preserved up to room temperature and robust with respect to chemical substitutions. This can be attributed to the weakness of spin-flip scattering between surface states with opposite helicity. A theoretical model proposed to explain the PL transition from the surface states[26], which can quantitatively describe the observed polarizability preservation in experiments. The transition between the surface state 2 (SS2) and Rashba surface state (RSS) is the main responsible transition. The weak charge carrier interactions with phononic modes in this region allow the radiative decay of exciton states, resulting in the observed unconventional PL.

The corresponding PL yield can be further enhanced via decoration with gold nanoparticles, in which the localised surface plasmon resonance exist[28]. The Bi_2Se_3/Au system shows a modified PL peak/intensity and is related to a hybridization of gold-Se/Bi orbitals, accompanied by a charge transfer from Au to bismuth selenide with appreciable enhanced PL. New recombination channels are thus created, leading to retarded recombination pathways and enhanced PL with circular polarizability[28], which can be explained via a mechanism called exciton-plasmon coupling.

The chemical bonding effects in bismuth chalcogenides and selenium bismuth lattice[25,29–32] are, on the other hand, responsible for the mentioned physical properties and the related device implications; therefore, exploring the chemistry of the selenium-bismuth bonds within the bulk or at the surface is of fundamental importance for any green energy application. Here, the light absorption and the subsequent charge excitations happen mainly in between the valence band selenium 4p states and the hybridized Se(4p)-Bi(6p) states in the conduction band. The local distribution of the charge density within the chemical bond is different among the Selenium atoms, which are in bonding with one or two Bi atom(s), corresponding to a more symmetric and non-symmetric electronic clouds.

For the Bulk case, the energy difference between the band edges is somehow related directly to the degree of covalency between the chemical bonds *i.e.*, on the electronegativity difference of cation (Bi) and anion (Se). The greater the electronegativity difference, the higher the band gap value and vice versa. Therefore, the bismuth sulphide has a band gap of about 1.3 eV, and the bismuth telluride has it of 0.12 eV. Dielectric constant and refractive index in bismuth chalcogenides follow the order of electronegativities *i.e.* Bi_2Te_3>Bi_2Se_3>Bi_2S_3>Bi_2O_3.[25] Based on the same interpretation, the Mullekin charge stayed on the lattice anions, chemical bond lengths, unit cell volumes, the number density of absorbing centres in space and thus the absorption coefficient varies based on nature of chemical bonds in between the constituent atoms in the lattice[25]. The geometrical parameters, together with thermal expansion coefficients, thermal and electronic conductance, obey the same trend as a function of the degree of covalency in bismuth-chalcogenide chemical bond[33].

Here, a more covalent bond -the lower electronegativity difference- translated to a higher electrical conductivity and longer bond distances. Mechanical properties have their own relations to this[34], however, the directional unsymmetry within the unit cell stemming from weak van der Waals bonds along the z axis and stronger covalent and symmetric chemical bonds within the ab-plane makes it possible to have fine exfoliation of bismuth selenide[35] and telluride materials along the [001] direction. Therefore, in a top-down approach, one can exfoliate very thin layers of these topological insulators from single crystals.

View Article Online
DOI: 10.1039/D5MA00876J

A similar impact exists on the chemical growth of bismuth selenide nanostructures. This imbalance in the chemical bonds within the ab-plane and along the z-axis leads to a rather high formation energy difference between different crystal growth directions. Therefore, thermodynamic preference is to shape the crystals normally as hexagonal sheets having a meaningful faster growth rate within the hexagonal sheet plane. To modify this imbalance and break the asymmetry, additional factors need to be implemented. Moreover, directional charge transport similar to what is observed in bismuth halide perovskites[36] is expected. These chemical bonding approaches have been explored earlier and can be adopted from the field of halide perovskite solar cell materials[37].

For surface states, the theory published by Thouless, Kohmoto, Nightingale, and Nijs (TKNN 1982) [38,39] explains the existence of topologically protected surface states and their relation to electronic structure and spin-orbit coupling. Anna Isaeva et al.[40,41] have reported on the chemical bonding effects for topologically protected surface states and particularly in bismuth selenide and telluride, and doped with Antimony. They explored the correlation between the evolution of chemical bonding and structure with the variability of the topological properties. These concepts can further be used for the material design of topological insulators. Moreover, one can tune the ratio between the surface and bulk states via engineering the growth, and in very thin layers, the time reversal symmetry can be broken *i.e.,* in less than 6 QTLs [42]and via doping with transition metal magnetic dopants[43–45].

The above-mentioned impacts of intra-atomic chemical bondings on physical properties are creating a framework for device applications. Mid-Infrared bandgap and high conductivity make it feasible to use bismuth selenide for infra-red photodetector applications and other practical cases such as photocatalysis, solar cells, etc (section 5). Price, ease of growth method, compatibility within the device framework, weight, abundance of ingredients, stability and overall performance are among additional factors to be considered for any special device implementation. The surface adsorption of water and oxygen has so far been a main degradation mechanism in semiconductor devices, triggering the decay of device performance during the time. The layered van der Waals structure of this class of materials however, shows a robust stability against the adsorption of moisture and oxygen for the device stability and is counted as a general beneficial factor for device applications. For medical applications, more knowledge needs to be established to understand the fundamentals behind; however, the black color and infrared bandgap of bismuth selenide are very important for the use of safe infrared light and local heating of surrounding bio cells for photothermal therapy applications. The van der Waals spacing in between the QTLs of bismuth selenide and telluride offers the potential for external ions to be taken up within the lattice, an essential process for practical electrochemical implications such as ion batteries[46].

Therefore, one can establish a library from different bismuth chalcogenide compounds and other elements based on local atomic chemical bonding effects and further help the accomplishment of the research field for future green energy applications. For example, mixed compounds with $Bi_2Se_xTe_{3-x}$ formulae can tune desired property in between the telluride and selenide counterparts. One important point is that during the crystal growth and based on the lattice formation energies, bismuth telluride crystals formed intrinsically as p-type however, the bismuth selenide tends to have more selenium vacancies and being as n-type. Via changing the ratio between the Se and Te in B $i_2Se_xTe_{3-x}$, the mobility modifies based on the above-mentioned effects, however the number density of charge carriers is also affected, and the material can change from n-type (x=3) to p-type (x=0) so. Therefore, in thermoelectric applications via fractional substitution of Te atoms with Se , the Seebeck coefficient crosses zero and changes sign for Bi_2Te_2Se[33]. As reported by Goodman in 1958[29], first the Te-I atoms are substituted with Se atoms and thereafter Te-II atoms will be substituted. The partial

View Article Online
DOI: 10.1039/D5MA00876J

substitution of Te-I or Te-II lattice atoms with selenium, have opposite impacts on the bandgap and conductivities[33,47].

3. Quantum phenomena in topological insulator Bi_2Se_3

In physics, breaking the space symmetry through the ordered arrangement of crystal ions and the corresponding electronic states are fundamentally attracting causing new quantum mechanical phenomena. Here, one can study and expand the borders of material science. Quantum anomalous Hall effect and spin Hall effect, high temperature superconductivity, Majorana fermions observed in specific novel nanomaterials are among the quantum mechanical marvel occurrences and of crucial importance for potential applications *i.e.* fault tolerant quantum computing and quantum bits, spintronic and magnetoelectric devices. In this sense, topological insulators and 3D topological insulator bismuth selenide present a rather recently discovered and important material class. They have insulating bulk states and topological order protected metallic surface states for shedding light into these fundamental research [27,48,49]; One major discovery in 1980s, the breaking of Hamiltonian symmetry for a two-dimensional confined electrons under a strong magnetic field was the quantum Hall effect. This order leads to *i.e.* dissipation-less transport of electrons and emergent particles with fractional charge [48]. Later on in 1982, Thouless et al. calculated quantum Hall conductance for these states [38] and topological aspects of electron wavefunction in two dimensions under magnetic field were explored by Kohmoto [50]. After that, important research efforts were going on; that a description for historical perspective of topological insulators can be found in Ref. [39].This topological order also occurs in three dimensional solids wherein the magnetic field replaced by material own spin-orbit interactions. They are called topological insulators since they possess insulating bulk and exotic metallic surface states [48]. For bismuth selenide however, a main theoretical prediction were reported via Fu and Kane in 2007 [51] and experimental verification happened in 2008 via Hsieh et al. [12]. Herein, we describe bismuth selenide as a prominent prototype topological insulator with few potential and already-implemented example experiments illustrating *i.e.* the quantum mechanical anomalous and spin Hall effects, Aharonov-Bohm effect, spin-momentum locking and Majorana fermions. A more comprehensive perspective about the quantum phenomena in topological insulators can be found somewhere else [52].

As mentioned, the key physical property of bismuth selenide (nominating the material as a topological insulator with own potential applications) is the topologically protected surface states forming a Dirac cone near the band edges [3]. In electronic band structure, the presence of Dirac cone shows the spin orbit decoupled bands wherein the electron spin and momentum are locked and different spins can have different movement direction at the surface of Bi_2Se_3 single crystal *i.e.* in the applications such as polarization dependent visible or infra-red light detection [3]. These types of behaviours stem from the details of chemical bonding of surface states and can be characterized with different measurements techniques. Here we shortly describe an illustrating picture for anomalous quantum Hall effect, quantum spin Hall effect, Majorana fermions, spin-momentum locking in bismuth selenide via mentioning few example applications.

3.1 Quantum Anomalous and Quantum Spin Hall Effects.

The classical Hall effect discovered by E. Hall – year 1879 [53]. It represents simultaneous introduction of perpendicular magnetic and DC electric fields (*i.e.* a few Tesla and few Volts) on a semiconducting thin film and measuring the subsequent lateral electrical potential difference on the edges of the film via a multi-meter. Here the Lorentz force from magnetic field results in a lateral accumulation of opposite charges (electrons and/or holes) at edges wherein the sign and value of the lateral potential can determine the type and charge carrier density within the film, magnetoresistance and Hall

View Article Online
DOI: 10.1039/D5MA00876J

coefficient. (a mathematical description in ref [53]). In the absence of external magnetic field, this effect has been observed in the presence of magnetization M inside the solid that can act as source of magnetic field, in this case it is called anomalous Hall effect. The quantum mechanical description of Hall effect so-called Quantum Hall effect is such that the Hall conductance in low temperatures and strong magnetic fields shows quantized values in units of $e^2/\hbar$ and is based on the number of occupied Landau levels in the solutions of system Hamiltonian. In this case, the presence of applied static magnetic field can result in quantization of the Landau levels and oscillatory movement of electrons within the film (mathematical description in Ref. [54]). To be able to observe the quantum Hall effect, the energy difference in between the Landau levels or the applied magnetic field must be large , the thermal energy of electrons be comparatively small and the samples must be of high electron mobility so that the width of Landau level is narrow enough for oscillations to be observable [52].

The quantum version of spin Hall effect and anomalous Hall effect called quantum anomalous Hall and quantum spin Hall (QSH) effects wherein strong spin-orbit coupling interactions inside the material replace externally applied magnetic field. In anomalous Hall effect, the chiral edge states exist and the quantum conductance is quantized and in quantum spin Hall effect the edge states propagate in different directions, the net charge current is zero, but the spin current can be detected via applied external electric field and spin quantum conductance is quantized as well. The integer numbers appear in the quantum conductance is related to topological class of the material, symmetries and features in the electronic band structure called Chern or TKNN number [38] which also corresponds to the number of occupied Landau levels. In the case of time reversal symmetric systems that exhibit the spin Hall effect, however, the Chern number is identically zero and another class of topological quantum numbers known as Z_2 invariants are the relevant topological parameters. For this reason, a class of materials called topological insulator and the quantum spin Hall state can be observed in them. The necessities for QSH state of matter which happens in topological insulators are time reversal symmetry, band inversion [55], and strong spin-orbit coupling (SOC). QSH state can be described by effective topological field theory and insulators classify in two categories based on Z_2 classification. Mathematical description exist in Refs. [56] and [52]. **Fig. 1** presents a description of different Hall effects.

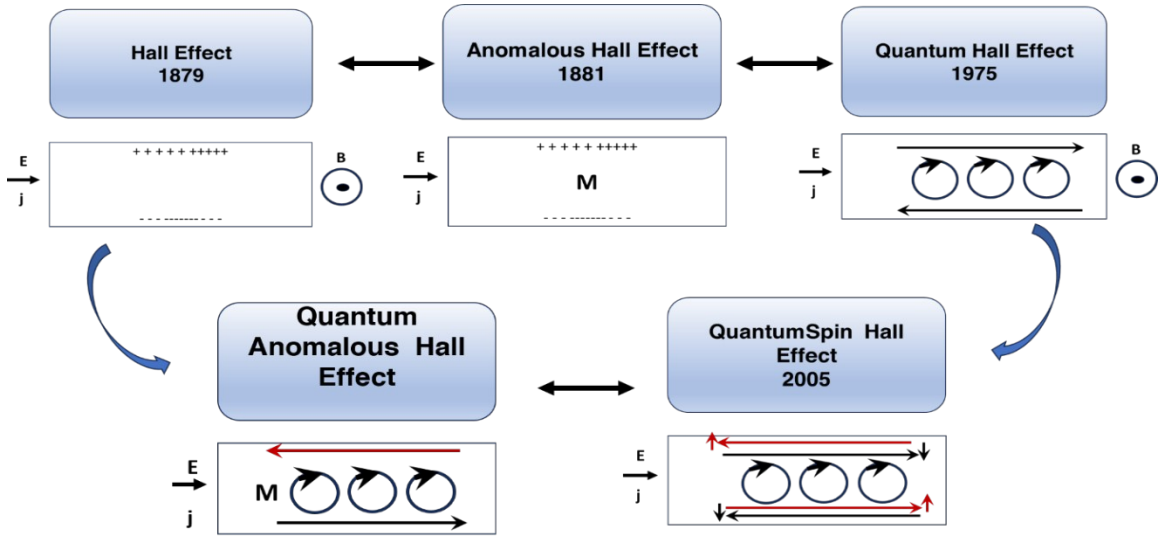

Fig. 1. Schematic representing the Hall, quantum Hall, anomalous Hall, quantum spin Hall and quantum anomalous Hall effects.

View Article Online
DOI: 10.1039/D5MA00876J

So far, the Hall Effect [57,58], anomalous Hall effect [59,60], quantum Hall effect [61,62], quantum anomalous Hall [63], and photoinduced inverse quantum spin Hall [64] effects have been separately observed in intrinsic or doped Bismuth selenide materials. Hall effect in bismuth selenide studied as transport experiments, and simultaneously the weak anti-localization effect, Shubnikov-van de Haas oscillations phenomena were observed and studied by Tang and Kuntsevich [51], [65]. Zhu and Moon et al. in separate studies observed the anomalous Hall effect in bismuth selenide in contact with a ferromagnetic layer or in a Cr-doped case [53],[54]. For quantum Hall measurements, Kumar et al. observed the QHE in bulk of Bi_2Se_3 single crystal wherein the point defects contributed to mechanism of QHE [61]. In a separate study Moon et al., through a defect engineering of the Bi_2Se_3 surface, observed a tunable QHE [62].

3.2 Aharonov-Bohm effect

Aharonov-Bohm effect [54] presents a phase interference of electron beams passing outside a cage encapsulating magnetic fields, wherein the corresponding induced phases from a non-observable applied field can be experimentally detected. This was observed in bismuth selenide quantum ribbons grown via molecular beam epitaxy in 2009, [66]. A mathematical description presented in Ref. [54]. **Fig. 2** shows the observation of the Aharonov-Bohm effect in bismuth selenide nano-ribbons in four-terminal resistance measurements. A clear modulation of the resistance is observed, corresponding to one flux quantum (h/e) threaded into the cross-section of the nanoribbon [54]. The green arrows represent the electronic current path from which the surface states can interfere due to the magnetic field phase induction.

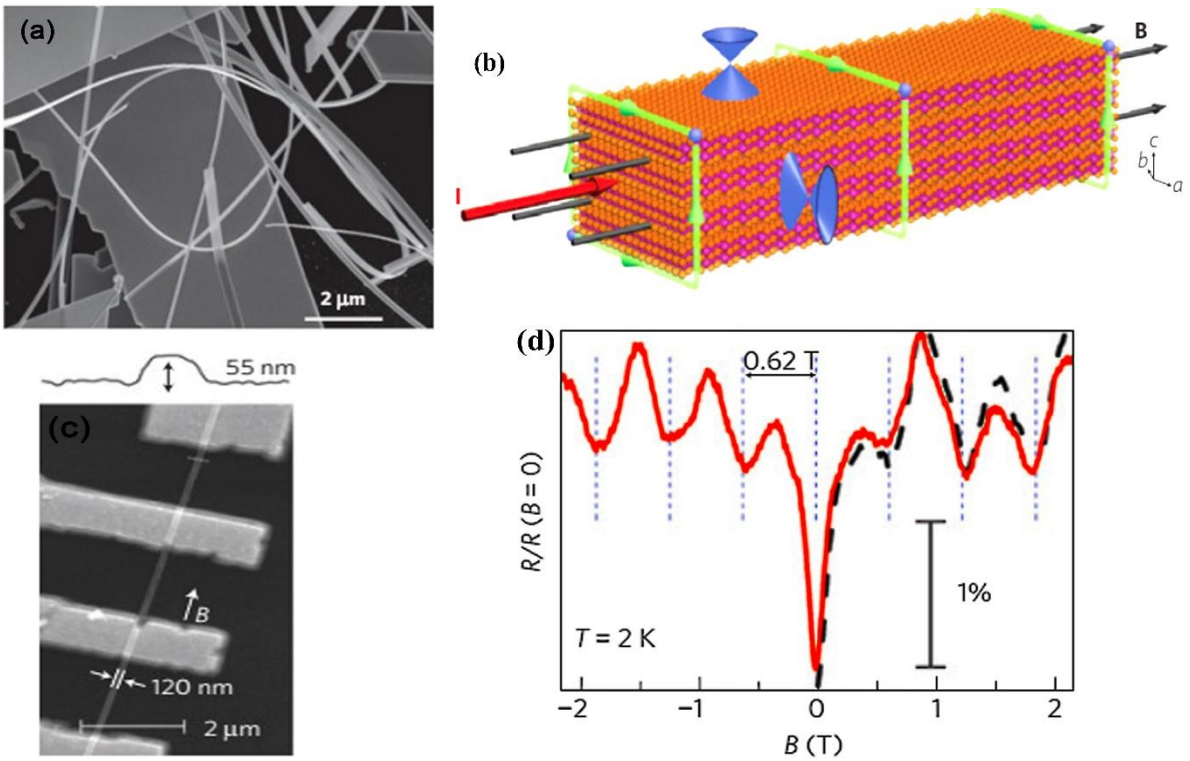

Fig. 2 Aharanov-Bohm effect in bismuth selenide nano-ribbons. (a) SEM image of nano-ribbons. (b) Schematic of the electrical current and magnetic field in nano-ribbons. Surface state Dirac cones illustrated as well. The green loops encircling the same magnetic flux stand for phase-coherent paths through which

View Article Online
DOI: 10.1039/D5MA00876G

the surface electrons interfere. (c) SEM image of four terminal magnetoresistance measurement. (d) Normalized magnetoresistance of the nanoribbon versus magnetic fields at 2 Kelvin. The solid red and dashed black traces were taken with scan rates of 3 mT s^{-1} and 10 mT s^{-1}. reproduced with permission from ref [54].

3.3 Spin-momentum lock

In heavy elements, the outer electrons with higher total angular momentum quantum numbers must be theoretically treated via relativistic terms. The interaction of angular momentum aroused magnetic field with electron spin in spin orbit coupling effect splits the degenerate states in the conduction band. In the bismuth selenide Dirac cone, the spin of different branches is opposite resulting in a momentum spin lock wherein different spins can propagate in different directions on the surface leading to many potential spintronic applications. For example, in polarization detection, the Dirac cone states at the surfaces are sensitive to electron spin and k quantum number and have directional dependence along [001] direction in the single crystal; therefore, one can have special sensitivity of Infra-red photodetector to the polarization of incoming photons. This is special just with topological insulators and have been experimentally observed in bismuth selenide [27,67]. **Fig. 3** shows the spin polarization detection of infrared light in bismuth selenide at temperature about 15 K. Based on the excitation selection rules and depending on the direction/polarization of incoming photons, different currents can be measured. In some cases, the momentum of excited electrons is perpendicular to the contacts and the measured current is much lower in comparison.

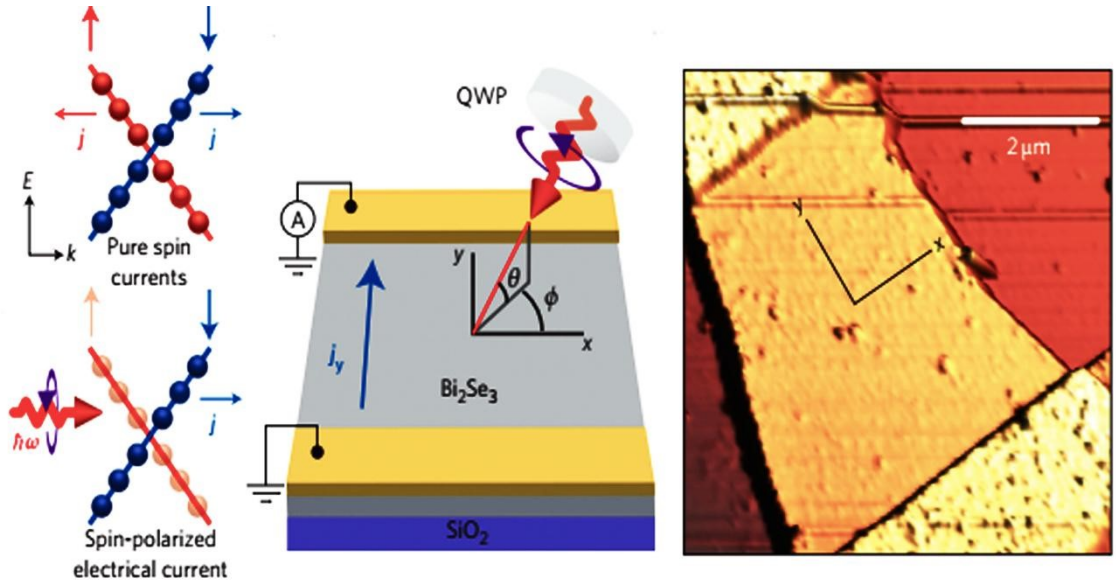

View Article Online
DOI: 10.1039/D5MA00876J

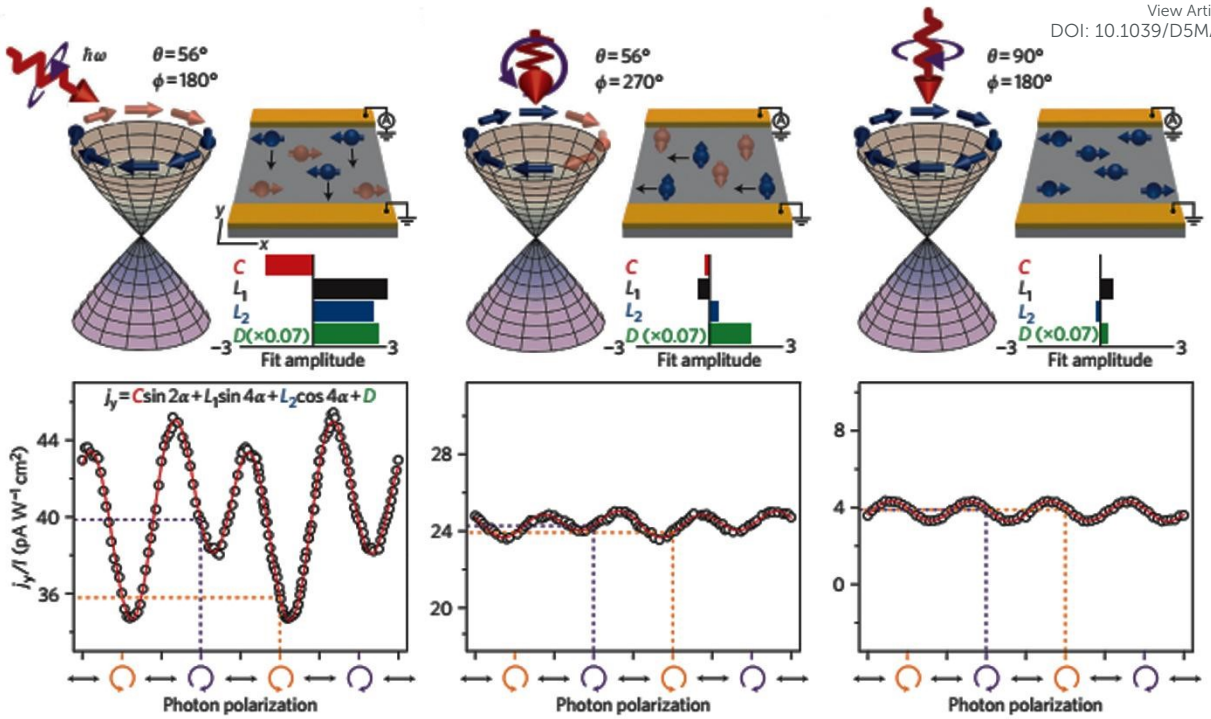

Fig. 3. Schematic of the Infrared detector based on bismuth selenide and the spin polarization detection of infrared light in bismuth selenide at 15 K for different incoming light directions/polarizations leading to different spin textures and observed currents. The occupation of Dirac cone branches is shown. Reprinted with permission from ref. [27].

3.4 Majorana Fermions

It is theoretically predicted by Ettore Majorana in 1937. Here, at the interface of an s-wave superconductor and a topological insulator, the Majorana fermions can be formed wherein the superconducting vortices are possibly their own antiparticles, electrically natural and obey the non-abelian statistics called Majorana fermions [68,69]. There, based on the proximity effect, the metallic surface states of topological insulator behave as superconducting. Majorana fermions are the fundamental representation of a quantum bit in future fault tolerant quantum computing research in historical dream of having a quantum computer [70]. This has been predicted numerically [71], experimentally evidenced in topological insulator Tellurium bismuth[72] and also in selenium bismuth [68].

4.Theoretical Calculations and Prospects

Theoretical calculations have been a paving-route approach towards understanding, predicting and engineering nanomaterials for future development goal based on green energy applications. Here one constructs the complementary point of view wherein experimental efforts can be conducted, designed, and wisely optimized to build novel nano-bio-material-based devices. Regarding the intensive studies on bismuth selenide, different theoretical approaches with different levels of accuracy and implemented approximations describe the related quantum mechanical underlying physics for bismuth selenide nanomaterials and devices; herein the description of *i.e.* chemical bonds and distribution of electronic cloud, density and band

View Article Online
DOI: 10.1039/D5MA00876J

structure of electronic states, Dirac cone, spin texture, the phonon states, electronic structure, etc is based on the achievement of numerical convergence for system Hamiltonian. It is very important to know the validity and accuracy of different levels of theory for description of bismuth selenide theoretical results. This concludes in postprocessing information for representation of different device phenomena (*i.e.* charge recombination and transport, polarizable dependence light absorption, ...), characterization data (*i.e.* analysis of ARPES, XRD, Hall measurement, XPS, ...) and physical properties such as conductivity, mobility, defect density, spin-momentum coupling, ... So far, density functional theory (DFT) has been a main considered methodology for many cases since many years for the researchers in the field [73], however many-body techniques, GW method, cluster expansion method coupled to data mining, artificial intelligence, machine learning and neuron network algorithms and even paper and pen analytical calculations have thus been hugely affecting the picture shedding light into understanding the main DFT results. Other approaches and methodologies have so far been considered to study the electronic structure of bismuth selenide including for example Ab initio molecular dynamics [74], DFT+Monte Carlo [75], dynamical mean field theory (DMFT) [76] and first-principle Green function approach[77]. For DFT calculations in order to correctly introduce the interlayer van der Waals forces into account, Grimme included a semiempirical term of dispersion correction r^{-6} type into the general gradient approximation(GGA) exchange-correlation functional called Grimme-D2 or Grimme-D3 correction [78]. The r^{-6} force is attractive term and the repulsive contribution comes from the exchange-correlation part itself. Many-body dispersion for long range interaction corrections can be used instead as well [79].

Bismuth selenide has a rhombohedral $R\bar{3}m$ layered structure [2] where different in-plane layers stacked on top of each other to make a multi quintuple-layer (QTP) structure with van der Waals forces in between the layers. In QTPs. there are two different types of selenium atoms, one bounded to two bismuth atoms and one in the van der Waals (vdW) layer bounded to one Bismuth atom. It can experience different phase transitions under higher pressures and temperatures [80]. The orthorhombic phase (space group P_{nma}) is considered as another thermodynamically stable phase [81] with lattice constants of a=11.91, b=4.04 and c=11.18 Å and a band gap of about 1 eV lying in visible region which is not a topological insulator. **Fig. 4** shows the lattice structure and atomic configuration in bismuth selenide crystal. Here, the covalent chemical bond formed in between the selenium and bismuth atoms and the main

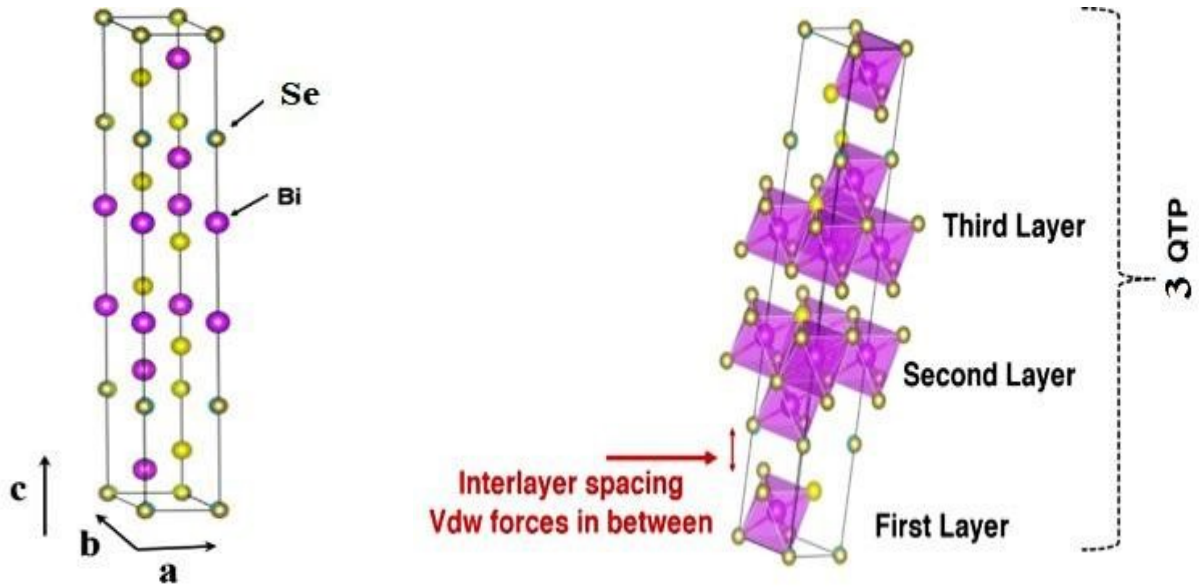

View Article Online
DOI: 10.1039/D5MA00876J

Fig. 4. Rhombohedral unit cell of bismuth selenide and the corresponding lattice vectors. An octahedral polyhedron is formed between the bismuth (purple spheres) and selenide (yellow spheres) atoms in a layered structure. The layered structure of a three-quintuple layer Bi_2Se_3 shown wherein van der Waals forces keep the interlayer spacing in between them.

states contributing to top valence band (VB) and bottom conduction bands (CB) are hybridized states. They are mainly contributed from selenium 4p and bismuth 6p orbitals respectively [82] which are the main role-playing contributors in charge conduction, light absorption and other physical phenomena. This detailed information about chemical bonding inside the lattice are of crucial importance for experimental characterization and the performance of devices based on Bi_2Se_3 materials. These theoretical data can explain the fundamental reasons behind the successful operation of corresponding devices. **Fig. 5** shows the typical calculated density of states (DOS) localised density of states (LDOS) and band structure of selenide bismuth and a comparison to experimentally achieved spectrum via ARPES technique. Based on the topological field theory, the topologically protected surface states of bismuth selenide make a Dirac cone at the bulk bandgap (**Fig. 5**c-d). It is the most special feature in electronic structure of bismuth selenide films and have many potential applications in fundamental and engineering research.

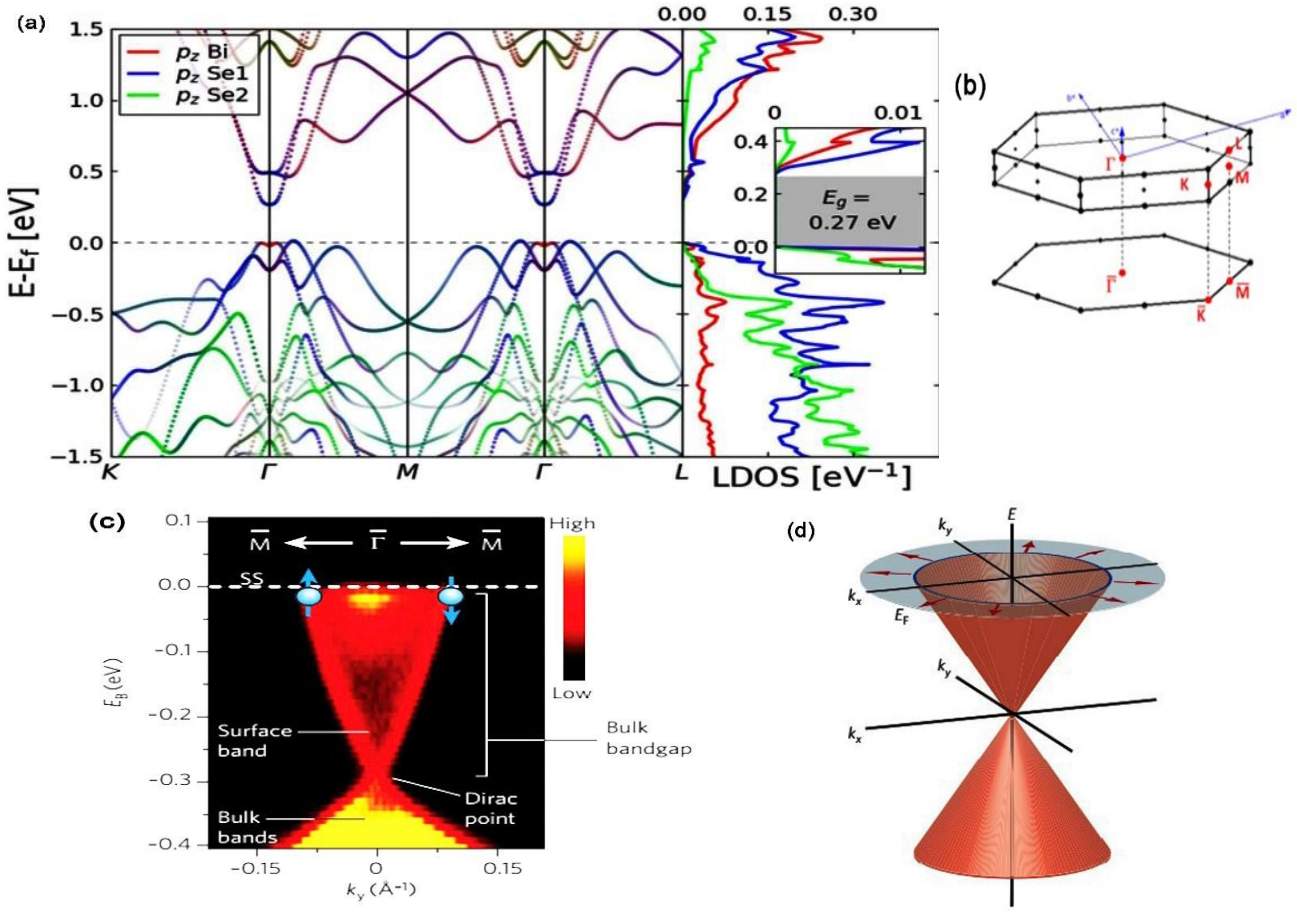

Fig. 5. (a) Electronic structure of bulk bismuth selenide calculated with spin orbit coupling based on GGA in ref [83] showing the contribution of bismuth and selenide p orbitals at band edges; (b) Schematic presentation of the bulk first Brillion zone Reprinted with permission from Ref. [83]. (c) experimental

View Article Online
DOI: 10.1039/D5MA00876J

ARPES spectrum of bismuth selenide few-layer film showing the band structure and Dirac point at intra bandgap space. Spin up and down of Dirac electrons illustrated by blue up and down arrow [48].(d) spin texture in Fermi loop arising from the spin-momentum lock. Reprinted from Nature by permission from ref [48].

Lawall and Shaari, Reid and Zhang et al. have in separate studies reported the basic electronic structure of bismuth selenide based on GGA-DFT [82,84,85] , moreover the experimental band structure using ARPES and spin resolved angle resolved photoelectron spectroscopy (SARPES) have been reported in many studies including ref [86]. The van der Waals gap in between the layers have an important impact on the structural properties and band gap which has been studied with different levels of theory in Refs. [87,88]. In a relevant study, bismuth selenide bulk structures under stress studied in Ref. [89] as well . Amorphous bulk electronic structure have been studied via ab-initio molecular dynamics [74]. Temperature dependency of bandgap variation together with calculations of electron-phonon interaction have been pursued in ref [90]. Via DFT calculations, mechanical, electronic and optical properties of bismuth selenide reported using LDA exchange correlation functional [34] and Lawal et al. reported basic structural and optical properties via GGA-DFT and Quantum Espresso package in Ref [91]. Ayadi et al. have investigated the electronic structure of Bi_2Se_3 heterostructures via ab-initio GW calculations [92]. Similar studies on the similar compounds such as Bi_2Te_3, Sb_2Se_3 and Sb_2Te_3 and comparisons of the chemical bonding effects have been reported in refs [93–95]. **Table 2** summarize some structural and electronic properties of bismuth selenide calculated via ab-initio methods and compared to experiment. The chemical bonding effects and interactions/binding between different QTLs in bismuth selenide have also been studied via electronic localized function (ELF) and non-covalent interaction index (NCI) methods and the interlayer charge transfers and intra-layer distances accordingly explained[30].

Table 2. Comparison of certain theoretical and experimental results for Bi_2Se_3 structural and physical properties.

	Experiment	**Theory**
Crystal structure	R$\bar{3}$m	R$\bar{3}$m
Lattice constant a,c (Å)	4.144 , 28.63[96]	4.22 , 29.21 [GGA87]
Interlayer spacing (Å)	2.57[96]	2.74 [GGA87]
Chemical bond length Bi-Se (Å)	2.78 and 3.04[17]	2.97 and 3.04[#]
<Se-Bi-Se (Degree)	86[O]	84.9[O #]
Band gap (eV)	0.3[3,96]	0.3[3]
Charge mobility(cm^2/VS)	1000[97]	-
Dielectric constant (∞)	29[98]	23.1[91]
Absorption coefficient	4.4x10^5 cm^{-1} [*7]	2.3x10^5 cm^{-1}[$25]

* at 500 nm # R.W. Wyckoff, Crystal Structures, John Wiley & Sons, 1965 at 300 nm

The details of lattice, bandgap and transport properties of bismuth selenide and comparison of DFT values and experiment however show the validity of DFT approach for this material (**Table 2**). Moreover, based on the different levels of implemented theory, different DFT based methodologies can have different accuracies and validities, resulting in a bit different estimated values corresponding to physical properties, **Table 3** compares LDA, GGA, and hybrid functional calculations. GW calculations shows the bulk band gap as direct at Gamma point however LDA and GGA show slightly indirect [99], Crowley et al. reproduced the GW_0 calculations with a hybrid functional B3Pw91 [100]. A more detailed discussion about the bandgap value and accuracy comes in Ref. [101].

View Article Online
DOI: 10.1039/D5MA00876J

Table 3. A comparison of Bi_2Se_3 structural properties and calculated band gap based on different DFT theoretical levels.

	LDA [ref]	LDA+U [ref]	GGA [ref]	Hybrid functionals [ref]
Lattice constants (Å)	4.08,28.24[87]	4.11,28.44 **U=3**,[87]	4.22, 29.21[87]	4.10,28,49[25]
Interlayer spacing (Å)	2.37[87]	2.42[87]	2.74[87]	-
Chemical bond length Bi-Se (Å)	2.9[%]	2.89[#]	2.87[%]	2.83[25]
<Se-Bi-Se (Degree)	85.4-91.2[%]	85-91[#]	86-92[%]	85.48-92.71[25]
Band gap (eV)	0.45[87]	0.29[87]	0.15[87*]	0.27[25]

* Without inclusion of van der Walls forces. [%] additionally Calculated by Khaki et al. using GGA+Van der Waals and LDA+vdw in Quantum Espresso package. # interpolated /estimated from the calculated data and geomaterical parameters (error 1-3%). Compared to LDA, the LDA+U results in very similar geometrical values (2% error).

In order to reach a tuneable physical property for device application, different modifications are possible to be done. During the crystal growth selenium vacancies are thermodynamically formed and the bismuth selenide is intrinsically a n-type semiconductor with a typical defect density of ~ $5x10^{18}$ cm^{-3} [102]. **Table 4** presents few examples from bismuth selenide different doping states and how one can tune the charge carrier density inside the bulk. The defect density and intrinsically n-type behaviour and the charge conductivities can be measured via Hall measurements; they are very important characteristic parameters affecting the cost and efficiency of final device. This can be controlled through *i.e.* doping and growth modification agents such as additives, adsorbents [103] and even partial substitutions of Se, Te and S within the lattice. Fermi level tuning can be adjusted via silver doping reported by Uesugi et al. [104] and Uchiyama [104] or *i.e.* Ca doping reported by Wang[102]. This engineering of properties can be done through doping and additives via different magnetic and non-magnetic dopants. Formation energies, electronic structure and structural properties of transition metal doped bismuth selenide has been reported by Abdalla et al. via generalized gradient approximation (GGA) functional based on density functional theory calculations with inclusion of spin-orbit coupling (SOC) effect [5]. Here, the magnetic moment of the dopant can open up a gap at the Dirac point and time reversal symmetry will be suppresses. Doping of series of transition metal cations and the impacts on the electronic structure is reported as well [43]. It has been experimentally measured via ARPES technique somewhere else [45,105].

Table 4. Different doping states of bismuth selenide and example references.

Dopant / Variant	n-type / p-type	Comments	Ref
FE	n-type	$n=2.4x10^{20}$ cm^{-3} σ =4100$\Omega^{-1}cm^{-1}$	106
CU	Donor n-type	$n=2x10^{20}$ cm^{-3} superconducting at 3.8K	18
IN	n-type	$n=2.2x10^{20}$ cm^{-3}	10
CA	p-type	Fermi level tuning and n-type to p-type conversion Via different doping concentration	12

View Article Online
DOI: 10.1039/D5MA00876J

NI	n-type	n=8.4x10^{18} cm^{-3} μ_{Hall}=32(cm^2/VS) Enhancement of thermoelectric power and field emission	107,108
CD/HG	acceptor	Dopant density 1.2-1.3x10^{19} cm^{-3}	13
NON-DOPED	n-type	n= 10^{17} to 10^{19} cm^{-3} and μ_{Hall} depend on crystal quality	109
MN	tunable	n-type for doping less than 5% p-type for x>5%	110
BI_2SE_2TE	tunable	ρ at 300K=16 mΩcm	111
AG[REFAG]	Donor n-type	Resistivity 150Ω μ_{Hall}=800 (cm^{2}V^{-1}s^{-1}) n=6x10^{13}(cm^{-2})	112

In principle one can make a library from different doping states with various capabilities and potentials for green energy devices. Here, the octahedra formed from the chemical bonding of bismuth and selenide inside the lattice is similar to the bonds in between the iodide and lead/bismuth in perovskite solar cell materials, where many well-developed concepts can be borrowed for topological insulator bismuth selenide and telluride. Here, as mentioned in section 2, the chemical bonds between individual atoms within the lattice tune the symphony of optoelectronic properties at the device level for different bismuth chalcogenides. The density of states, the number density of atoms in unit space, and the effective mass of carriers are slightly different and have their own impacts on the photo-physical processes. Nevertheless, following the same direction, exploring other bismuth chalcogenides such as Bi_2S_3(bandgap 1.3-1.7 eV) and Bi_2O_3(bandgap 2.2-2.8 eV), as well as 3D topological insulator counterpart rhombohedral Sb_2Te_3 have been informative and insightful, and people have performed comparative theoretical studies among these compounds. Bismuth Oxide and sulphide have different crystal structures and lattice symmetries and have not shown the topological insulator behaviour; however, are chemically robust in electrochemical processes, resistant to photo-corrosion and with a proper bandgap have their own benefits and drawbacks for device applications such as photocatalysis, photothermal therapy, solar cells and more. In bismuth telluride, however, the density of states and electronic structure features near the band edges is slightly different than Bi_2Se_3 and overall surface state band symmetries, and the anion Mulliken charges are different. [25] The chemical bonding between Bi-Se can be described in terms of ppσ interaction between the atomic p orbitals within the QTL. For Bi_2Se_3, both the VB maximum and CB minimum have a nearly isotropic effective mass. For Bi_2Te_3, six valleys for VB maximum are located in the mirror planes of the Brillouin zone and have a highly anisotropic effective mass.

A connected network of octahedral $BiSe_6$ constructs the bismuth selenide crystal structure; however, along the c axes, the network is not continuous, and there are van der Waals gaps in between the atomic layers (QTPs) and vdW forces keeping them together in the lattice. Here, one strategy is that to interpret and study the periodic electronic structure based on the properties of chemical bonds in between the bismuth and selenium, *i.e.* via tight-binding approach. The covalent bond between the metal donor and chalcogenide acceptor is responsible for many physical properties, such as light absorption, charge separation, transport, and the unit cell volume. In chemical bond engineering, based on simple steric size, cation/anion size effects and geometrical tolerance factors, atomic electronegativity considerations and Goldschmidt rules [113,114], the overlap of atomic orbitals based on tight binding model, one can predict , understand and control the nature and length of chemical bond and new materials can be formed.

View Article Online
DOI: 10.1039/D5MA00876J

Simple tight binding description of energy level of electrons ε(*k*) here presented via equation 1 wherein E_m stands for atomic energy level of orbital m, ψ and ψ_m are periodic and atomic wave function, r is location operator and Δu is the perturbation potential coming from the periodic total potential. This formula can describe many physical aspects of chemical bonding inside the material based on tight binding interpretations.

$$\varepsilon(k) - E_m = \frac{\int \psi *_m (\mathrm{r}) \Delta u \psi(r) dr}{\int \psi *_m (r) \psi(r) dr} \quad (1)$$

Tight binding approach have been implemented for the successful evaluation of bismuth selenide bulk and surface band structure by Acosta et al (**Fig. 6**). The topological nature of surface states, Dirac cone, bulk band gap, band inversions have been obtained via a simple tight binding method. It has been shown that energy of bulk states near the Dirac-point is associated with a band mixing of P_z and $P_{x,y}$ orbitals and mixing of angular momentum of J=3/2 and J=1/2. The results in this simple model can reproduce very well the data from computationally costly methodology in literature [115]

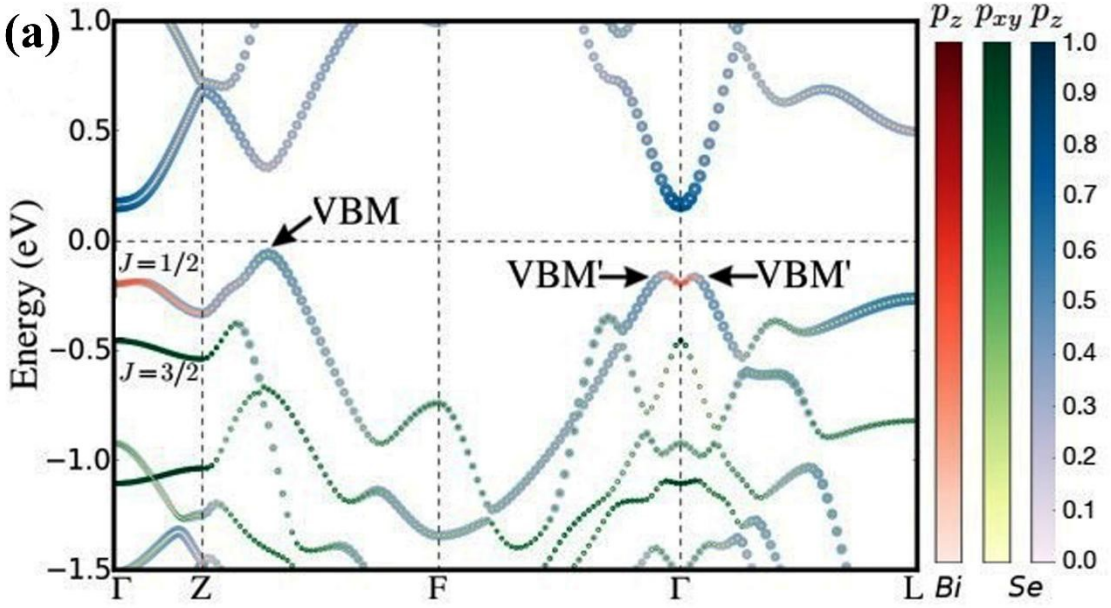

View Article Online
DOI: 10.1039/D5MA00876J

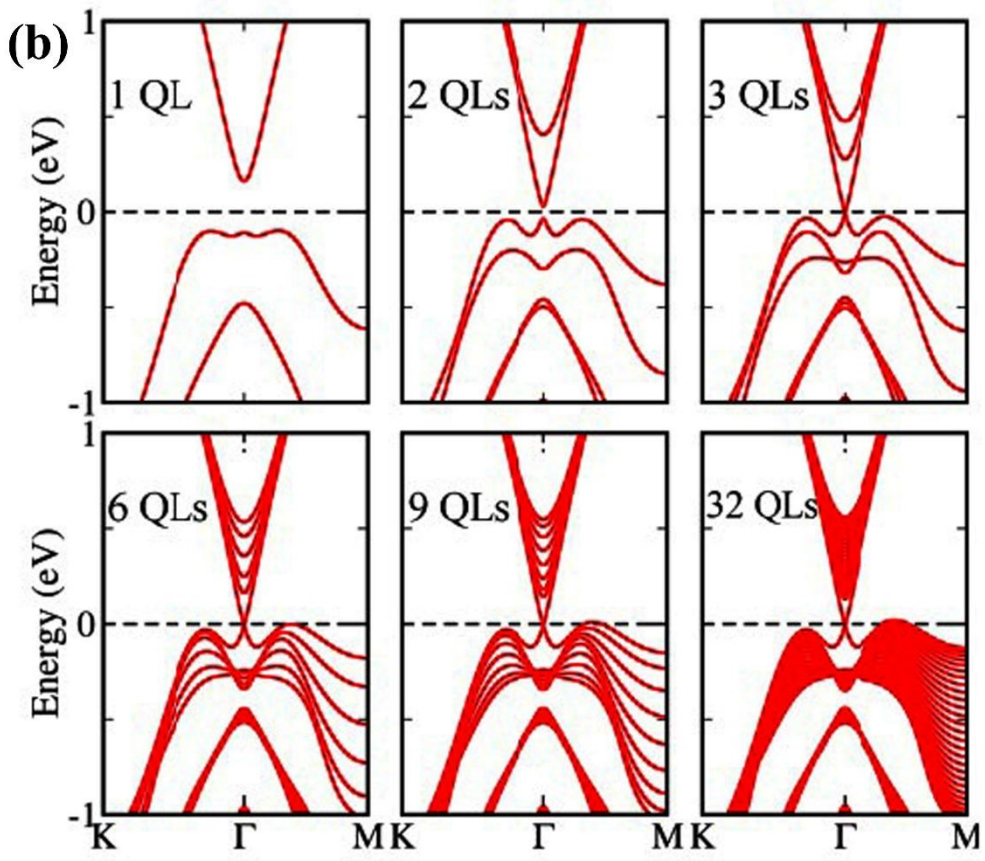

Fig. 6 (a) Bismuth selenide bulk band structure. The colour code represents the projections of the p_z Bi orbitals (red), p_xp_y Se orbitals (blue), and p_z Se orbitals (green) in the wave function. The maximum and local maxima of the valence band are denoted by VBM and VBM', respectively. (b) Band structure of Bi_2Se_3 surface for different thickness values. Reprinted with permission from ref [115].

The most special with theoretical calculations of bismuth selenide is the topologically protected metallic surface states forming a Dirac cone in the intra band gap space in band structure. This is resulting in time-reversal symmetry preservation nominating bismuth selenide as a topological insulator with its specific potential applications (**Fig. 7**). One can make application of these surface states via engineering the surface to volume ratio of corresponding nano-structures in experiment. In order to correctly calculate the surface states band structure in DFT programs one approach is to use hybrid functional together with spin orbit coupling and smearing [5,116]. Based on bulk theoretical calculations, the interlayer space in between the surface layers and the impacts of van der Waals forces on the corresponding band structure also reported in Ref. [88]. It was found that the surface states are robust and protected under stress; and the pressure tends to increase the Fermi velocity of surface electrons and surface density of states at bottom of conduction band [89]. Bouaziz et al have calculated the transition metal doping of bismuth selenide and telluride [111] surfaces in Ref. [117].The results were analysed with Anderson impurity model wherein the magnetic impurities open up a gap inside the Dirac cone. **Fig. 7** shows the surface band structure of bismuth selenide calculated in Quantum Espresso package. However, for very thin slabs, different thickness layers (Quintuple layers) have different band structure at the Dirac cone wherein a gap can open up for thin slabs; that have been explored theoretically and experimentally (**Figs. 7-8**) [42,100,103]. The theoretical description is reported in Ref. [100]. Wang et al have studied the magnetic quantum oscillations for surface states of 6 QTPL Bi_2Se_3 [111] surface via ab-initio calculations reported in Ref. [118]. The Bi_2Se_3 electronic structure under stress

View Article Online
DOI: 10.1039/D5MA00876J

have been investigated in Ref. [89] and it was found that the topologically protected surface states remains robust under the stress as well.

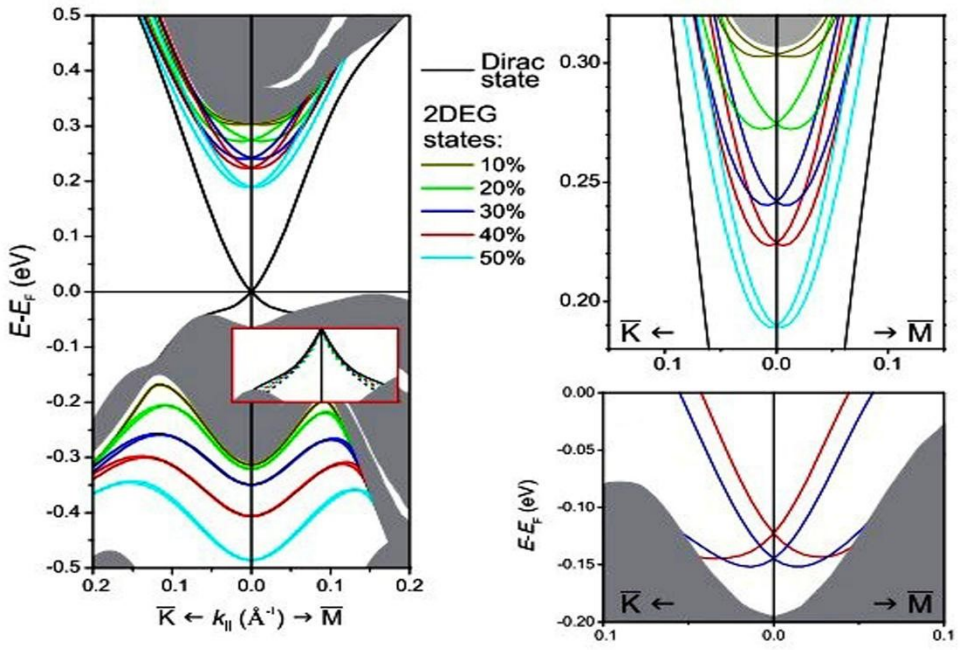

Fig. 7 Calculated surface band structure of bismuth selenide (9 QTPL) with different van der Waals gap expansions and the corresponding Rashba splitting and modifications on the Dirac cone states from ref [88] . Reprinted with permission from ref [88].

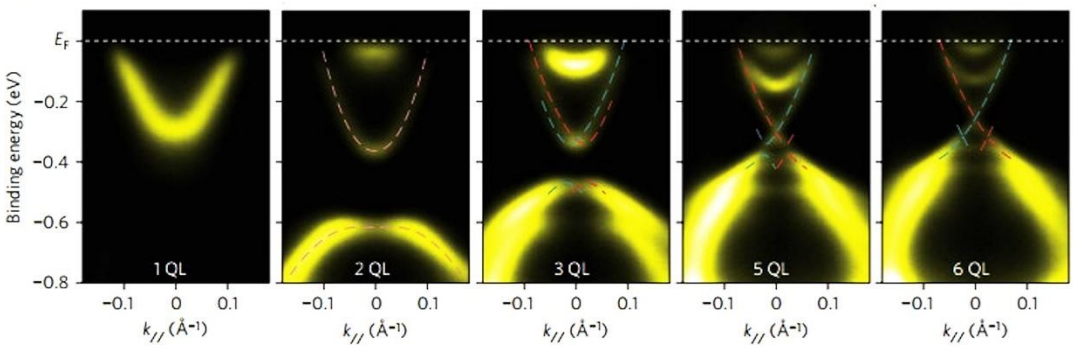

Fig. 8 Experimental ARPES spectra of few quintuple layers of bismuth selenide from ref [42]. Reprinted with permission from ref [42].

The above-mentioned insights from theoretical calculations contribute to draw perspective for future research on bismuth selenide both on experimental and theoretical sides wherein one can predict and suggest, deep understand, design and engineer the new devices based on topological insulator bismuth selenide nanostructures and shed lights on the novel materials for future green energy

View Article Online
DOI: 10.1039/D5MA00876J

applications. Here, we suggest using the concept of Goldsmith rule for ion exchange within the lattice [113] and a comprehensive check to make a library of various prototypes with different potential applications. Also, due to the similarity of layered structure of bismuth selenide with PbI_2, the adoption of two-step deposition method from perovskite solar cell materials [119] for bismuth selenide can possibly come to new materials such as two-dimensional layered , and hybrid 2D-3D structures and intercalation of different organic molecules in the interlayer spacings of the lattice. Moreover, the same chemical bonding concepts *i.e*. the octahedral chemical bond length and angle impacts on the bandgap and material unit cell volume; and the corresponding tight binding description can be explored to further shed light into basic understanding of this class of topological insulator materials.

5. Material synthesis

Different technologies have been used as synthetic method for bismuth selenide so far. The reproducibility, stability, cost and time, control on the growth, capability to integrate with device technologies and accessibility are important parameters for making a decision or preference. In commercial applications, reaction time and price of the precursors/equipment play role on the whole processes. However, the growth temperature, control, and engineering of the growth and how the material can be integrated/transferred in a special device structure dictate the potential application of the method. We in this section present examples of nanostructured growth and compare the methodologies; comparative summaries are presented in **Table 5-6**.

5.1. Chemical vapor deposition (CVD)

Here, reactants in the gas phase introduced and adsorbed on the substrate where a chemical reaction takes place and the nucleation and the growth of the material continue. The CVD deposition ofnanostructures take places directly on the substrate excluding the presence of solvent and additives, etc. Liu et al. have grown multi layered nanostructured bismuth selenide where selenium and bismuth powders were evaporated in the CVD tube. They carried with argon gas to the silicon substrate - decorated with Au nanoparticles - in 550 degree centigrade [120]. Brom et al. in another work [20] made Bi_2Se_3 hexagonal nanopillars using a sapphire [0001] substrate, a 220-540 degree centigrade temperature, tri-methyl bismuth(TMB) and Se pillars as source and hydrogen carrier gas. The temperature and growth procedure optimized in order to have the best substrate coverage and less selenium vacancies (**Fig. 9**). Few micrometre sized high quality platelets and nanoribbons of bismuth selenide have grown by Alegria et al. via a metal organic chemical vapor deposition (MOCVD) method using diethyl selenium and trimethyl bismuth precursors, hydrogen carrier gas, 470 degree centigrade temperature, 100 Torr chamber pressure and gold nanoparticle decorated silicon substrate[19]. Vapor-liquid-solid (VLS) mechanism can explain the growth mechanism of as-synthesized structures on gold decorated silicon [100] substrate.

Selenium vacancies are more likely to be formed during the growth due to a lower formation energy; therefore a selenium rich environment should be created inside the reaction tube wherein the defect density cab be even controlled via modifying the vapor pressure of selenium[19,20]. Thermodynamics, the relation between the geometry, pressure and temperature, concentration of the reactants, surface energies at boundaries together with transport of the reactants via drift or diffusion are key parameters. They rationalize the nucleation, growth, crystal orientation and vacancy concentration and physical properties of the as-grown products. Mica, graphene, and h-BN are the other common substrates for the epitaxial growth of bismuth selenide vie chemical or physical deposition techniques.

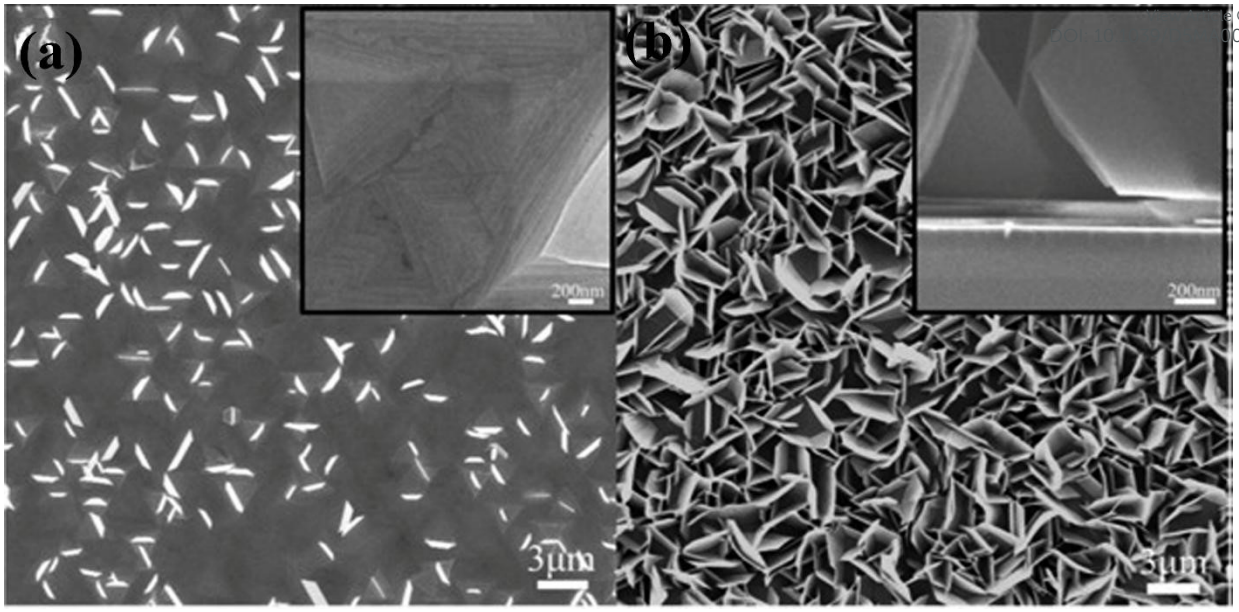

Fig. 9 SEM images of bismuth selenide sheets grown via CVD at substrate temperature of (a) 260°C and (b) 280°C. The inset in (b) is a cross-section image of the sample. Reprinted with permission from ref [20].

5.2. Chemical Route synthesis

Chemical reactions inside a solution have been one of the most straight forward and widely implemented low-cost synthetic routes for the design and engineering in the growth of nanostructures of different types. Here, the growth mechanism is depending on the temperature and pressure inside the vessel, the supersaturation fluid dynamics inside (*i.e.* stirring), time, the adsorption energies of additives and reactants on the nuclei crystallite, Zetta potential and even the environment humidity and lighting. Therefore, the morphology size and quality of the as-grown nanostructures and corresponding physics of the structures can be tuned. The selection of solvent and precursors however is more dependent on and restricted to the desired device with already deposited layers. Therefore, the post deposition of the as-grown products on a substrate after the synthesis thus is the solution for device fabrication purposes. Here a few examples represented.

The chemical synthesis of bismuth selenide via solution processed methods (*i.e.* hydrothermal, solvothermal, etc) results in very high quality single crystalline domain bismuth selenide hexagonal nanosheets. The typical precursors are selenium powder, bismuth nitrate and conventional solvents like water and ethanol. The surface adsorption and growth energy is very anisotropic for rhombohedral lattice of bismuth selenide, here the consecutive bismuth and selenide layers along the c-axis connected to each other through the weak Van der Waals forces. However, the chemical bonds for incoming atoms for in-plane atoms are of covalent nature and a directional preference for thermodynamically driven in-plane growth exist. This results in very high quality hexagonal nanosheets with very fine facets and few layers' thickness (**Fig. 10**)

Razzaque et al. [121] have grown bismuth selenide nano cubes (size less than 100 nm) via colloidal route: injection of metal organic precursors in about 200 degree centigrade under Nitrogen atmosphere and

vigorous stirring for water splitting purposes. The as grown products post deposited on glass substrate using aerosol spray deposition (with a rather poor adherence) and the growth parameters were optimized. The relevant stoichiometry of resulted films was rather significantly tuned by temperature adjustment. A surface oxidation of the products studied by X-ray photoelectron spectroscopy (XPS) was due to the presence of a capping agent precursor inside the solution[121].

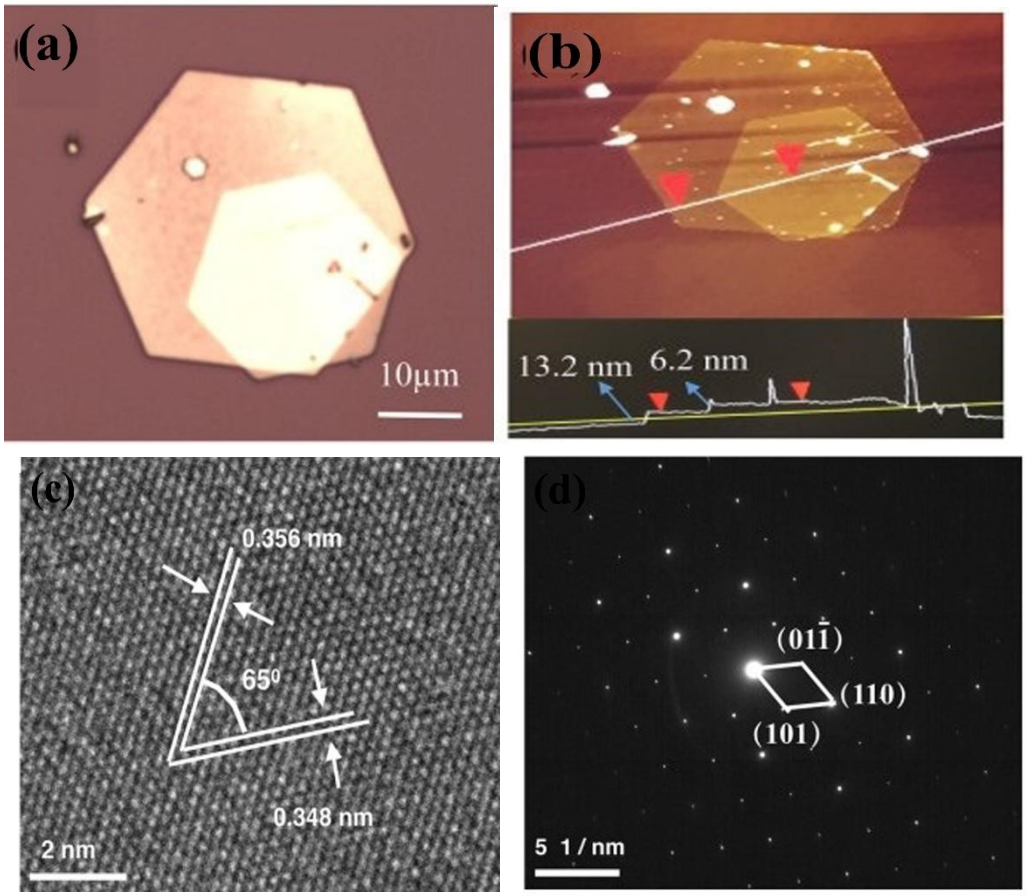

Fig. 10 (a,b) Optical image of stacked Bi2Se3 nanoplates and AFM. (c) HRTEM and (d) Electron diffraction pattern of solvothermally synthesized bismuth selenide sheets by Liu et al. Reprint with permission from ref [122].

In the work of Pradhan et al., a different bismuth precursor bismuth acetate together with short chain amine and acids and an organic solvent octadecene in lower temperature of 100 degree has been used for the chemical synthesis of nanosheets [123]. As doping in solvothermal method is easily done via addition of dopant salt, the same methodology has been implemented for the metal doping of bismuth selenide nano sheets for example in Refs. [11,123].

5.3. Exfoliation

Liu et al. [124] have made a photodetector on flexible substrate from bismuth selenide nanosheets with exfoliation method (**Fig. 11a**). In summary, bulk bismuth selenide grinded in a mortar and then ultrasonicated with NMP solvent for 24 hours, washed and dispersed in water. In this top-down synthesis approach, the mechanical forces exerted on the bulk bismuth selenide must be stronger than

View Article Online
DOI: 10.1039/D5MA00876J

vdW forces in between the atomic layers which results in cleavage and exfoliation of the material. One has not a full control on crystallinity and shape of the structures. The bottom-up approaches such as CVD and solvothermal are more favourable for device applications; however, it is attracting due to the cost and easiness. In another work, Hong et al. made the more controlled exfoliation of QTLs via atomic force microscopy tip (**Fig. 11b**) down to 1 QTL[35]. Here, when the horizontal force induced via AFM tip is large enough, the Bi-Se bonds can be broken, therefore the upper part of the bismuth selenide will be scratched away. By controlling the lateral force and vertical position of the tip, it is possible to remove most of upper QLs and have intact ultrathin Bi_2Se_3 at the bottom [35].

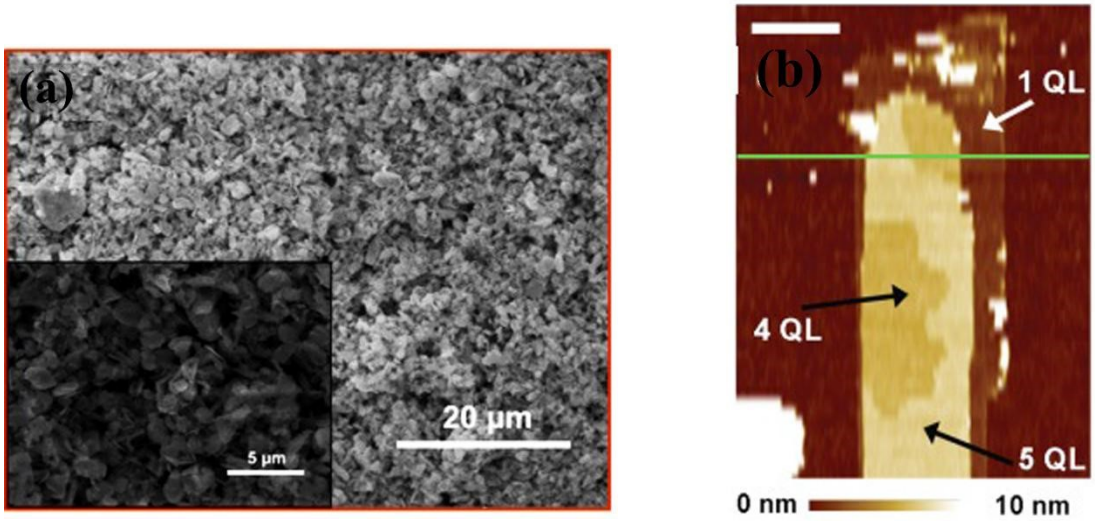

Fig. 11 Exfoliated bismuth selenide a) SEM image of sheets grown by Liu et al. Reprinted with permission from Ref [124]. b) AFM image of nanoribbons. The exfoliation can be done until 1 QTL. Reprinted with permission from ref [35].

5.4. Molecular beam epitaxy (MBE)

In molecular beam epitaxy one can control the film formation atom by atom. Here, in the expense of high vacuum and higher cost, one can obtain decent film quality and crystal growth. Precursor powders are heated up in Knudsen cell and a typical pressure of 10^{-10} Torr and a substrate temperature of about 200 ^{O}C gives a uniform thin film [125,126]. Here, with having a proper substrate one can tune the thickness to be few QTLs. For example in one of the very early experimental verifications of the Dirac cone in bismuth selenide, they used MBE to produce films with 1-6 individual QTLs[42]. The deposition rate can be for example 0.67 Å per minute in this method[127]. h-Boron nitrate[128] , indium phosphate[129], silicon[130], SiC [42], aluminium oxide[125] and amorphous SiO_2 [127] are among the substrates that have been so far used. A 7QTL MBE-deposition of bismuth selenide on $Bi_2Ca_2Cu_2O_8$ superconductor in 2013 resulted to observation of proximity effect and the discovery of superconducting states of topological insulator surface states. That was one step towards the observation for formation of Majorana fermions in these materials [131]. Springholz et al. have done Monte Carlo simulations to simulate the MBE growth and compared the results with experimental data [132].

View Article Online
DOI: 10.1039/D5MA00876J

5.5. Other deposition approaches and crystal growth from solid state reactions

For large scale bulk single crystals different solid-state reaction from melt such as Bridgeman method [133] have been used earlier; that we refer the reader to Refs. [2,13,106,110,134,135] for further reading. Other deposition approaches such as physical vapor deposition [136], sputtering [137], electrochemical deposition [138,139], bacteria-mediated growth [140], Nano-sculpturing [141], pulsed laser deposition (PLD) [142,143], and SILAR [144,145] have been implemented to deposit the nanostructures of bismuth selenide. Lithographic approaches have also been implemented, coupled to patterning the nanostructures on substrate using solvent stamping via van der Waals epitaxial growth reported by Zheng et al. [146]. In practical and commercial applications however, a competition between the yield, cost, integrability, convenience, time, etc play the main role for having a specific methodology for the device fabrication. **Table 5** compares different synthetic approaches from this sense and some typical examples including the growth precursors, temperature and pressure is afterward presented in **Table 6**.

Table 5. A comparison between the implementation of different synthesis approaches.

Method	**CVD**	**MBE**	**Chemical**	**Exfoliation**
Cost	Medium	High	low	Low
High-Tech	😊	😊 😊	**X**	X
Ease	yes	No	yes	No
Controllability	high	Super	good	Low
Tedious	😊	😊 😊	😊 😊	😊
Integrability	Decent	Decent	Difficult	More Difficult

Table 6. A summary for the synthesis of bismuth selenide materials via different approaches

Method	**Typical Precursors**	**Temp / Pressure**	**Morphology**	**References**
Melt Grown crystal growth	Bi, Se powders	850 ^{O}C	Crystal, Single crystals	110,134
Bridgman Method	Elemental Bi, Se	750 ^{O}C	Crystals	133
Solvothermal Hydrothermal	Bismuth: Bi, $Bi(NO3)_3$.$5H_2O$, $BiCl_3$, Bi_2O_3 Selenium: Se, SeO_2,H_2SeO_3, Na_2SeO_3	About 200 ^{O}C Autoclave(0.05mTor) Several hours till 2 days	Nanowires, Sheets, Tubes, Flakes, Films, Ribbons	147–150
Microwave assisted synthesis	Bi, Se powders $BiO(NO_3)$ $Bi(NO_3)_3$.$5H_2O$ Na_2SeO_3 Ethylene glycol	180 °C/1 minute/ power of 1000 W 2.45 GHz	Nanowires Nanoflakes	151,152
SILAR	$Bi(NO3)_3$.$5H_2O$ Na_2SeO_3 On FTO	Room Temperature	Nanoparticulated film	144,145

View Article Online
DOI: 10.1039/D5MA00876J

MBE	Bi and Se sources	300 ^{O}C	Thin film	125,126
PVD	Bi_2Se_3 powder Ar carrier ga Si (100)substrate	3 mTorr 700 ^{O}C	Thin-film	136,153
CVD	Bi_2Se_3 & Se powders	550-700 ^{O}C 8x10^{3} pascal	Nano-Wires, sheets, Thin-film	154–156
PLD	Bi_2Se_3 target	Excimer laser 5.5 J/cm2 350 ^{O}C 4x10^{-6} torr	Thin film, Hexagonal sheets	142,143
Exfoliation	Bi_2Se_3 Material	On Si/SiO_2 substrate	layered film-nanoribbon	35,124
MOCVD	TMBi and DESe Gold deposited Si	480 ^{O}C Hydrogen carrier	Nanoflakes	19,157
Patterning approaches	PDMS stamp Bi_2Se_3 powder	Ar carrier gas 50 mTorr	Nano-sheet arrays	146
Electrochemical deposition	$Bi(NO3)_3$, 5 H_2O SeO_2, HNO_3	Room temperature On ITO	Nanostructured film	138,139
Chemical bath deposition (CBD)	$Bi(NO3)_3$ .5H_2O Na_2SeO_3	80 °C/200 min On TiO_2		158
Sputtering	Bi_2Se_3 target	3 mTorr Ar 30W dc 10W RF/425 ^{O}C	Film	137,159
Nano-sculpturing	Bi_2Se_3 flakes	Via TEM	Ring, wire, antidot, etc	141

6. Characterization of Bismuth Selenide

Characterization is considered as the basic tool to study, engineer and foreseen the physical properties and potential device characteristics for the bismuth selenide materials and devices. It is based on the related underlying fundamental physics and is of crucial importance for research development in this area. Different kinds of characterization such as material physical characteristics measurement, advanced electronic structure and spin texture measurements, device stability against water and oxygen for long term operations and the collective behaviour of electronic charge and spin are mainly classified within device and material characterization techniques. These have been so far followed experimentally and theoretically. . Among these techniques, there are various methods on bismuth selenide such as the Raman spectroscopy [160,161], Angle resolved photoemission spectroscopy(ARPES) [3,86], spin- and angle-resolved photoemission spectroscopy (SARPES) [86,162] X-Ray photoelectron spectroscopy (XPS) [163,164] and electron energy loss spectroscopy (EELS) [163,165], Ultra-violet photoelectron spectroscopy (UPS) [166], scanning tunnelling microscopy (STM) [167,168], electrochemical characterization [121,169], Hall effect measurements [170], electron and Neutron diffraction[171] , and Shubnikov-de Haas measurements [9,172] , temperature dependent conductivity and magnetoresistance (*i.e.* Hall measurement) [57] , thermal conductivity [173], magnetic susceptibility and torque magnetometry [168,174], X-ray

View Article Online
DOI: 10.1039/D5MA00876J

absorption (XAS) [175], atomic/Kelvin/piezoelectric force microscopy (AFM,KPFM,PFM) [176], nuclear magnetic resonance (NMR) [177],Terahertz and laser spectroscopy [17,178,179].

In order to highlight the topologically protected surface states and implement them for device application, one approach is to reduce the contribution from bulk states via bulk doping or having smaller nanosized structures with higher surface to volume ratio. To characterize this, different techniques can be used. Zheng et al. have introduced a new approach for enhancement of bulk conductivity and improvement of the surface conductivity via tuning the formation of Bi_2Se_3 few-QTL films over the Bi_2Te_3 few-QTL films with different thicknesses [180]. In Hall conductivity measurements, however the collective contributions from both bulk and surface states appear in the measured data; Instead in Terahertz spectroscopy [179] measurements one can measure *i.e.* the temperature dependence mobility and carrier density of surface states deconvoluted from bulk states.

Thermoelectric power generation is the widely investigated and initially triggered device target for bismuth selenide [181]. Field emission [108] and field effect transistors [182] as well. Today the potential applications go through the photodetector, batteries, medical imaging and cancer therapy, gas sensors, biosensors and more (See section 7). These device architectures need their own characterization methodology. Here the semiconducting behaviour is in the focus for device applications and the characterization of defect/doping density; and Fermi level tuning is an important issue. Superconducting states also observed at low temperatures for Nb- , Sr- and Cu- doped bismuth selenide materials [168,174,183].

Bismuth selenide -as mentioned- is a n-type semiconductor due to the thermodynamically favourable formation of selenium vacancies during the growth. Shirodkar et al. in a computational/experimental study have showed that the selenium vacancy defect states can be healed via oxygen adsorption at the surface [184]. Walsh et al. [185] have reported about a very fine-tuned with nearly free selenium vacancy synthesis of bismuth selenide having the Fermi level almost at the middle of the band gap. They have also showed that with careful annealing and monolayer de-capping, one can tune the Fermi level near the upper half of the gap. In addition, chemical n-type/p-type switching of bismuth selenide nano-ribbons via reversible cupper doping/intercalation is reported by Xiong et al. [186].

Energy levels of the photogenerated electron and holes, and their dynamics *i.e.* time constants of thermalization and e-h recombination processes are essential determining factors for device performance. Studied by Jnawali et al. [17] via laser spectroscopy (mid infrared femtosecond transient reflection) measurements, thermalization kinetics of excited electron-hole pairs estimated to be about a couple of picoseconds. The excited bulk carriers behave like a dense electron gas with recombination time constant of 150 ps and 50 ps at 10K and 300K respectively. Electron-phonon interaction has the key-role in thermalization processes; Huang et al. in a combinational study using time-resolved XRD and angle-resolved photoemission (ARPES) techniques quantified the mode specific electron-phonon couplings for the bismuth selenide and telluride surface states[187]. Very recently, charge transfer kinetics and electron-phonon dynamics of Bi_2Se_3 heterostructures with perovskite solar cell material $CH_3NH_3PbBr_3$ has been investigated by Sharma et al. showing their potential promise for solar cell applications [178].

View Article Online
DOI: 10.1039/D5MA00876J

Local optical properties of CVD-grown bismuth selenide nano sized beams (called nanobeams with mean size about 700x300 nm) have been studied by Nandi et al. [22] via nanoimaging phase mapping characterization. The as-grown films show a very high refractive index of 6.4 for mid infrared light and the phase mapping reveals local domains with different shifts with different scattering yields for unpolarized and different polarized light. This thus provides information about the local optical properties of bismuth selenide nanostructures [22]. Das et al. have studied the visible light optical properties of PVD-grown films and annealed at different temperatures reported in ref [24]. Ellipsometry measurements of bismuth selenide optical properties for different nanostructures of bismuth selenide are reported by Yang et al. in Ref. [188].

The bismuth selenide structures are prone to be protective and robust against the water and oxygen (air attack) which is essential for device operation. The water and oxygen stability of bismuth selenide has been studied in Ref. [164]. It was shown that there is negligible reactivity of bismuth selenide with water and oxygen and surface oxidation of bismuth selenide in dry air happens in time scale of years. This together with higher stability and lowed degradation of structure with topologically protected surface states makes them good potential candidates for several applications. For example, the field emitters based on bismuth selenide are reported by which show a turn-on voltage of 2.5 v/μm and current density of about 180 μA/cm^2 [108]. Theoretical calculations shows that even in the case of oxidation the topologically protected surface states remains robust and the electronic structure of surface states remains unchanged [189]. A similar metal chalcogenide compound based on tin $Sn(S_{0.92}Se_{0.08})_2$, implemented in tin-based perovskite solar cells as charge selective layer to supress the well-known oxidation of Sn cations inside the film via circumventing the oxygen desorption enhances the stability of the solar cell. Proper energy levels and excellent stability against water and oxygen resulted in a high performance of highly stable perovskite solar cell with power conversion efficiency (PCE) of 11.78 % [190].

Surface wettability is an important factor for both device stability issues and liquid-phase deposition of extra layers in device fabrication. Surface wettability of PVD-grown bismuth selenide is studied via Das et al. [24]. They annealed the films under different temperatures and found that the crystallite size increases from 14 to 24 nm for films without annealing and annealed from 100 to 250 degree Celsius. The contact angle with water showed an increase from 99 to 120 degree respectively. Goncalves et al. however have showed the presence of other Bi_xSe_y phases inside the bismuth selenide after annealing at temperatures higher than 300K [191].

The characteristics of other bismuth chalcogenides such as bismuth telluride and sulphide also shed light into better understanding and rapid development of devices based on Bi_2Se_3 materials. **Fig. 12** presents a few results about the experimental characterization of bismuth selenide materials and devices mentioned above.

View Article Online
DOI: 10.1039/D5MA00876J

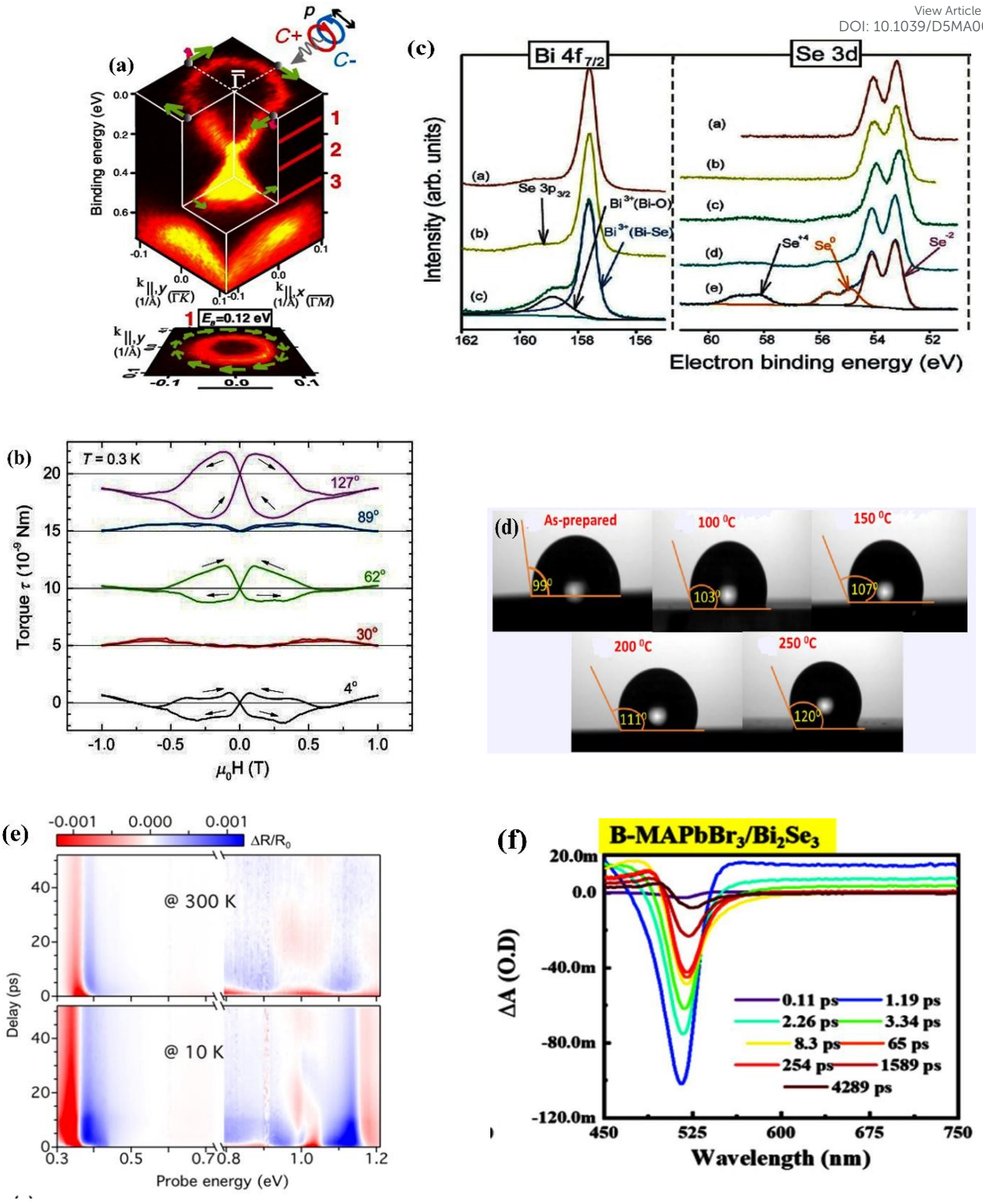

Fig. 12 Examples for experimental characterization of bismuth selenide materials and devices. (a) SARPES spectrum showing the electronic spin texture. Reprinted with permission from ref [162]. b) Typical torque curves measured from torque magnetometry at 0.3K reprinted with permission from ref [174]. (c) XPS spectra and the corresponding evolution of bismuth and selenium core electrons before and after exposure to humidity. Reprinted with permission from ref [164]. (d) Contact angle images of samples annealed at different temperatures. Reprinted with

View Article Online
DOI: 10.1039/D5MA00876J

permission from ref [24] e) a typical transient reflectance spectrum measured at 300K and 10K with pump wavelength of 1.5 eV. Reprinted with permission from ref [17]. f) transient absorption spectra for $MAPbBr_3$ perovskite heterostructure with bismuth selenide showing signature of the photoinduced absorption and ground state bleach. Reprint with permission from ref [178].

Point defects are widely implemented to tune material optoelectrical properties. The understanding and the level of our control on mesoscale defects and domains in bismuth selenide is rather limited yet and new probes to characterize the relevant carrier dynamics necessitate novel probing tools specially to study the topologically protected surface states and corresponding optical properties[192]. On the other hand, in order to specifically probe transitions between the surface-protected states, a joint theoretical/experimental approach with new characterization methods seems to be crucial to achieve a full understanding and the complete picture of Bi_2Se_3 photo-physics. Still, the picture is not complete and many recent publications trends goes towards this direction.

7. Green energy devices based on bismuth selenide

7.1. IR-Photodetectors

Infra-red photodetectors have a wide range of novel applications in military, space industry, astronomy, and remote imaging. Here different materials have own benefits and drawbacks and the commercial ones produced in military and *i.e.* NASA for detection of black holes in astronomical applications which still need further developments. Bismuth selenide is one of the materials with band gap laying in the far infra-red/Terahertz region making it potentially specific for special applications. However, Photovoltaic effect-, photoconductivity effect-, photo thermoelectric effect- based IR detectors have different underlying mechanisms. They are stemming respectively from self-driven selective accumulation of opposite charges under illumination, incoming photon triggered enhanced conductivity and thermal gradient based electrical currents based on heating effects. One needs to use the proper characterization technique and play with conductivity, mobility, absorption coefficient, exciton lifetime, electron transport time, etc, in order to control and improve the device performance. Here, the most important parameters for characterization and practical potential investments are noise ratio (ratio between light and dark currents), detectivity, responsivity (ratio of incident photons flux P_{in} and the output current Ip) and response time (time span for photocurrent rise after light-on) which are briefly described in Ref. [193]. We refer the reader to Ref. [194] for more information about different working conditions, type-mechanisms in Infra-red photodetectors and commercial examples.

Liu et al. have reported about the implementation of bismuth selenide nanosheets in a device based on the paper substrate which has shown excellent responsivity at 1064 nm IR light with acceptable stability under different bending conditions [124]. Here, the IR light driven photoconductivity of bismuth selenide detects the incidence of infra-red light (**Fig. 13**).

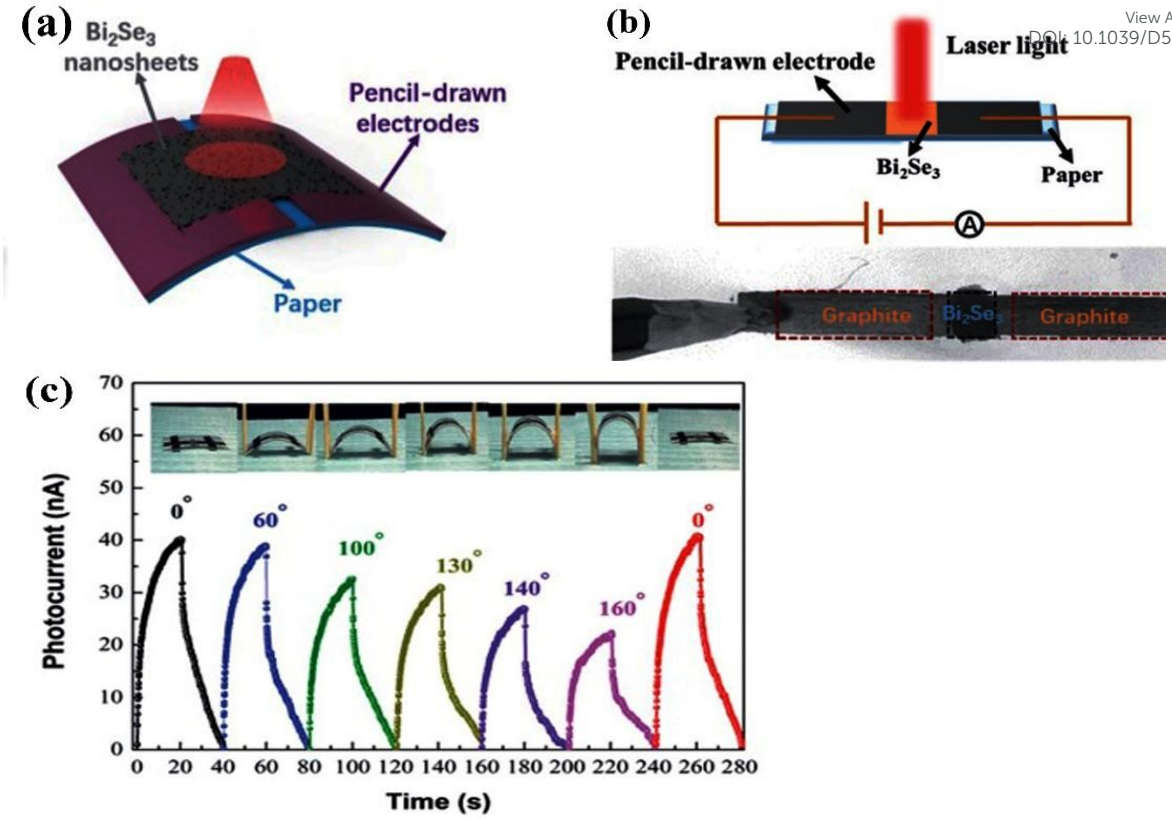

Fig. 13 a) Schematic of the bismuth selenide infrared photodetector device based on the flexible paper substrate, b) illustration of the corresponding photocurrent measurement, c) photocurrent rise and decay time (response time) under consecutive turning on/off of the incident light under different bending conditions. reprinted with permission from ref [124].

Zhang et al. fabricated a high performance photodetector device based on n-type silicon and bismuth selenide heterojunction structure (**Fig. 14**) [195]. In a separate study Wang et al., have used a heterojunction-based IR detector base on bismuth selenide/WO_3 wherein the interface band bending reduces the dark current noise and enhances the charge separation efficiency inside the device. This results in the 2D Bi_2Se_3/WSe_2 responsivity of $3AW^{-1}$ and detectivity of 2.2×10^{10} Jones for 1456 nm infrared [196].

View Article Online
DOI: 10.1039/D5MA00876J

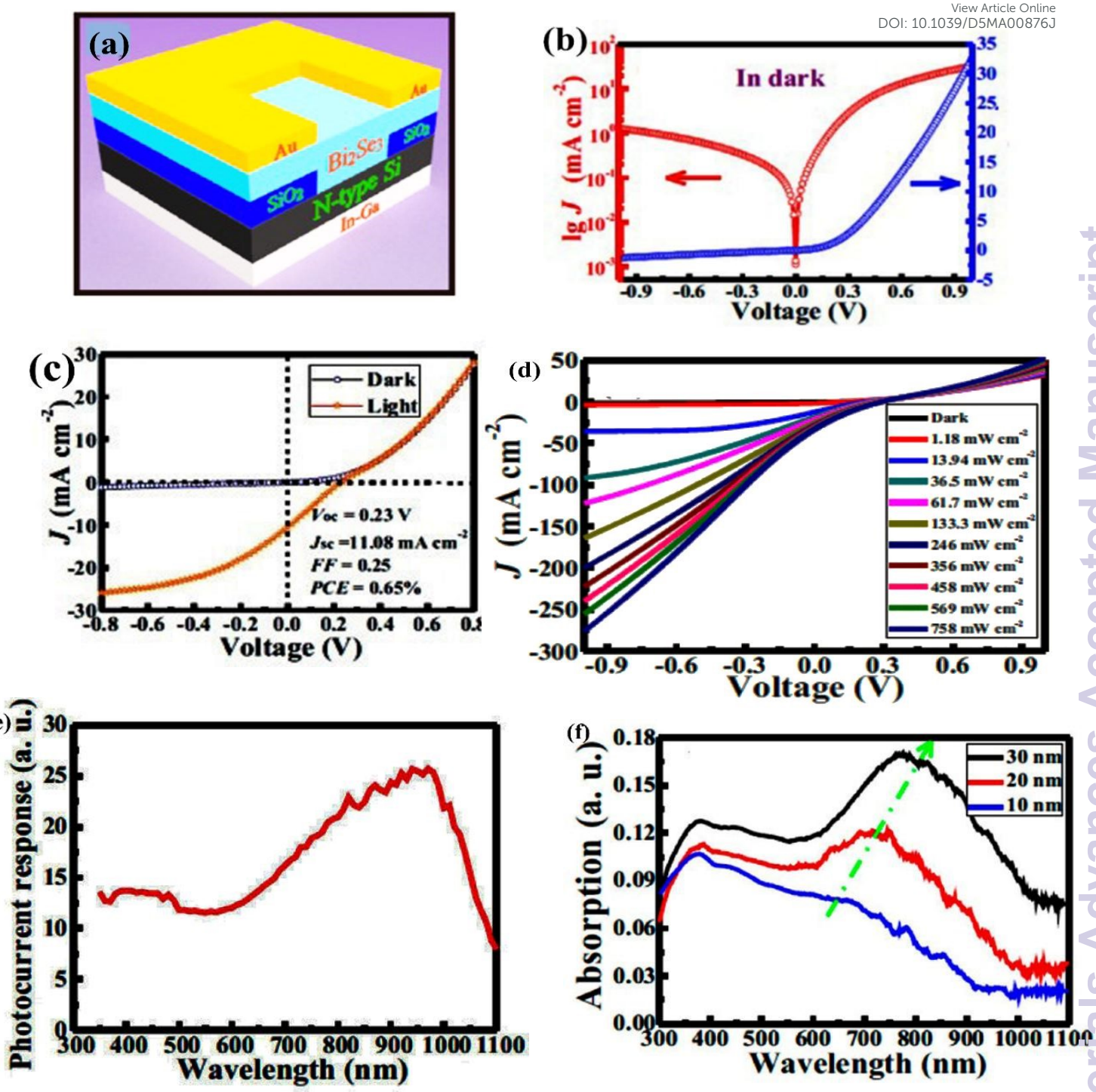

Fig. 14 (a) Schematic of the heterojunction device based on bismuth selenide and the (b-f) device characteristics (b) Dark current (c) photovoltaic effect under sun light (d) photocurrent under 808 nm NIR, (e) photocurrent response spectrum and (f) absorption spectra of device with different thicknesses. Reprinted with permission from ref [195].

Efforts have been made for bismuth selenide based photodetectors previously both in theoretical and experimental part, however the field is still rather young and in the stage of R&D (research and development). More studies needed to fully understand the underlying physics and overcome the

View Article Online
DOI: 10.1039/D5MA00876J

current practical limits such as slow response time in second time scale. Flexible photodetectors and wearable and portable devices, polarization sensitive detectors, heterojunction detectors, and doping effects are among the recent reports in Refs. [124,146,195–197]. Moreover, the surface protected topologically preserved surface states of bismuth selenide and the formation of spin coupled Dirac branches with spin-momentum lock (see section 3.3) make them specific for polarization detection capabilities *i.e.* the one reported in Ref. [27] and **Fig. 3**. Furthermore, similar efforts have done on bismuth telluride and also mixed phases such as Bi_2SeTe, $Bi_2Se_xTe_{2-x}$, $Bi_2Se_xTeyS_{2-x-y}$, … in order to further explore and expand the material properties and corresponding device performances which are beyond the scope of the current manuscript.

Sharma et al. have demonstrated that focused ion beam (FIB) fabricated Bi_2Se_3 nanowires can act as ultrasensitive photodetectors for visible and near-infrared light, achieving a photoresponsivity of approximately 300 A/W [198]. Zheng and colleagues developed a method combining micro intaglio printing with van der Waals epitaxy to create large-area Bi_2Se_3 arrays, and an external photoresponsivity of about 1,650 A/W [146]. This technique enabled the creation of large-area arrays of Bi_2Se_3 topological insulators, achieving a record Hall mobility of approximately 1,750 $cm^2/V{\cdot}s$ at room temperature. Additionally, their patterned crystal arrays were successfully integrated into flexible photodetectors.

Liu's study focused on how precursor temperature affects the growth of Bi_2Se_3 nanobelts for NIR photodetectors, yielding ultra-fast photo-response and high detectivity[199]. Hong et al. fabricated Bi_2Se_3 films on micro pyramidal silicon, enhancing light trapping and achieving excellent performance across a wide wavelength range[136]. The etching process was crucial for improving photo-response, and the devices demonstrated optimal performance after 30 minutes of wet etching. Overall, the micro pyramidal structure significantly boosts the photodetection capabilities of the Bi_2Se_3/Si heterojunction, indicating strong potential for infrared detection applications. Yang et al. introduced a Bi_2Se_3/MoO_3 heterojunction that exhibited exceptional responsivity and detectivity over a broad spectrum[200]. The response time was 63 microseconds significantly faster than ordinary bismuth selenide-based photodetectors.

Das et al. have created a heterojunction of Bi_2Se_3 nanoflakes and silicon nanowires, achieving a maximum photoresponsivity of 934.1 A/W [201]. They characterized the device via analysis of temperature dependent barrier height and ideality factor of the junction. Li et al. fabricated a copper-doped Bi_2Se_3/p-Si heterostructure, significantly improving the photocurrent after doping *i.e*. a 42-fold increase compared to intrinsic bismuth selenide[202]. Lu's work on a cascade heterostructure of bismuth chalcogenides demonstrated outstanding photodetector performance [203]. The convenient charge transport/transfer within this cascade heterostructure together with high incident-photon-to-current-efficiency (IPCE) makes it possible to implement them also as a photoelectrochemical splitting device for water splitting. Tang et al. introduced sub-millimeter terahertz detectors using a metal-Topological insulator-metal heterostructure, achieving high responsivity and fast response times [204].

Fig. 15-16 and Table 7 summarize the recent efforts and compare the corresponding performances presenting the schematic diagram of various photodetector devices based on Bi_2Se_3, the performance of the Bi_2Se_3 photodetector in terms of photocurrent switching and the summary comparison of the performance of different Bi_2Se_3 photodetectors. Overall, these studies underscore Bi_2Se_3's versatility and performance, positioning it as a key material for advancing photodetector devices.

View Article Online
DOI: 10.1039/D5MA00876J

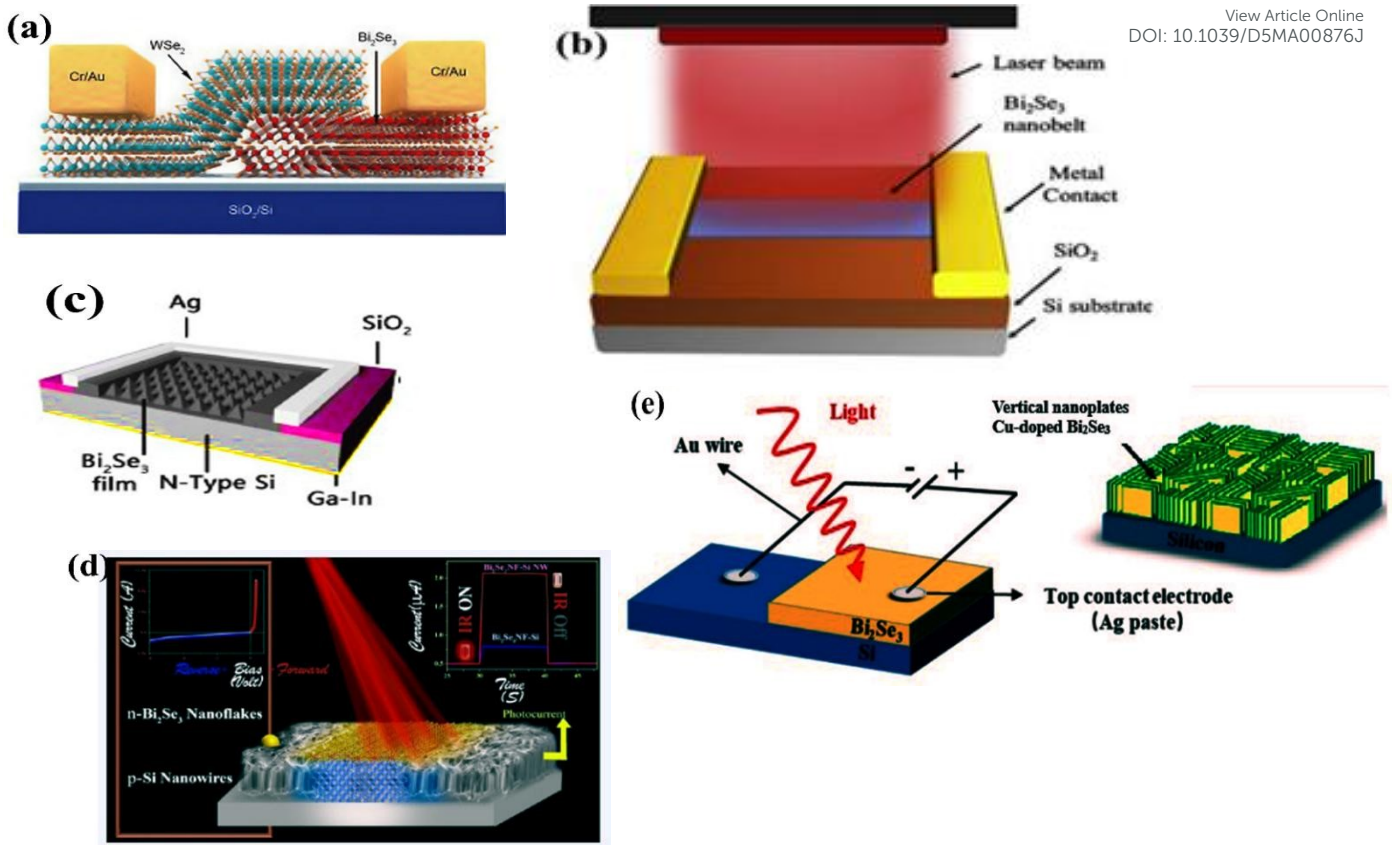

Fig. 15. Schematic illustration of a) the device based on a heterojunction between Bi_2Se_3 and silicon, Reprinted with permission from ref [196], b) the single Bi_2Se_3 nanobelt NIR devices, Reprinted with permission from ref. [199] , c) a Bi_2Se_3/n-type silicon-based device, Reprinted with permission from [136], d) Bi_2Se_3/Si-Nanowire heterojunctions, Reprinted with permission from. Ref [201], and e) vertical nanoplates of copper doped Bi_2Se_3/Si heterostructure photodetector device, reprinted with permission from ref [202].

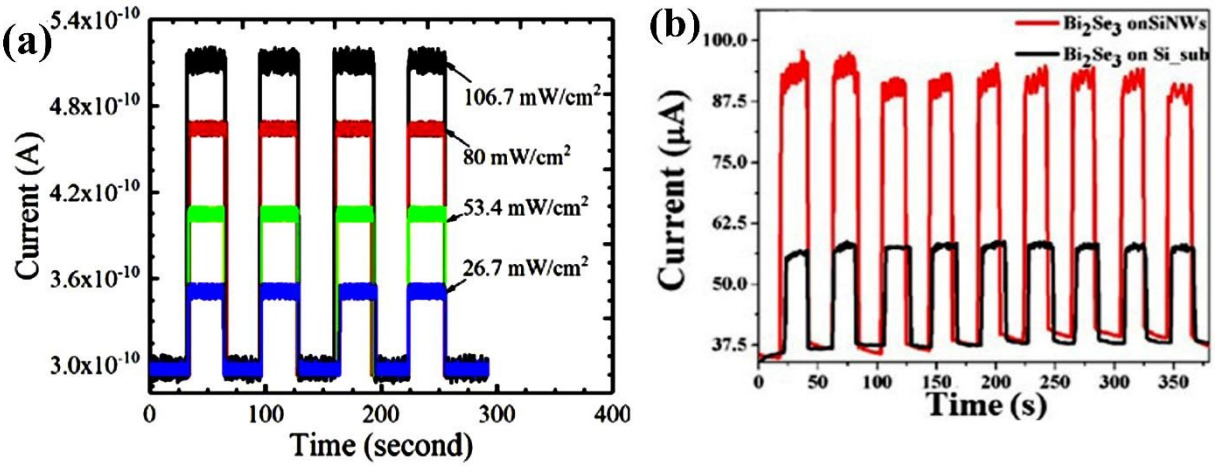

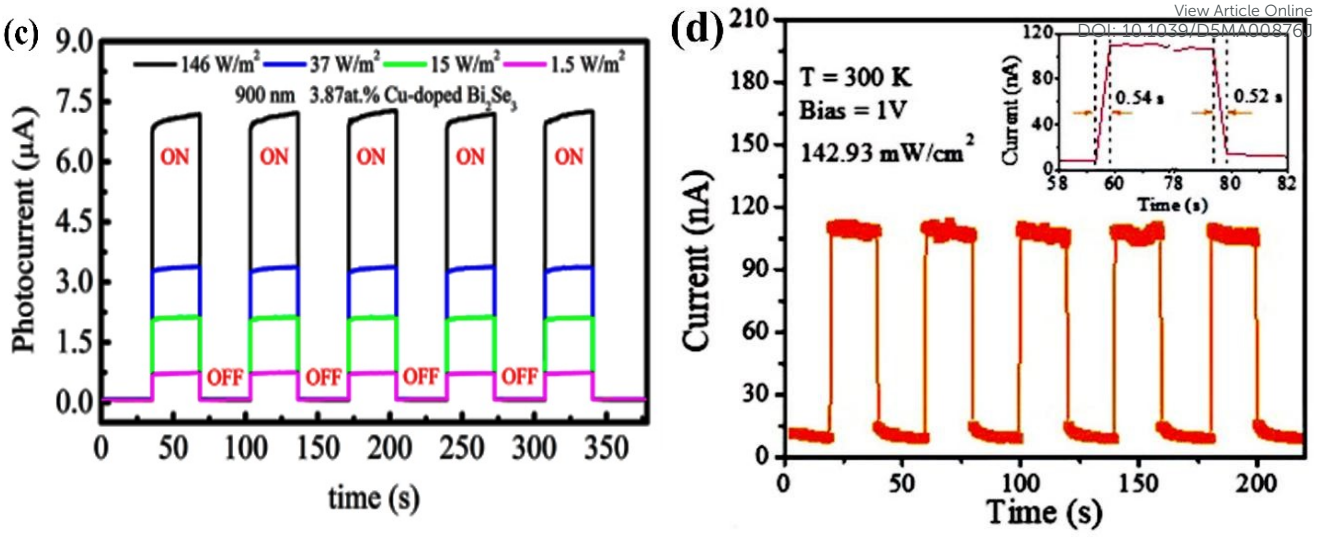

Fig. 16. Photocurrent switching performance of (a) the Bi_2Se_3 nanobelt photodetector reprinted with permission from ref [199], (b) of Bi_2Se_3 structures grown on pure Si substrate and Si nanowires, reprinted with permission from ref [201], (c) the Cu-doped n-Bi_2Se_3/p-Si photodetector under 900 nm and 146 W/m^2 light illumination with 3.87 atom % Cu concentration under different light intensities, reprinted with permission from ref [202], (d) the Bi_2Se_3 flake photodetector at a bias voltage of 1 V and an illumination power of 142.93 mW cm^{-2} reprinted with permission from ref [205].

Table 7. Performance Comparison of various Bi_2Se_3 Photodetectors

Materials	Detector	Growth method	Detectivity (Jones)	Responsivity (A W^{-1})	Risetime (s)	Ref
Bi_2Se_3 nanosheets	IR photodete	liquid exfoliation	-	26.69 × 10^{-6}	-	124
Bi_2S_3 nanosheets	Photoelectrochemical (PEC)-type photodetector	liquid phase exfoliation (LPE)	9.93 × 10^7	210× 10^{-6}	0.1	206
Bi_2Se_3 (thick flakes)	THz detector	-	2.17× 10^{11}	75	-	204
Cu-doped n-Bi_2Se_3/p-Si	Heterostructure photodetector	CVD	1.85×10^{11}	168.9 × 10^{-3}	-	202
Bi_2Se_3(Thin Film)/MoO_3	Heterojunction photodetector	MBE	5.79 × 10^{11}	2609	62×10^{-6}	200
Bi_2Se_3/Si (nanowire)	NIR photodetector	wet chemical route	2.30 × 10^{13}	934.1	0.041	201
Bi_2Se_3/ Si	NIR photodetector	wet chemical route	7.2 × 10^{12}	287.7	0.11	201
Bi_2Se_3 (nanowire)	NIR -detector	Focused ion beam (FIB)	7.5× 10^9	300	0.55	198

View Article Online
DOI: 10.1039/D5MA00876J

Bi_2Se_3 nanosheet (exfoliated)	Photoelectrochemical (PEC)-type photodetector	Hydrothermal	-	20.48×10^{-3}	0.7	207
Bi_2Se_3 nanobelts	NIR photodetector	Van der Waals epitaxy	4.63×10^{8}	10.1×10^{-3}	0.037	199
$Bi_2Te_3/Bi_2Se_3/Bi_2S_3$	Photoelectrochemical (PEC)-type photodetector	Sequential vapor phase deposition	8.96×10^{9}	103×10^{-3}	8×10^{-3}	203
Bi_2Se_3 (nanowire)/Si	Heterostructure photodetector	Thermal evaporation	2.38×10^{12}	924.2	0.045	208
Bi_2Se_3/micropyramidal Si	Heterojunction photodetector	PVD	1.24×10^{11}	7.16×10^{-3}	0.52×10^{-3}	136
Bi_2Se_3 flake	IR photodetector	Van der Waals epitaxy	3.3×10^{10}	2.74	0.54	205
Bi_2Se_3 flake (T = 80 K)	IR photodetector	Van der Waals epitaxy	8.0×10^{10}	23.89	0.54	205
Bi_2Se3/Si Heterostructure	Heterostructure photodetector	Epitaxial growth	4.39×10^{12}	24.28	2.5×10^{-6}	195
2D Bi_2Se_3/WSe_2	visible and NIR detectr	Van der Waals heterostructures	2.2×10^{10}	3	4×10^{-3}	196

To engineer and design new materials with enhanced properties for photodetectors, one needs to systematically probe the material library space and use fundamental insights from chemical bonding prospects and fine-tune the desired aspects. Alloying and mixing compounds with other bismuth chalcogenides is a great possibility to further shed light on the development of bismuth selenide-based photodetectors. Photodetectors based on topological insulator materials is reported in Ref.[209] and more informative reports about bismuth chalcogenide based photodetectors are mentioned in Refs . [210–212] Further insights can be elucidated from X-ray photodetector/scintillator devices based on various bismuth compounds wherein the high atomic number of bismuth is very beneficial for high X-ray antennation.[213]

7.2 Spintronics and quantum computing

Bismuth selenide is a prominent topological insulator that has been gained considerable attention in the field of spintronics due to its unique electronic properties, spin-momentum locking and the presence of protected surface states. Integrating Bi_2Se_3 with ferromagnetic materials has opened new avenues for exploiting magnetoelectric effects [1,214,215]. These researches explore how electric fields can influence magnetization and spin transport, potentially leading to innovative spintronic devices that leverage the interplay between charge and spin currents [216]. The bismuth selenide Dirac cone in the band gap allows the surface states electrons to have a very high velocity, mobility and long spin diffusion length and mean free path which is very attracting for spintronic devices. Furthermore, for the surface states electrons the spin is locked to the momentum which means that different spin currents can propagate in different directions in the presence of magnetic interactions with ferromagnetic layers. By leveraging the robust spin-polarized surface states of Bi_2Se_3 and investigating the effects of defects and heterostructure configurations, the studies collectively advance the energy-

View Article Online
DOI: 10.1039/D5MA00876J

efficient technologies capable of manipulating spins via electrical means. This comprehensive approach positions Bi_2Se_3 as a cornerstone material for future developments in memory and logic devices within the spintronics landscape [217]. Here, we summarize a few examples from the recent effort in manipulating and engineering the spin or spin-locked currents for spintronic and quantum computing potential applications.

In an investigation by Tang et al. for the quantum transport properties of heavily doped Bi_2Se_3 nanoribbons, it was revealed that the manipulating defects and doping levels can further enhance the spin transport characteristics, which is crucial for device performance [57]. Jozwiak et al. contribute to this understanding by examining the control of spin-polarized surface states, demonstrating that external magnetic and electric fields can effectively manage the spin dynamics—an essential factor for functional spintronic applications [218]. Mellnik et al. have focused on the generation of spin-orbit torque in Bi_2Se_3, providing evidence that this material can efficiently convert charge currents into spin currents [219].

In addition, Bi_2Se_3 also shows promise in quantum computing (See section 3.4). However, defect-induced bulk carriers can obscure the valuable surface states essential for these applications. Abhiram et al. have explored isoelectronic doping through ion irradiation using 600 keV antimony (Sb^+) ions on Bi_2Se_3 thin films. Their findings, based on Rutherford backscattering spectroscopy, revealed that heavy irradiation altered the magnetoresistance from a parabolic to a linear response, which was attributed to mobility fluctuations. This study highlights ion irradiation as an effective method for tuning quantum coherence phenomena in Bi_2Se_3, potentially enhancing its properties for both spintronic and quantum applications (**Fig. 17**) [220]. By carefully controlling the doping, mobility, structural integrity, and quantum coherence, it is possible to enhance the efficiency and functionality of spintronic configurations, paving the way for advanced applications in next-generation electronics [220].

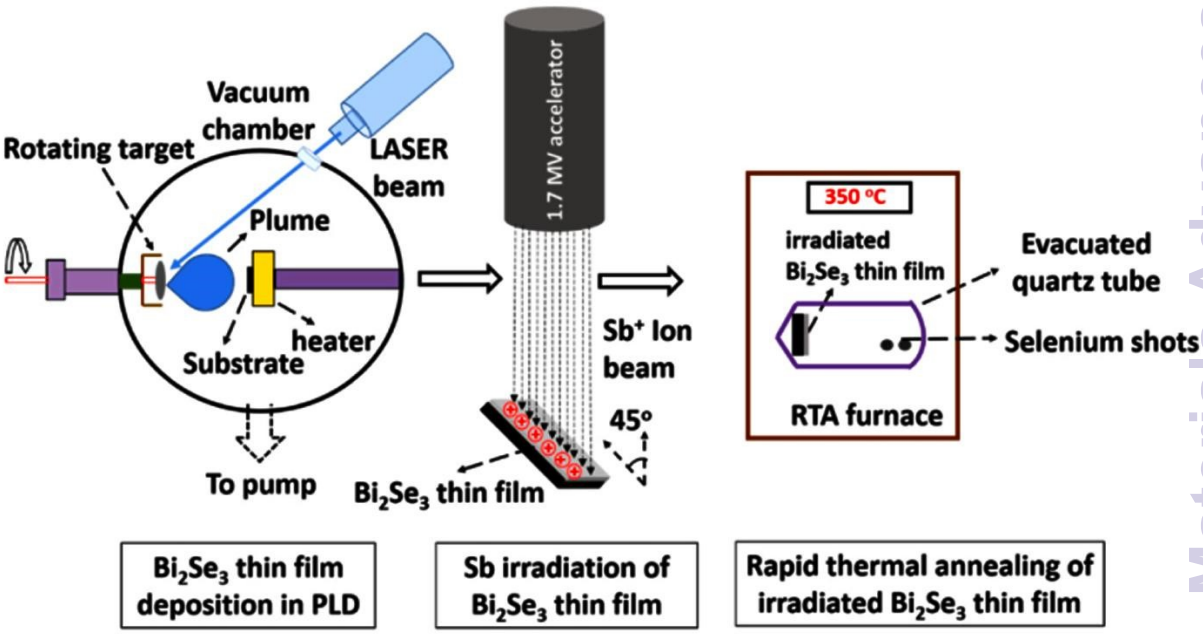

Fig. 17 Schematic of deposition, Sb-irradiation, and post-irradiation annealing of Bi_2Se3 thin film. Reprinted with permission from [220].

View Article Online
DOI: 10.1039/D5MA00876J

Li et al. investigated spin currents in Bi_2Se_3 by utilizing tunnelling ferromagnetic (FM) contacts while applying a charge current to the surface[221]. Their results indicated that the momentum direction of the carriers **k** locks the spin direction along the y axis, which is detectable via the FM contacts (Fe). The magnetic field-dependent voltage measured between the FM contacts and an Au contact showed sharp increases or decreases as the magnetization of the Fe electrode switched, depending on the alignment of the magnetization direction with the carrier spins [221–223].

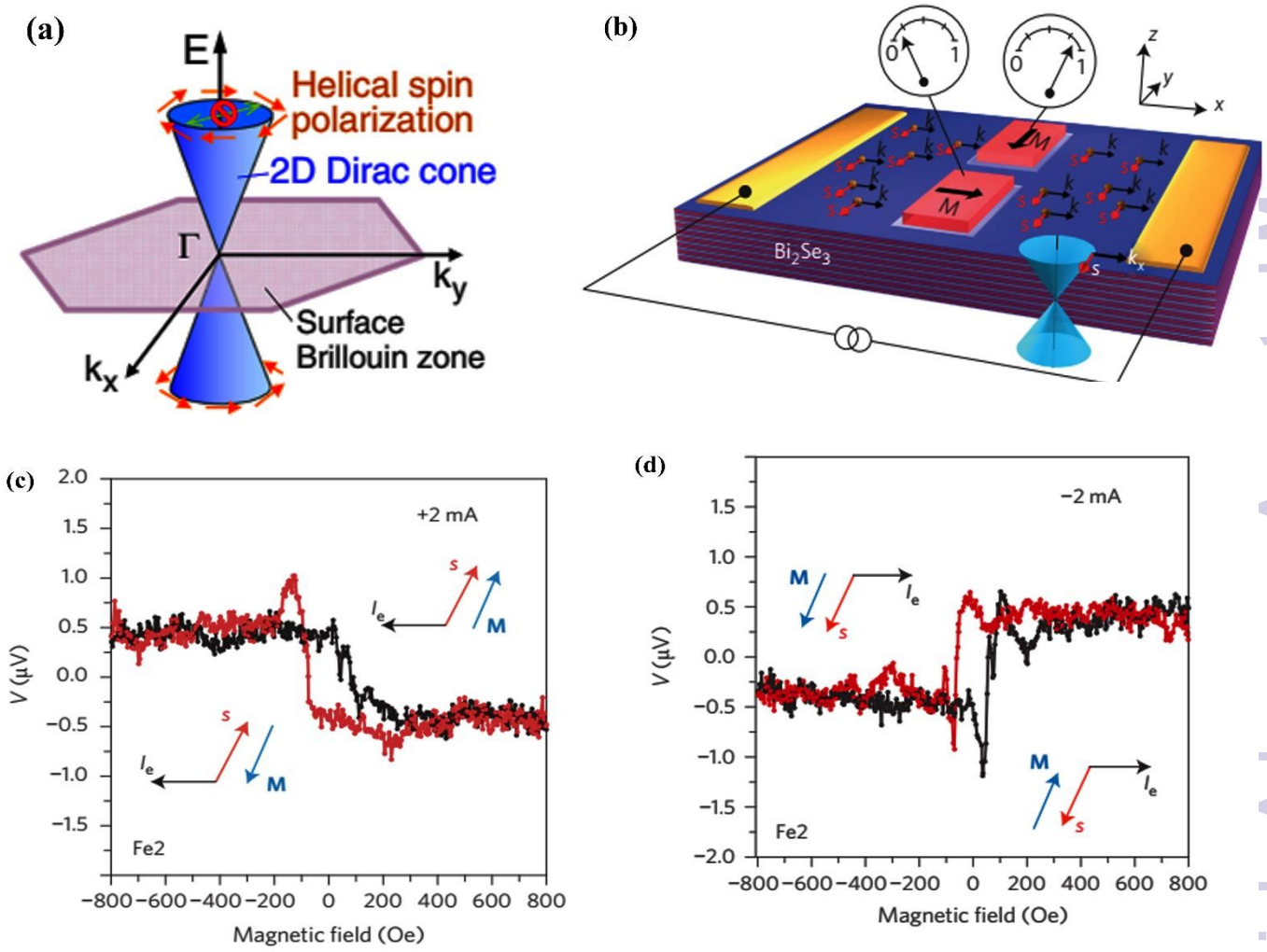

Fig. 18. Spin transport in the surface metallic states of topological insulators (TIs). (a) Schematic representation of spin momentum locking in the Dirac band of TI surface states. Reprinted with permission from Ref [224] (b) Conceptual illustration of the TI spin transport device structure, featuring a ferromagnetic (FM) electrode to measure the spin polarization of the conducting carriers. (c) and (d) Spin-dependent voltage as a function of the magnetic field for positive and negative 2 mA currents, respectively. Reprinted with permission from Ref [221].

A promising application of the spin Hall effect is the manipulation of the magnetization of an adjacent ferromagnetic layer through spin-orbit torque (SOT), here *i.e.* switching the magnetic moment for adjacent ferromagnetic layers. Spin−orbit torque relies on generation of spin current from charge

View Article Online
DOI: 10.1039/D5MA00876J

current in a nonmagnetic material which is a critical topic for spintronic devices and promise an energy-efficient scheme for manipulating magnetization in magnetic devices [225]. The spin-momentum locking present in the surface metallic states of topological insulators (TIs) provides an effective mean to generate spin currents and three dimensional topological insulators family and specially the bismuth selenide show orders of magnitude improvement in SOT efficiency at low temperature[224] . A notable breakthrough in this area was the observation of substantial spin-orbit torque at the Bi_2Se_3-permalloy (Py) interface, where Bi_2Se_3 exhibits metallic behaviour [219,222]. Researchers have employed the spin-torque ferromagnetic resonance measurements to probe two distinct torques—spin-orbit torque and Oersted field torque—around the resonance condition of the Py thin films [222,223]. Mellnik et al. could achieve a SOT efficiency of 2.5 and spin conductivity of 110-200 $x10^3$ ($\hbar/2e\Omega$ m) for Bi_2Se_3/Py junction [219]. Han et al. have implemented a Bi_2Se_3/CoTb layer with perpendicular magnetic anisotropy at room temperature and shown the switching via current induced magnetization as presented in **Fig. 19** [226]. A similar work on Bi_xSe_{1-x}/Ta is presented in **Fig. 19b** from Ref. [227].

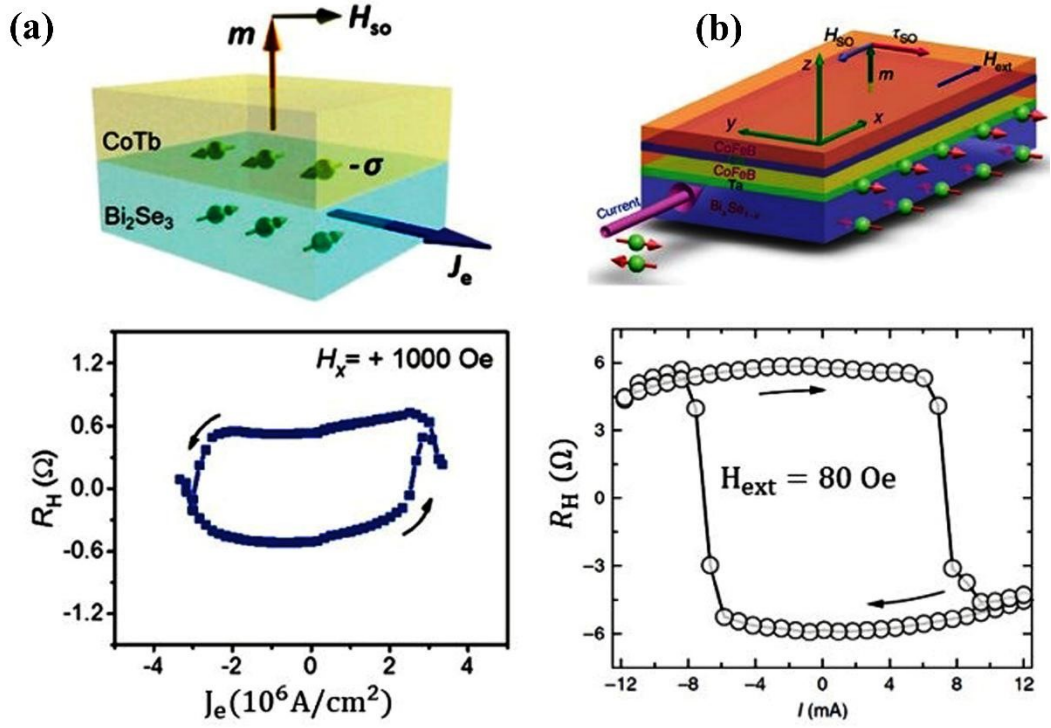

Fig. 19. Current-induced magnetization switching in bismuth selenide-based architectures (a) Bi_2Se_3/CoTb and b) Bi_xSe_{1-x}/Ta. Reprinted with permission from ref [226,227].

Magnetic doping is crucial for breaking time-reversal symmetry in the surface states of TIs, leading to novel physical phenomena and technological applications. Liu and colleagues focused on chromium-doped Bi_2Se_3 in its ultrathin form, which is anticipated to exhibit the quantum anomalous Hall effect (QAHE) [228] (**Fig. 20**). They successfully produced high-quality $Bi_{2x}Cr_xSe_3$ epitaxial thin films using molecular beam epitaxy (MBE). Their findings suggest that the coexistence of ferromagnetic and antiferromagnetic chromium defects accounts for the lower magnetic moments observed in conventional magnetometry, which are significantly below the 3 μ_B per chromium atom predicted by Hund's rule [228]. The ferromagnetic quantum anomalous Hall effect was separately observed by Moon et al. in a Cr-doped 10-QL Bi_2 Se_3 layer on Al_2O_3 substrate. They also studied the shape of the

View Article Online
DOI: 10.1039/D5MA00876J

hysteresis/magnetoresistance relation via a tight binding model and demonstrated that the Berry phase calculations including the Cr-induced Zeeman effects can reproduce the QAHE results [229].

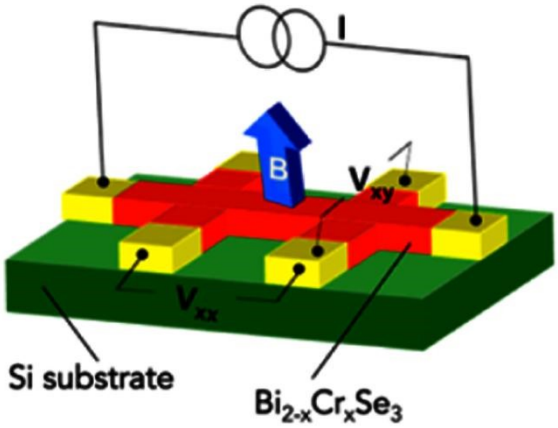

Fig. 20 Schematic diagram of the experimental setup of the quantum anomalous Hall (QAH) effect measurement. Reprinted with permission from Ref. [228].

7.3 Solar cell devices

Perovskite absorbers have no response in IR region and incorporation of bismuth selenide can enhance the performance of perovskite solar cell devices in this part. High charge mobility and tuneable p-type/n-type behaviour are also considered as beneficial for bismuth selenide material for charge selective layer implementation. In solar cell industry and based on the device structure (*i.e.* three terminal tandem, a flexible transparent, or a stand-alone commercial one) we need to use and design new materials to have the best efficiency, cost, toxicity level, weight, etc. Here, bismuth selenide and the counterpart bismuth telluride/sulphide have been tested in different solar cell devices both as (co-)absorber or charge transfer layer. They implemented in order to increase the charge mobility and reduce trapping/recombination draw back effects or optimise the light absorption capability in IR region. Supekar et al. have collected the recent efforts for the implementation of bismuth sulphide and antimony sulphide counterparts in solar cell devices in Ref. [230]

Bismuth selenide (band gap 0.3 eV) has not the best band gap for the solar light absorption in solar cells, therefore is not fundamentally interesting as a key component main layer in solar cell materials; However it has been implemented as an additive in dye sensitized solar cells anode or cathode electrodes [231,232] and perovskite solar cells [233] charge transport layers. Other bismuth chalcogenide such as bismuth telluride and sulphide have also been implemented as electron and hole transport layers in high stability, high efficiency normal and inverted perovskite solar cells improving the ambient stability of the device as reported in Ref. [234,235]; And even as hole transporter in organic solar cells [236]. As an additive, it can enhance the charge transport, carrier lifetime, collection efficiency, infrared absorption, enhancement of overall power conversion efficiencies and improvement of electrocatalytic activity in counter electrode. It has been even been theoretically explored as well [233]. The similar compound bismuth sulphide however fulfils the bandgap criteria for being a good solar absorber and have been implemented both as solar absorber layer and transport layer for perovskite solar cell devices so far [235,237,238]. Very recently, a similar tin chalcogenides has been used as electron transport layer for enhancement of stability in tin based perovskite solar cells [190]. The special surface related properties of bismuth selenide have

View Article Online
DOI: 10.1039/D5MA00876J

been considered for novel charge transport layers in perovskite solar cells. For example the charge transfer kinetics at interface of lead perovskite absorber material with Bi_2Se_3 have studied via laser spectroscopy in Ref. [178].

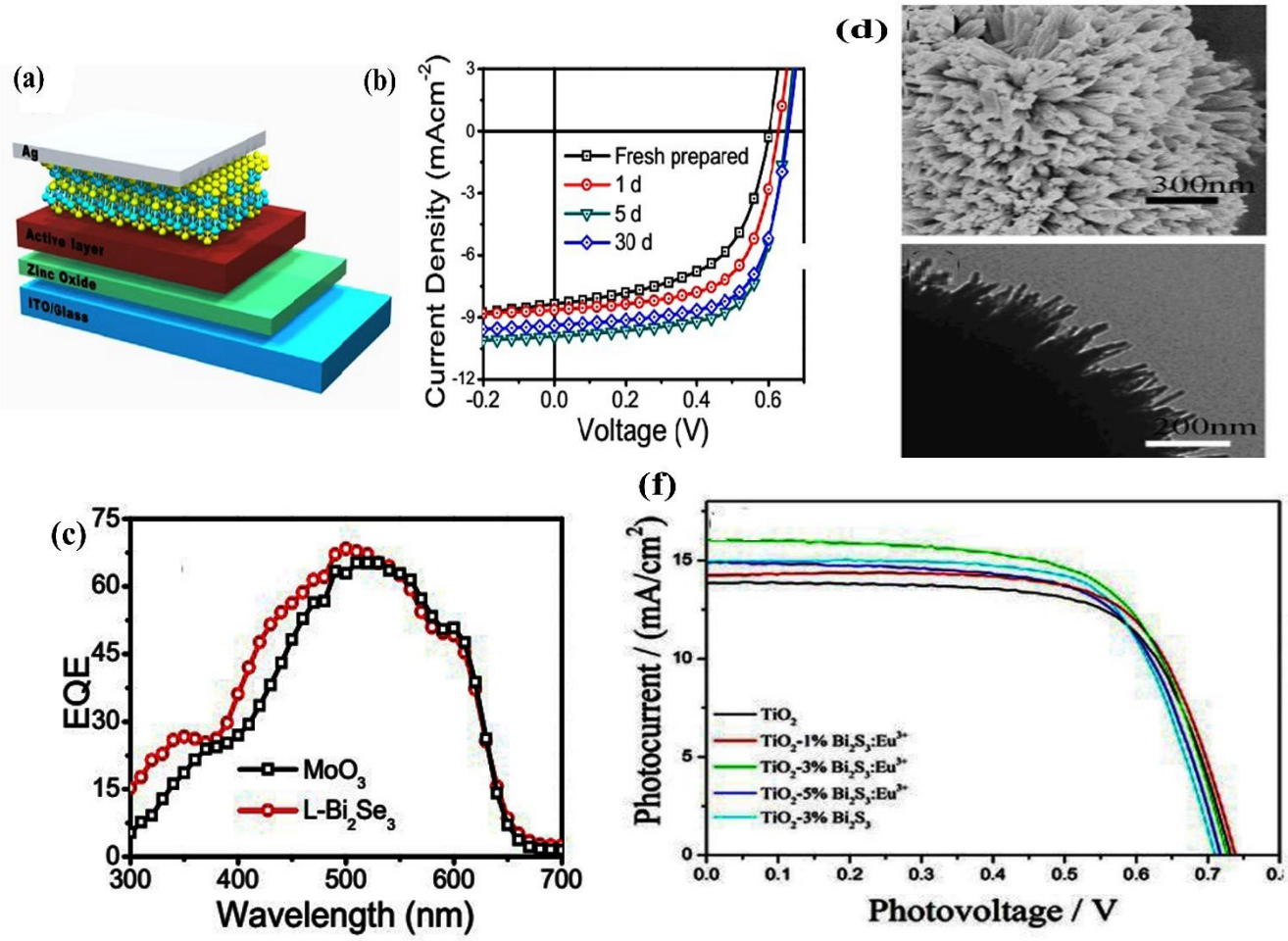

Fig. 21 (a) Schematic of the organic cell device with Bi_2S_3 counter electrode and (b,c) power conversion efficiency of the device after aging and comparison of incident photon to current efficiency (IPCE) with typical MO counter electrode. Reprinted by permission from ref [231,236] (d,e) SEM and TEM images of bismuth selenide nanostructures used as an additive in dye sensitized solar cell and (f) the PCE improvement with bismuth sulfide additive. Reprinted by permission from ref [231,236].

7.4. Charge storage devices

Bismuth selenide materials have been implemented as electrode material for ion batteries and supercapacitors. There is more room for bismuth selenide nanostructures for charge storage devices research, and even its composites with carbon have shown very good results. Layered stacked structure of the bismuth selenide and high surface to volume ratio of its nanostructures provide a high ion diffusivity and charge transfer in electrode. Moreover, they usually show a high stability in batteries. Zhao et al. in a recent work [165] proposed a few-layer bismuth selenide cathode as cathode material in quasi solid Zn ion batteries with anti-freeze hydrogel electrolyte and characterized the

View Article Online
DOI: 10.1039/D5MA00876J

battery at low temperature of -20 Celsius. The delivered capacity was 1.5 times higher than room temperature with the same specific current. A high stability of about 95% retention after 2000 cycles at 1 A/g obtained as well. They have showed that zinc ion uptake at few-layer bismuth selenide is higher in lower temperatures *i.e.* about 6 Zn^{2+} ions uptake at -20 ^{O}C and four ions uptake at 25 ^{O}C. This unusual behaviour happens just for few-layer bismuth selenide and not for its bulk counterpart and can relate this to topologically protected surface states and weaker phonon vibrations at low temperatures. Therefore, this bismuth selenide-based electrode can be a choice for charge storage and powering of devices operating in low temperatures for long term. **Figure 22** shows the electrochemical characterization of the battery, cycle retention and corresponding bismuth selenide volume changes after intercalation of zinc ions.

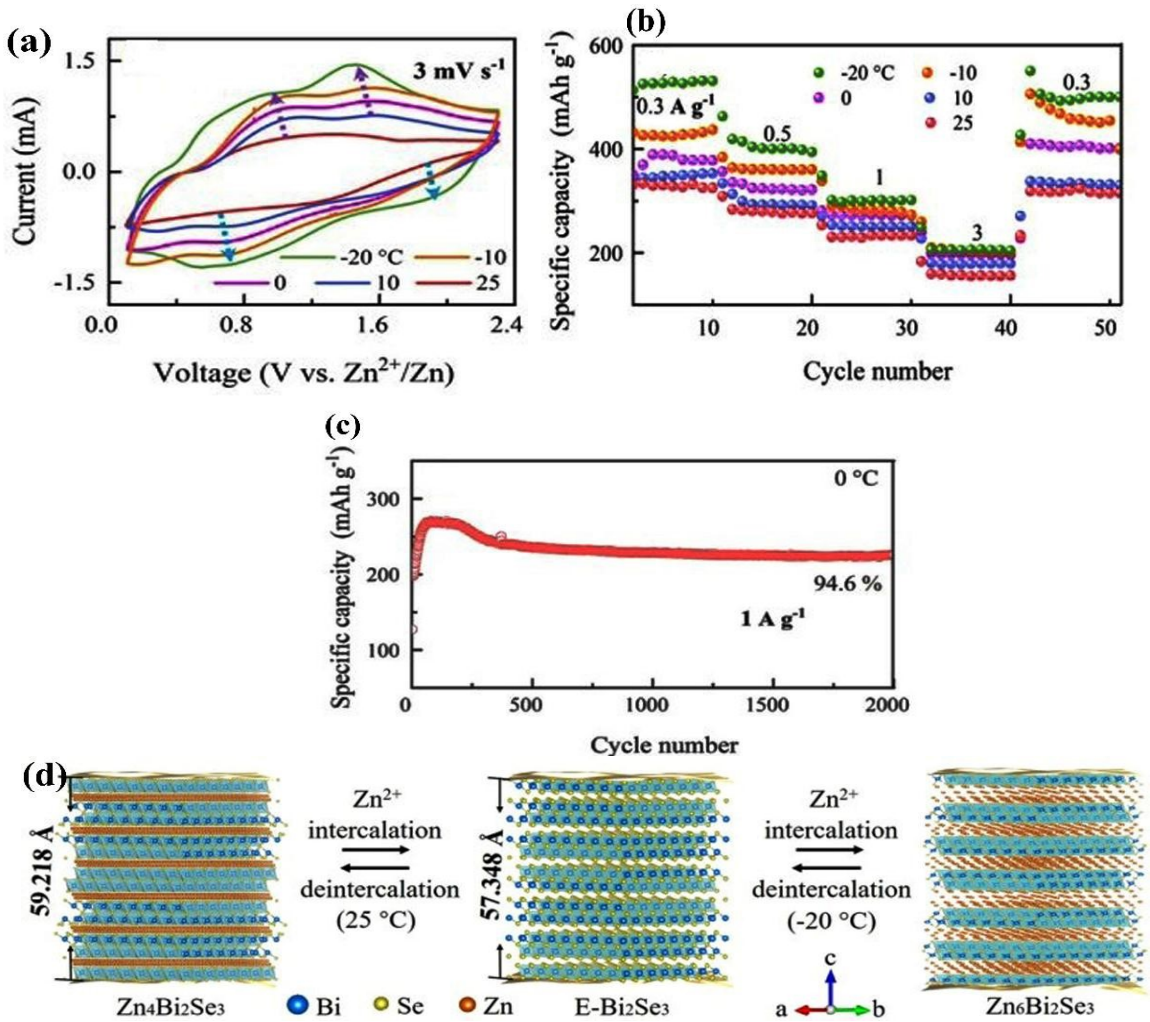

Fig. 22 Zn ion battery based on bismuth selenide cathode (a-c) cyclic voltammetry, specific capacity at different temperatures and cycle retention after 2000 cycles at zero Celsius. (d) corresponding temperature dependent unit cell volume changes after the intercalation of zinc ions at cathode. Reprinted with permission from ref [163,165].

Xingxing Zhao et al. [239] have used bismuth selenide with a carbon coating Bi_2Se_3@C in the cathode of potassium ion batteries which involves alloying redox reaction. It shows a very high reversible capacity of 526 mAh/g at 50 mA/g specific current and very high stability after 1000 cycles of charge-discharge. A micro supercapacitor was made by Hao et al. [46] with a high specific capacitance of 272.9 F/g. The

View Article Online
DOI: 10.1039/D5MA00876J

high electrochemical active surface of bismuth selenide for reversible redox reactions due to its layered quintuple layer structure mentioned as the support of this good result. A large capacitance, high power density and 95.5% retention after 1000 cycles obtained for a flexible all solid-state capacitor made of Bi_2Se_3.

Meja et al., characterized the bismuth-selenide-based anode electrodes for aqueous sodium ion batteries via electrochemical techniques. They have found two order of magnitude improved related diffusion coefficients in comparison to other similar anodes for sodium ion batteries. However the stability is still an issue which needs to be considered for practical applications[169]. A schematic of the cell and the results are shown in **Fig. 23**.

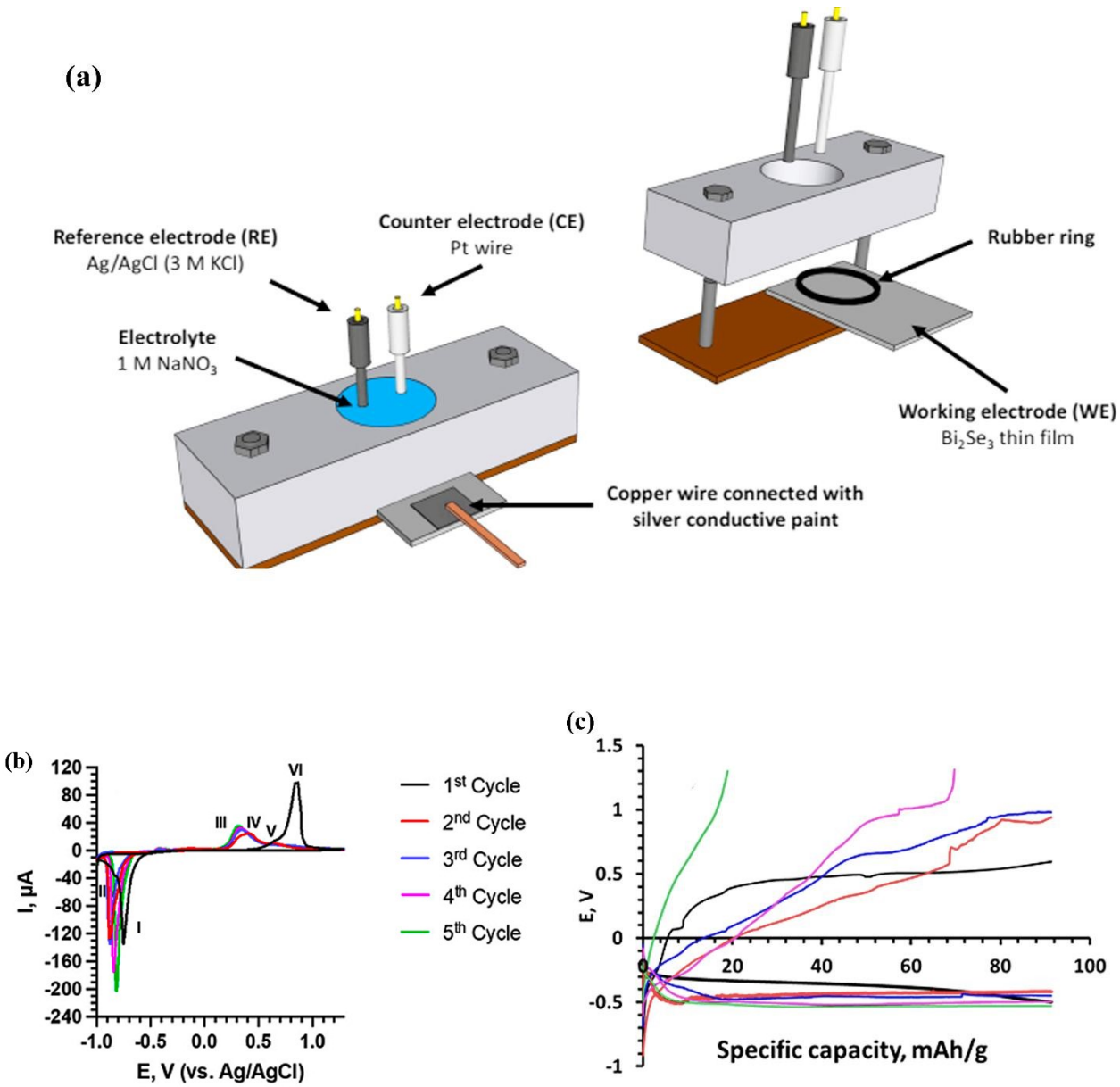

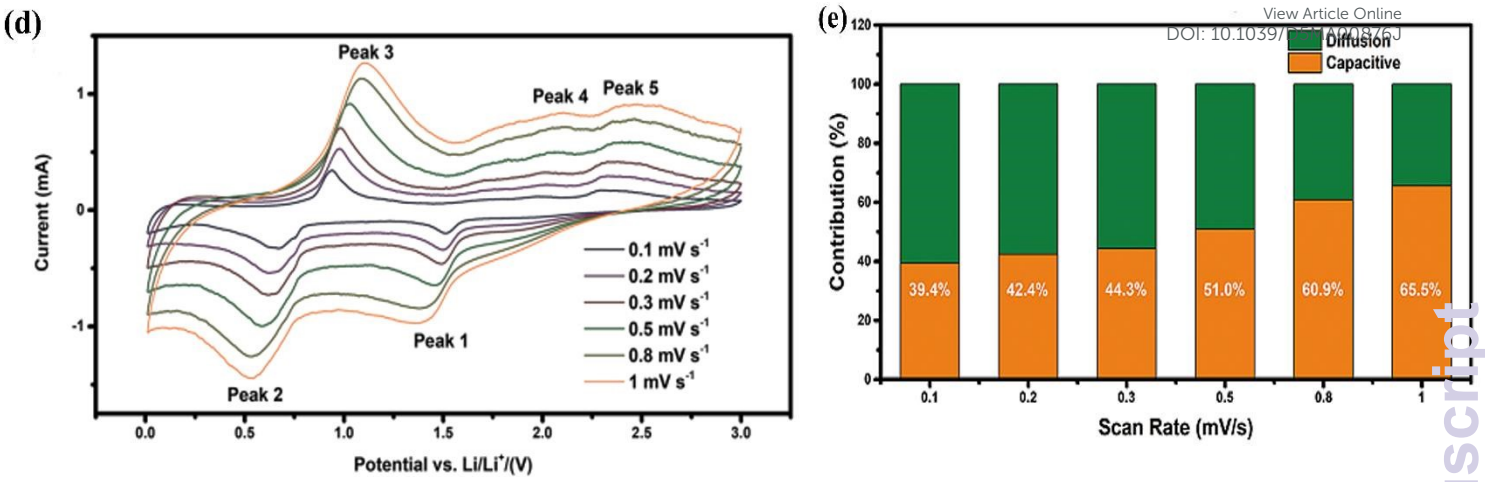

Fig. 23 (a) Schematic of the electrochemical cell. (b,c) cyclic voltammetry and charge/de-charge curves for bismuth selenide electrode in lithium ion battery from ref[169]. Differences in CV graph are corresponding to different reaction or charging/de-charging phenomena at electrode interface. Reprinted with permission from Ref [169] d and (e) cyclic voltametric graphs of bismuth selenide @C electrode for lithium ion battery in different scan rates and the corresponding diffusive and capacitive contributions in total capacitance measured at different scan rates. Reprinted with permission from Ref [240].

Kumari et al., have employed bulk and nanostructured bismuth selenide in all solid-state lithium-ion batteries as anode and achieved acceptable performance. Thermochemical reaction between the solid electrolyte and selenium produced at de-lithiation process results in loss of cycle stability. However, they showed that the nanostructured film based on nanoparticles and nanosheets enhances the stability compared to the bulk counterpart with excellent discharge capacity [241]. Basically, two different contributions from capacitive and diffusive charging can happen at electrode with different reaction features at cyclic voltammogram (**Fig. 23 c-d**) [169]. Several studies have been pursued to investigate ,implement and engineer the sole bismuth selenide based or its composite based ion batteries regarding the stability improvement, performance enhancement or studying the physical chemistry of the reactions at interfaces[240,242–244]. Theoretically bismuth selenide has a high specific capacity for alkali-ion storage due to its layered structure with large interlayer spacing.

After the achievement of successful results for bismuth selenide based potential lithium-ion batteries, more studies on zinc, magnesium, potassium, and sodium ion batteries have been also conducted. These accomplished with varieties of implemented materials such as bulk, nanostructured, doped, nanocomposite and metal organic frames all based on bismuth selenide. Here the drawback can be the stability issue *i.e.* poly-selenide shuttle formation, pulverization [245] and excess volume expansion of the layered bismuth selenide electrode after the ion intercalation; which affects the stability. Bismuth selenide nanostructures instead provide more surface sites and more space for the bulk expansion. Zhu et al. modified the bismuth selenide electrodes with nitrogen-doped $Bi_2Se_{3-x}Te_x$ nano materials, which show a stable discharge capacity of 464 mAh/g after 60 cycles at a charge density of 0.1 A/g. Its unique structure helps the volume expansion issue and stability of the cell [246] . In a recent work , Zou et al. implemented the Sb doped bismuth selenide decorated and encapsulated with nitrogen-doped carbon as anode material for lithium ion batteries [245]. They have shown that

electrochemical performance improved and the shuttling of poly-selenide suppressed after doping/encapsulating of bismuth selenide.

Ni et al., in a separate report, have discussed and compared the challenges and recent efforts for the implementation of bismuth chalcogenide electrodes in electrochemical devices such as ion batteries and supercapacitors. The key technical issues for material development for novel, more stable, and high-performance devices have been highlighted.[247] One key feature is the layered structure of bismuth telluride and selenide with van der Waals interlayer interactions, leading to possible less stable electrodes in cell cycling; however makes more room for a higher ion uptake. The bismuth sulphide and oxide possess, however, a different crystal structure and show a higher stability. Engineering of band edges based on the chemical bonding concepts is a facile route for having different electrochemically active windows in electrochemical applications.

7.5. Biosensors and Gas Sensors

Due to its high electrocatalytic activity, high surface-to-volume ratio of its nanostructures, high charge carrier density, and the presence of plasma resonance, bismuth selenide has been widely used as a material for urea, glucose, ammonia, and atenolol biosensors. Together with its imaging, cancer therapy, antimicrobial, and even drug delivery properties, bismuth selenide shows great potential for application as a future medical agent. Fudan Zhu et al. considered a multiwall carbon modified bismuth selenide as an electrochemical biosensor with promising performance for nitrile detection (up to 0.01 μM) [248]. Higher electron transfer rate and active surface area were mentioned as reasons for the high detectivity of this biosensor for the detection of nitrile in food and the environment. Savariraj et al. made a biosensor from a few-layer bismuth selenide material made via microwave-assisted synthesis [249]. Resonant plasma frequency and high electrocatalytic activity of Bi_2Se_3 mentioned as promising for the high level of glucose detection (up to 6 μM). This sensor reaches the steady state with 3 seconds after glucose introduction and keep steady state for up to 19 days.

Lingping Xiao et al. demonstrated the Au nanoparticles decorated bismuth selenide electrochemical colorimetric biosensor [250]. Here, the solution colour change showed the 'Switch-on' and 'Switch-off' of the biosensor. The cancer biomarker is the CEA, and the presence of antibody-CEA or antigen-CEA can turn on or -off the catalytic activity of the bismuth selenide electrode. **Fig. 24** shows the schematic of the sensing mechanism together with the TEM images of the gold decorated bismuth selenide sheets and the catalytic activity of the structure for the reduction of 4-nitrophenol in the presence of different concentrations of anti-CEA.

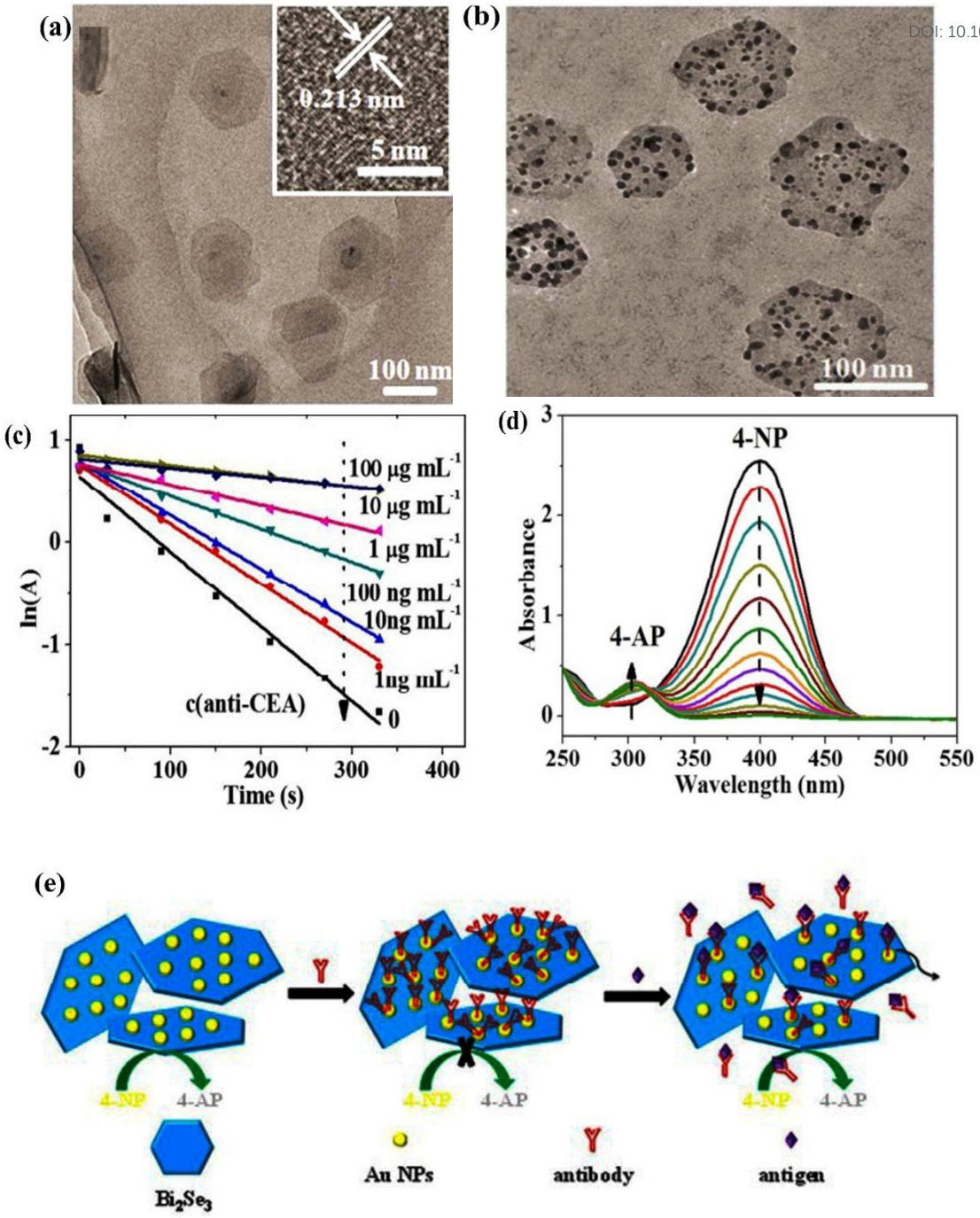

Fig. 24 (a,b) TEM images of the gold-decorated bismuth selenide sheets implemented in the calorimetric biosensor. (c,d) shows the catalytic activity of the bismuth selenide structure and the corresponding absorbance change for the reduction of 4-nitrophenol in the presence of different concentrations of anti-CEA. (e) schematic of the sensing mechanism in the presence of antibody-CEA and antigen-CEA. Reprinted with permission from Ref. [250].

View Article Online
DOI: 10.1039/D5MA00876J

This shows a very high selectivity and sensitivity even for very low CEA concentrations of 160 picogram per millilitre together with confirmation via real clinic sampling, analysing results. The corresponding catalytic activity of this electrode was compared to other similar works in ref [250]. It shows that using a much lower amount of material, they have better or much better catalytic activity for the reduction of 4-nitrophenol.

Gas sensing properties of Bi_2Se_3 are investigated in Refs. [251,252] . Van der Waals layered structures usually don't have dangling bonds at the surface, and gas sensing capabilities are limited. However, through *i.e,* creating two-dimensional nanoscale and edge features[251] or making epitaxial growth, one can reach the desired electronic properties. For NO_2 gas sensing, a high response of 93% at 50 ppm has been reached via a bismuth selenide nanosheet layer in a chemi-resistive gas sensor with anti-humidity capability [252] (**Fig. 25**).

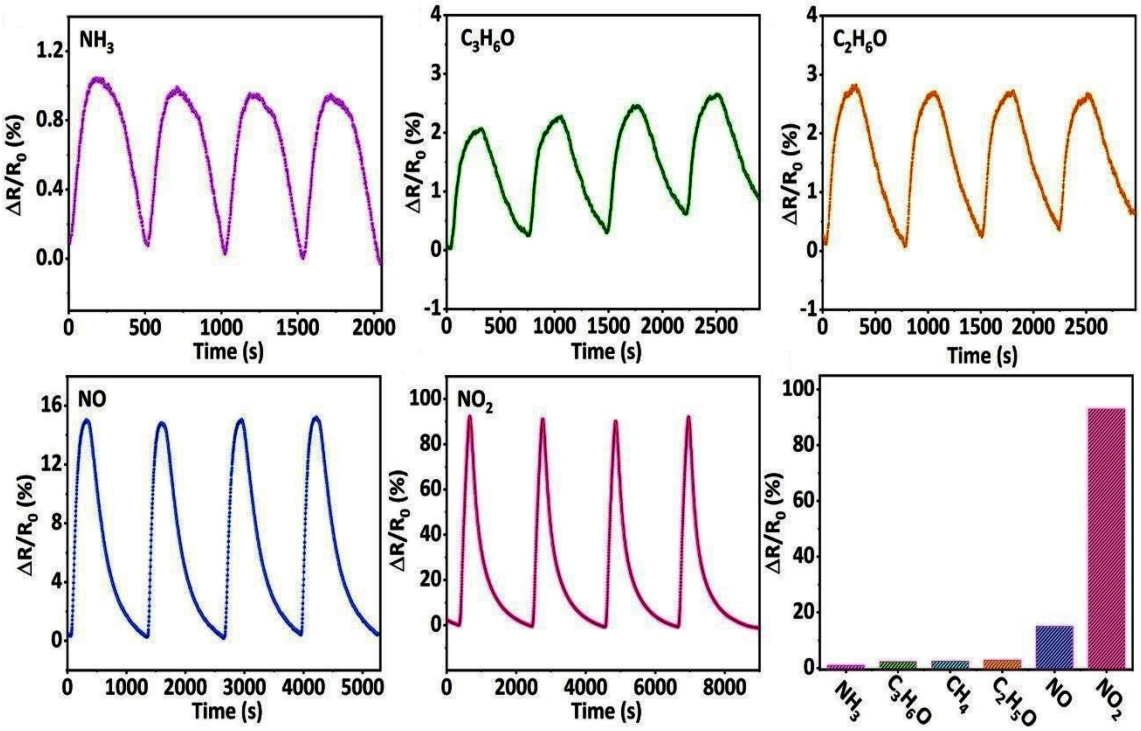

Fig. 25 resistance variation of chemi-resistive gas sensor based on bismuth selenide under exposure of different gases. Reprinted with permission from ref [252].

In a separate study, Yi et al. measured the NO_2 sensing properties and its underlying mechanism for bismuth selenide/tin selenide hexagonal sheets heterostructure. It shows a rather fast detection of 15 seconds at room temperature and detection limit of 25 pbm [253]. The gas sensor also showed a good selectivity for NO_2 in between the tested gases such as H_2S, NH_3, CH_4, CO and SO_2.

7.6. Antimicrobial effects and medical applications

The bismuth selenide surfaces are prone to be effective antimicrobial surfaces as reported previously *i.e.* by Jiang et al. [254]. 80 nm bismuth selenide sheets together with hydrogen peroxide presented as new type of insecticide and biocompatible surface wherein in-vitro and in-vivo studies show that growth of Escherichia coli and Staphylococcus bacteria significantly suppressed (**Fig. 26**).

View Article Online
DOI: 10.1039/D5MA00876J

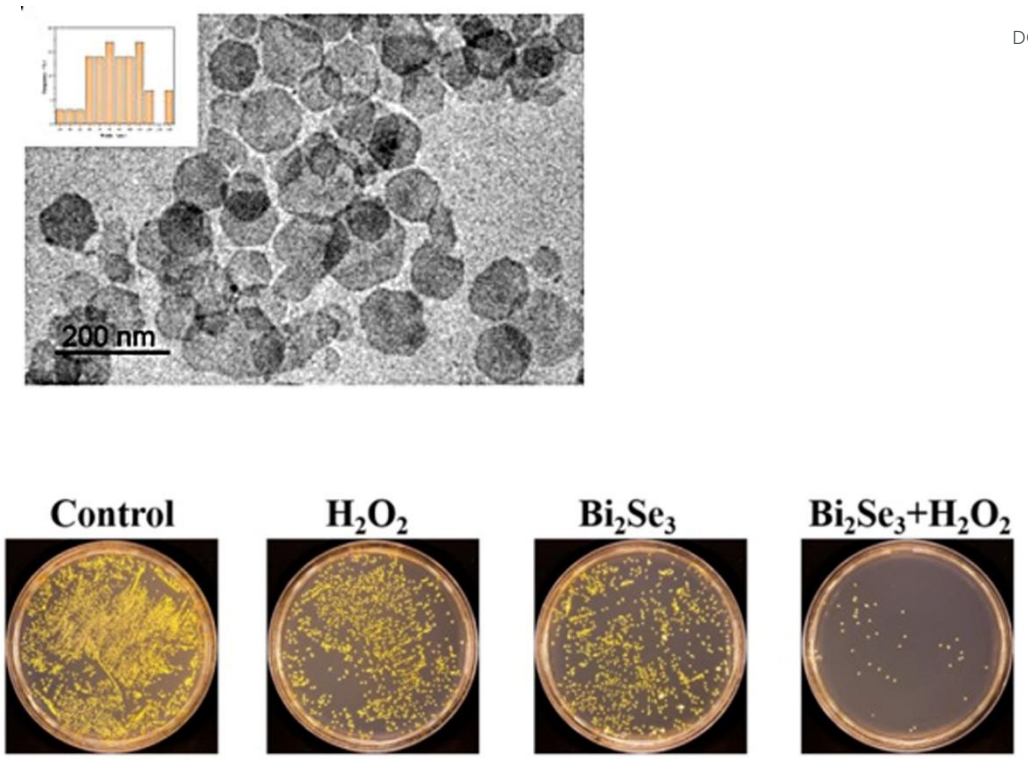

Fig. 26 TEM image of implemented bismuth selenide nanosheets and optical images of bacteria growth on control and antimicrobial surfaces. Reprinted with permission from ref [254].

Recently, nanomedicine and bioengineering have made it possible to have diagnosis and therapy simultaneously. This safely enhances the cancer immunotherapy and tumour imaging [255]. The main benefits and characteristics are non-toxicity and biocompatibility, the ability to convert biofriendly infrared light into heat and subsequent active electron hole charges for chemical and biochemical reactions, high X-ray attenuation coefficient of bismuth, the ability of selenide in reducing the cancer mortality, and its rather controllable shape and size in the nano-size regime. Therefore, bismuth selenide has been considered widely for different medical applications such as imaging, delivery, antimicrobial, cancer therapy, and photothermal therapy applications.

In imaging-guided photothermal therapy, one can simultaneously monitor and eradicate the tumours selectively in specific, limited space and with remote-controllable means. Li et al. via a multifunctional sponge like nano-spheres (presented in **Fig. 27**a) have done real-time imaging tests for in-vivo X-ray computing tomography (CT) and infrared thermal imaging of tumours with high contras. They also performed photothermal therapy tumour killing with high stability and high biocompatibility and importantly no toxicity. They also show that these structures possess a very high capacity of drug loading and release in drug delivery as well as being an anti-tumour agent with growth inhibition ration of 94% outperforming other methodologies [256]. Here, the nanostructured sub-micron sized morphology assists the light trapping and scattering, prepare more volume for drug loading and showing more stability and biocompatibility compared to nanoparticles and other nano-sized structures. The presence of bismuth selenide inside the mouse tumour together with near IR laser (808 nm) shows the antitumor cancer therapy ability wherein the initial tumour spots are ablated and absent after the treatment (**Fig. 27**f). This innovative platform shows promise for safe and effective antitumor therapy and encourages further research into drug loading on Bi_2Se_3 and other

photothermal agents for enhanced biomedical applications. Multifunctional therapic impacts of these nanostructures are summarized in **Fig. 27**.

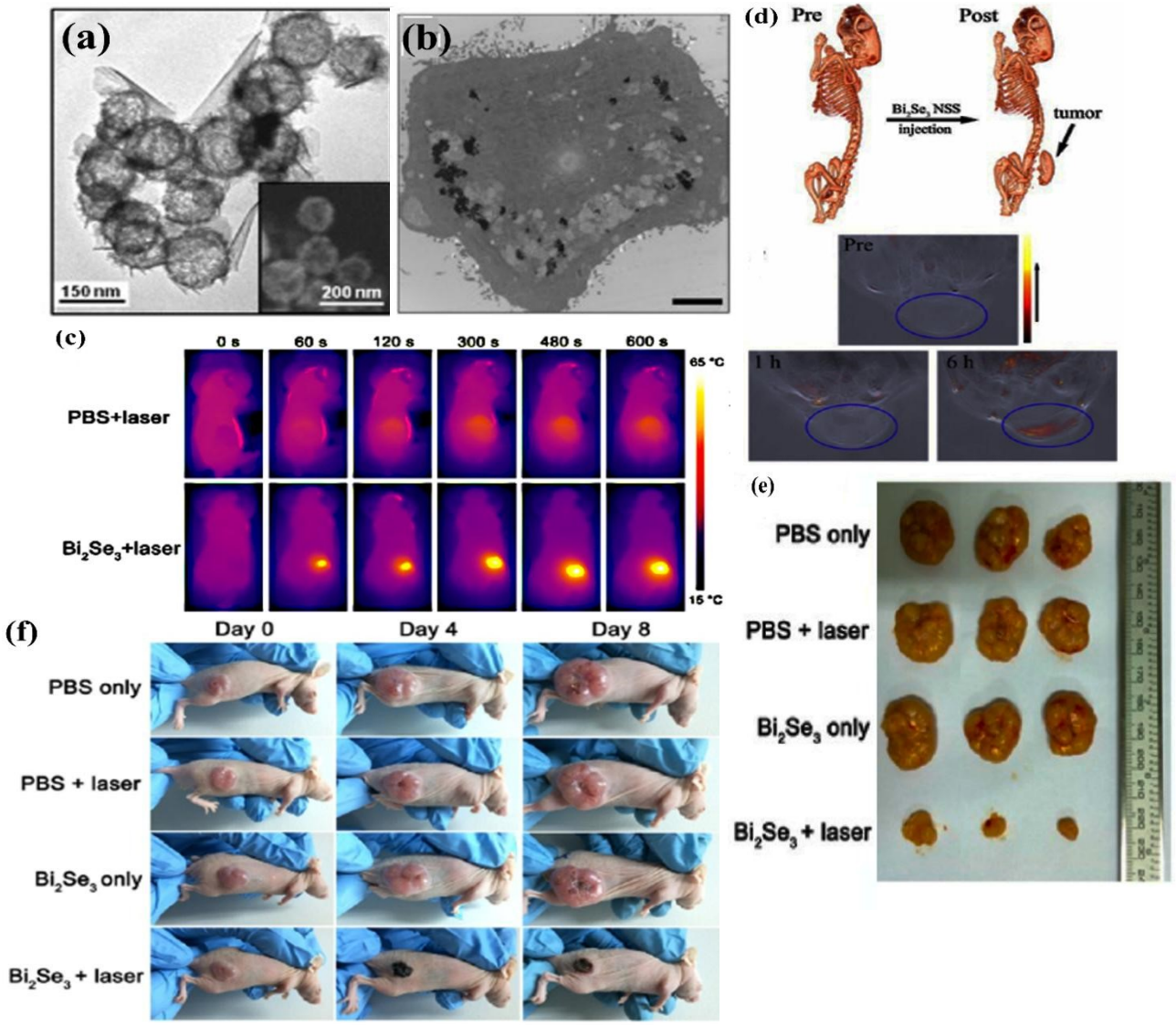

Fig. 27 (a) TEM image of the bismuth selenide sponge-like spheres (b) TEM image showing the penetration of the bismuth selenide structures in the intracellular medium. c) Infrared thermal images showing local accumulation of bismuth selenide at tumour location and ablating it (d) CT image and multispectral optoacoustic tomography (MSOT) image of mouse tumour before and after (one and six hours later) bismuth selenide injection. (e) representative optical images of the tumour after 12 days of treatment. (f)Optical images of antitumor and cancer therapic ability of bismuth selenide in in vivo study inside a mouse body, reprinted with permission from [256].

Yilin Song et al. have implemented hyaluronic acid-doped poly-pyrrole-coated bismuth selenide hexagonal sheets loaded with zinc phthalocyanine nano-dish complex for antitumor applications. This complex showed a tumour growth inhibition ratio of more than 96% with an excellent therapeutic effect. CD47 tagged bismuth selenide particles at the same way implemented for photothermal therapy by increasing macrophage phagocytosis of cancer cells studied by Guo et al. [257]. Jingke Yao et al. reported about the chemically grown bismuth selenide nanostructures as an alternative, easy to

View Article Online
DOI: 10.1039/D5MA00876J

prepare, and unexpensive alternative for gold nanoparticles in highly efficient optical coherence tomography [258]. In the work done by Mao et al. [259] biocompatible nanosized particles of bismuth selenide were successfully applied in multi-modal imaging guided radio-thermal therapy against cancer. Simultaneous capability of bismuth selenide as cancer imaging and therapic agent was shown by Juan Li et al.[260]. The presence of bismuth selenide particles injected in the mouse body can be a contrast agent for CT imaging of tumour in the body and under illumination with near infrared laser. They simultaneously burned out the tumour from the mouse body as shown in **Fig. 28-29**.

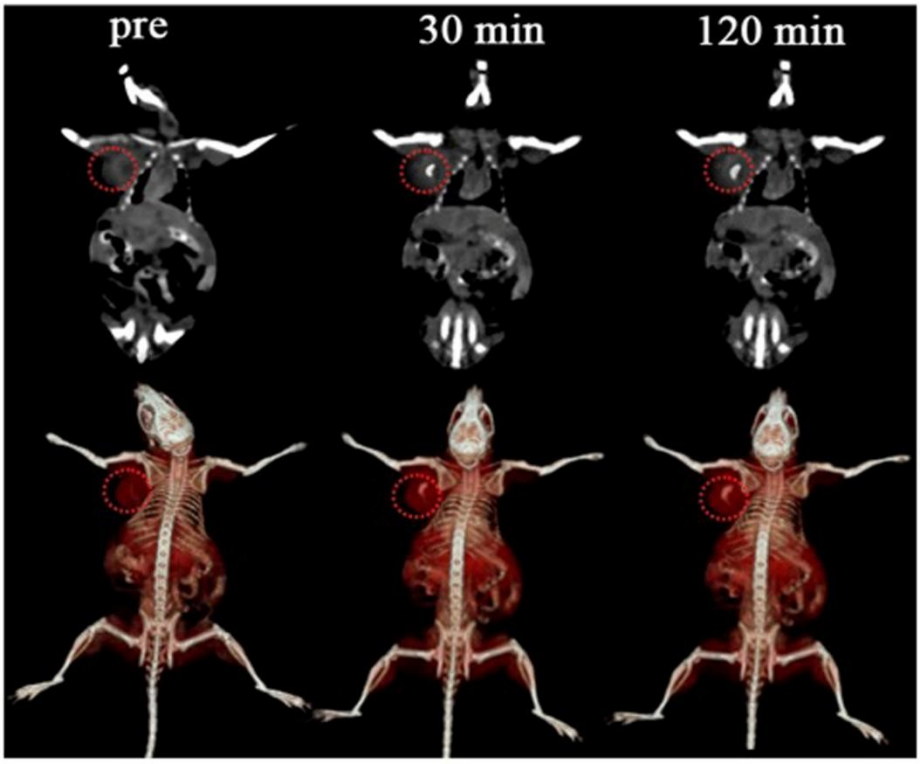

Fig. 28 X-ray-computed tomography (CT) coronal views of the mouse body before injection (pre) and after injection of bismuth selenide particles after 30 and 120 minutes. The red circle shows the location of tumour. The particles collected selectively at tumour location and acted as contrast agent. Reprinted with permission from [260].

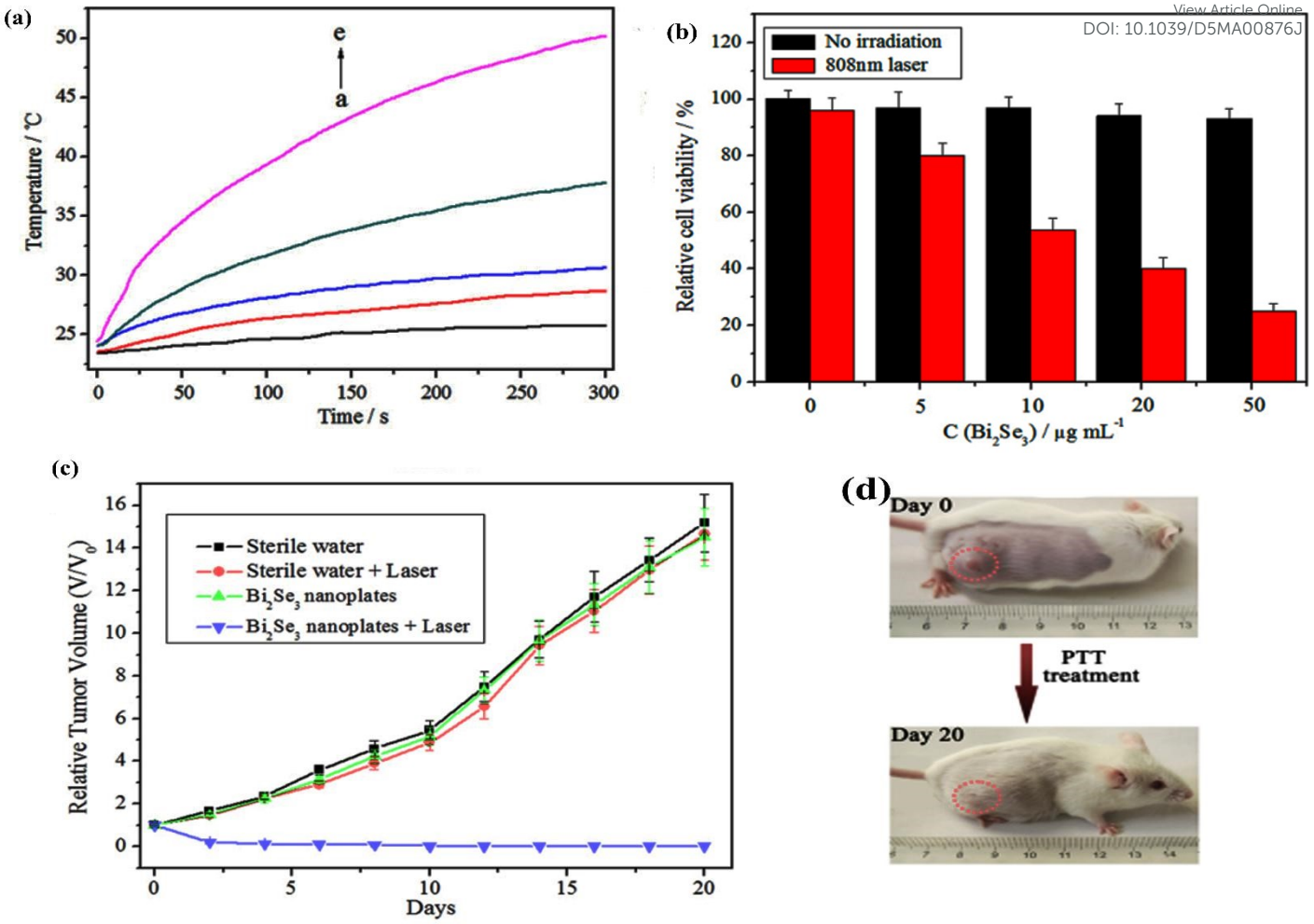

Fig. 29 (a) Temperature of the tumour in photothermal therapy at different concentrations of injected bismuth selenide particles in water (a-e) 0,5,10,20,50 microgram per millilitre). (b) Cell viability of cancer cells with/without bismuth selenide in dark and light (808 nm infrared laser irradiation). (c) relative tumour volume after the therapy and (d) corresponding optical images showing that the tumour is burned out. Reprinted with permission from [260].

Moreover, bismuth selenide /manganese oxide nanocomposite templated via bovine serum albumin has shown a great capability as radiotherapy sensitizer with enhanced radio sensitivity with satisfactory stable tumour targeting as well as magnetic resonance imaging (MRI) and CT-scan [261].

Hao Zhou et employed novel biosynthesis of Bi_2Se_3 via Selenite-reducing bacteria wherein the pre-incubated bacteria were added to the precursor solution of bismuth and selenide and bacteria enzymes helped to reduce the Se anions and initiate the growth [140]. The resulting bismuth selenide structures formed inside the bacteria and at extracellular medium and collected via centrifugation. These structures showed no toxicity to human breast cells and together with near Infrared 808 nm laser illumination in Photothermal Therapy (PTT) ablate the breast cancer cells effectively. The corresponding TEM images and formation mechanism together with cancer cell viability in the presence of bismuth selenide-Z (here Z means bacterial-attached) and laser illumination are presented in **Fig. 30**.

View Article Online
DOI: 10.1039/D5MA00876J

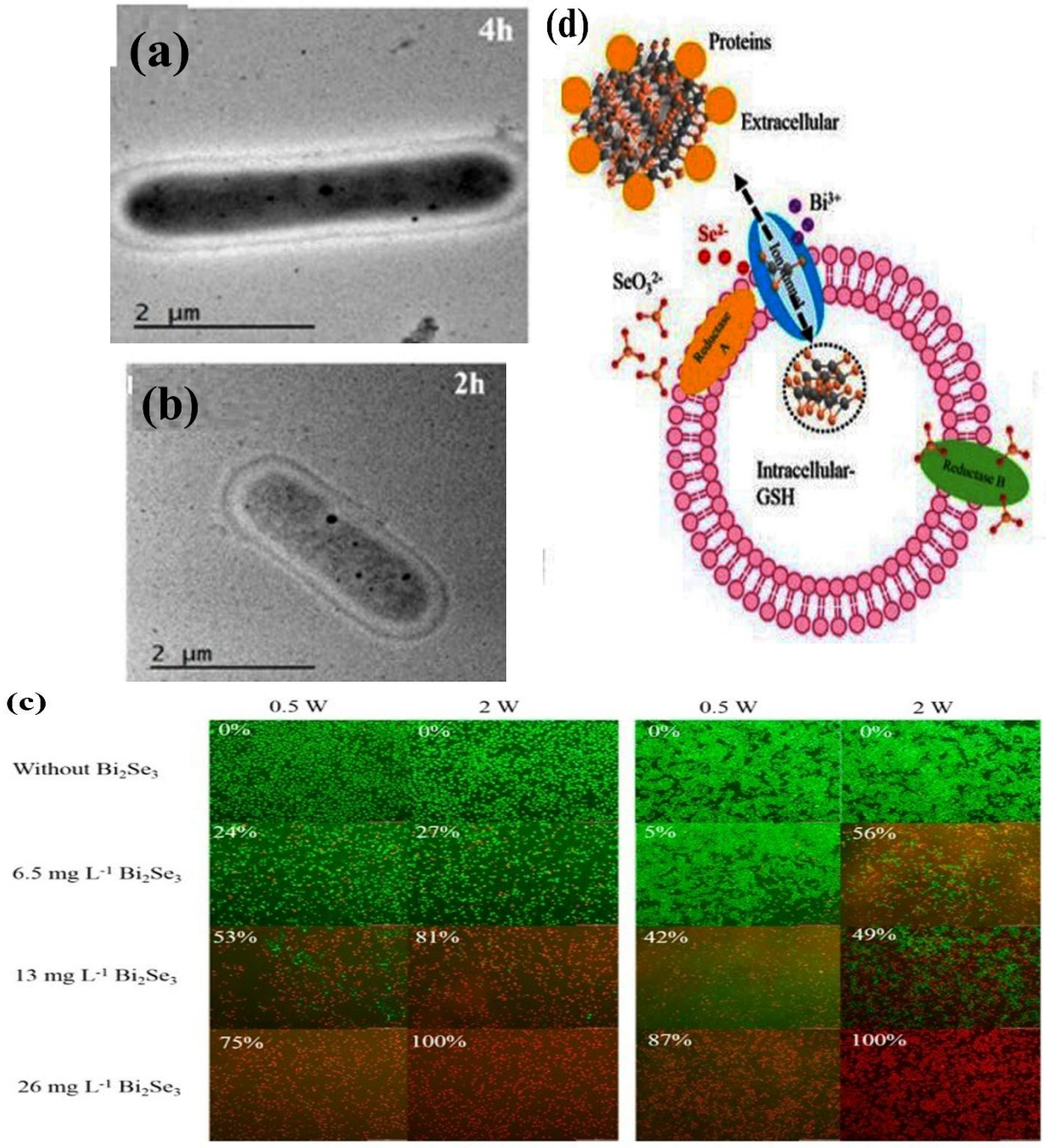

Fig. 30 (a,b) TEM images show the bismuth selenide-Z nanostructures inside the cell. (c) the schematic for the formation of structures in intracellular and extracellular medium, and (d) cell viability of breast cancer cells in the presence of Bi_2Se_3-Z structures under infrared laser illumination. The red spots show the dead cells. Reprinted with permission from ref [140].

In a separate study, Hongjuan Zhao et al. implemented a specific morphology of macrophage membrane camouflaged hollow bismuth selenide nanoparticles in order to enhance the imaging and therapic efficiencies compared to normal bismuth selenide nanoparticle structures. They showed possessing prolonged blood circulation life, accelerated and enhanced tumoritropic accumulation and great promise for suppressing the breast cancer [262].

View Article Online
DOI: 10.1039/D5MA00876J

Similar bismuth chalcogenides have been implemented in antibacterial, cancer therapy, and biosensing devices. This class of materials represents potential capacities for medical research as reported in Ref. [263] Generally, oxide and sulphide compounds have a more active surface for bio-functionalization compared to bismuth selenide, and comparative studies among these compounds can be insightful for developing and engineering new materials with novel properties based on chemical bonding effects (See sections 2 and 4).

8. Concluding Remarks and Future Prospects

Topological insulator bismuth selenide has shown great promise in nanostructure-based new generation green energy device applications. Specific physical properties and many intriguing potential capabilities coming from the crystal and atomic structure and topologically protected surface states make all these possible. Proper characterization and engineering of these properties via fine growth modifications are necessary for the advancement of the research area for future practical issues. Although they have been initially used as thermoelectric devices and transistors, they have more applications than the above-mentioned i.e. in anti-wear/anti friction [264], water splitting [265], nanoelectromechanical switching[266], piezoelectric applications [267], metal-oxide-semiconductor-field-effect-transistors(MOSFET), thermopower conversion of waste heat to electricity, etc.

An overview of recent state-of-the-art photodetector devices based on bismuth selenide is briefly summarized, and response times in the order of a few microseconds and detectivities up to 10^{13} Jones have been achieved. The optical spectrum is sensitive from the mid-infrared range and above, and topological insulators have shown their own capabilities[209]. Further future developments include speeding up the responses and enhancing sensitivities, large-scale stability improvement. Here, new mechanisms such as photothermal sensing, the local heating effects, and phase transitions at low temperatures for polarization detection still need to be further explored. Material engineering, defect engineering, and hybrid devices made from combinations of various materials, for example, graphene-based hybridization with topological insulators, offer the potential to construct novel devices and the development of on-chip multi-functional optoelectronic technologies and cyber security.

In medical imaging and therapic applications, the successful performance of bismuth selenide with acceptable stability is proven; however, studies are showing that in long-term circulations of its small nanoparticles inside the body (*i.e.,* lungs), they can elevate the level of reactive oxygen species (ROS), causing cell death [268]. Therefore, special encapsulating may be needed for real in vivo experiments. Other studies show super bio compatibility and non-toxicity, however. It seems more conclusive research needs to be done for this. Nanostructured sub-micron hollow spheres on the other hand provide a more biocompatible solution compared to very small nanoparticles.

In a very recent study, the relation between the Bi_2Se_3 nanoparticle size and the cytotoxicity indicates that biocompatibility can behave differently for different particle sizes[269]. Therefore, the new modified growth procedures with sole control on the nanostructure size and morphology, as well as the higher scalability and particle yield, can be desirable for phototherapy and bio-imaging treatments within the body. The ongoing research for treating diseases via phototherapy still needs standardized protocols, and there is a big room for further development of clinical research based on bismuth selenide materials.

View Article Online
DOI: 10.1039/D5MA00876J

Many interesting growth methodologies with excellent morphological control have been developed, and together with doping, Fermi level alignment, and structural modifications, lead to superior design and fabrication of novel nanostructure-based devices.

Here, for large-area multi-pixel detectors, it is important to deal with mm- or cm-sized films and corresponding single crystals. Promising growth routes need to be implemented for the future, including polycrystalline wafers or large-scale single crystals and several hundred micro-thick films. Hybrid structures with multi-layered two-dimensional materials can enhance and tune the photophysical properties and suppress the dark current for achieving higher-performance detectors. Triggered by this, experimental verifications based on a hybrid structure approach are still at the level of research and development (R&D) stage, and later large-scale scaling and commercialization are on the way, for example, for X-ray photodetectors.

The wide range of bismuth selenide technological applications makes it feasible to have future multifunctional self-powered devices for novel medical treatments, wherein the biocompatible device with embedded charge storage capability can implicitly do the bio-sensing, tumor imaging, and cancer cell therapy within the human body. In order to achieve self-powered operations, additional possibilities are engineered, built-in electric fields at interfaces, making use of ion migration and ferroelectric domains, which can be further inspected for bismuth selenide-based devices.

For thermoelectric applications, mechanical stability, however, can be improved in the layered structures via alloying, introducing secondary phases, tuning the grain integrity, and making new composites, which may introduce new complexities. Applications such as high precision flexible dual mode thermocouple sensors [270] and conversion of waste water heat to electricity in the industrial sector are desirable. On the other hand, further exploiting the topological surface states for high-performance thermoelectric devices is required. The macroscopic features are so far well characterized; however, the recent attempts and methodologies to probe the local microscopic features with a high spatial resolution remain unexplored and need to be further developed[271]

In the theoretical research part, the main interest is fundamental physics of topological insulator surface states and the application in Majorana fermions and spintronic devices. Recent efforts have been devoted to spin dynamics, spin-polarized Dirac states [272], superconducting transitions, electronic structure at interfaces and topology, Majorana states, spin current torques, and electron-phonon interactions with DFT as still the main methodology for electronic structure calculations.

While a joint theoretical/experimental approach for quantum information and future quantum computers is developing, the quantification of role-playing phenomena becomes more vital. The presence of excitons under photo-excitations and the impacts on quantum computing is an important issue, and it is still unclear whether the exciton topology is transferred to the photonic quantum state of Bi_2Se_3 or not.[273] Chemical bonding effects[30,31] and comparisons with telluride counterpart as well as other explored materials such as halide perovskite solar cell family, are very insightful. For more information and comparisons for the bismuth Telluride-Selenide system, we cite the reader to references [33,274].

The presented studies in this paper shed light on drawing a picture from the research status for topological insulator bismuth selenide as well as other chalcogenide counterparts, and paving route towards their further implementations in green energy devices.

View Article Online
DOI: 10.1039/D5MA00876J

Author contributions

The manuscript is written and revised with contribution from all the authors. MP, RK and HK prepared the initial draft. MP guided the work. MP, MM and GB have supervised the work and further revised the manuscript.

Data Availability

Data will be made available on request.

Conflict of interest

The authors declare no competing interest or personal relationships that could affect or influence this report.

Acknowledgment

MP thanks Iranian Elite foundation for the funding support of the current work.

References

1 F. K. Wang, S. J. Yang and T. Y. Zhai, *iScience*, 2021, **24**, 103291.
2 K. Mazumder and P. M. Shirage, *Journal of Alloys and Compounds*, 2021, **888**, 161492.
3 Y. Xia, D. Qian, D. Hsieh, L. Wray, A. Pal, H. Lin, A. Bansil, D. Grauer, Y. S. Hor, R. J. Cava and M. Z. Hasan, *Nature Phys*, 2009, **5**, 398–402.
4 D. A. Wright, *Nature*, 1958, **181**, 834–834.
5 L. B. Abdalla, L. Seixas, T. M. Schmidt, R. H. Miwa and A. Fazzio, *Phys. Rev. B*, 2013, **88**, 045312.
6 Y. Xiong, N.-C. Lai, Y.-C. Lu and D. Xu, *International Journal of Heat and Mass Transfer*, 2020, **159**, 120077.
7 A. M. Adam, E. Lilov, E. M. M. Ibrahim, P. Petkov, L. V. Panina and M. A. Darwish, *Journal of Materials Processing Technology*, 2019, **264**, 76–83.
8 G. R. Hyde, H. A. Beale, I. L. Spain and J. A. woolman, *Jornal of physics and chemistry of solids*, 1974, **19974**, 1719–1728.
9 J. G. Analytis, J.-H. Chu, Y. Chen, F. Corredor, R. D. McDonald, Z. X. Shen and I. R. Fisher, *Phys. Rev. B*, 2010, **81**, 205407.
10 J. HoRLK, .
11 P. S. Maiti, S. Ghosh, G. Leitus, L. Houben and M. Bar Sadan, *Chem. Mater.*, 2021, **33**, 7558–7565.
12 D. Hsieh, D. Qian, L. Wray, Y. Xia, Y. S. Hor, R. J. Cava and M. Z. Hasan, *Nature*, 2008, **452**, 970–974.
13 J. Horäk, L. Koudelka, J. Klikorka and L. Šiška, *Physica Status Solidi (b)*, 1982, **111**, 575–580.
14 R. Sk, M. M. Shirolkar, B. Dhara, S. Kulkarni and A. Deshpande, *Chemical Physics Letters*, 2015, **638**, 94–98.
15 X. F. Kou, W. J. Jiang, M. R. Lang, F. X. Xiu, L. He, Y. Wang, Y. Wang, X. X. Yu, A. V. Fedorov, P. Zhang and K. L. Wang, *Journal of Applied Physics*, 2012, **112**, 063912.
16 C. Ojeda-Aristizabal, M. S. Fuhrer, N. P. Butch, J. Paglione and I. Appelbaum, *Applied Physics Letters*, 2012, **101**, 023102.
17 G. Jnawali, S. Linser, I. A. Shojaei, S. Pournia, H. E. Jackson, L. M. Smith, R. F. Need and S. D. Wilson, *Nano Lett.*, 2018, **18**, 5875–5884.
18 Y. S. Hor, A. J. Williams, J. G. Checkelsky, P. Roushan, J. Seo, Q. Xu, H. W. Zandbergen, A. Yazdani, N. P. Ong and R. J. Cava, *Phys. Rev. Lett.*, 2010, **104**, 057001.

View Article Online
DOI: 10.1039/D5MA00876J

19 L. D. Alegria, M. D. Schroer, A. Chatterjee, G. R. Poirier, M. Pretko, S. K. Patel and J. R. Petta, *Nano Lett.*, 2012, **12**, 4711–4714.
20 J. E. Brom, L. Weiss, T. H. Choudhury and J. M. Redwing, *Journal of Crystal Growth*, 2016, **452**, 230–234.
21 K. Kadel, L. Kumari, W. Li, J. Y. Huang and P. P. Provencio, *Nanoscale Res Lett*, 2010, **6**, 57.
22 S. Nandi, S. Z. Cohen, D. Singh, M. Poplinger, P. Nanikashvili, D. Naveh and T. Lewi, *Nano Lett.*, 2023, **23**, 11501–11509.
23 G. A. Ermolaev, I. S. Vyslanko, A. P. Tselin, M. A. El-Sayed, M. K. Tatmyshevskiy, A. S. Slavich, D. I. Yakubovsky, M. S. Mironov, A. B. Mazitov, A. Eghbali, D. A. Panova, R. I. Romanov, A. M. Markeev, I. A. Kruglov, S. M. Novikov, A. A. Vyshnevyy, A. V. Arsenin and V. S. Volkov, *Nanomaterials*, 2023, **13**, 1460.
24 S. Das, B. Dandasena, D. Alagarasan and R. Naik, *ACS Appl. Opt. Mater.*, 2024, **2**, 642–654.
25 J. Deng and Z.-Y. Zhao, *Computational Materials Science*, 2018, **142**, 312–319.
26 H.-H. Kung, A. P. Goyal, D. L. Maslov, X. Wang, A. Lee, A. F. Kemper, S.-W. Cheong and G. Blumberg, *Proc. Natl. Acad. Sci. U.S.A.*, 2019, **116**, 4006–4011.
27 J. W. McIver, D. Hsieh, H. Steinberg, P. Jarillo-Herrero and N. Gedik, *Nature Nanotech*, 2012, **7**, 96–100.
28 T. S. Bhattacharya, S. Raha, P. K. Mondal, M. Pradhan, S. Ghosh and A. Singha, *Adv Funct Materials*, 2025, e10990.
29 J. R. Drabble and C. H. L. Goodman, *Journal of Physics and Chemistry of Solids*, 1958, **5**, 142–144.
30 M. S. Christian, S. R. Whittleton, A. Otero-de-la-Roza and E. R. Johnson, *Computational and Theoretical Chemistry*, 2015, **1053**, 238–244.
31 A. V. Powell, P. Vaqueiro, S. Tippireddy and J. Prado-Gonjal, *Nat Rev Chem*, 2025, **9**, 241–260.
32 S. K. Mishra, S. Satpathy and O. Jepsen, *J. Phys.: Condens. Matter*, 1997, **9**, 461–470.
33 M. Neuburger, *The bismuth telluride-bismuth selenide system*, Hughes, California, 1966, vol. 1966.
34 H. Koc, H. Ozisik, E. Deligöz, A. M. Mamedov and E. Ozbay, *J Mol Model*, 2014, **20**, 2180.
35 S. S. Hong, W. Kundhikanjana, J. J. Cha, K. Lai, D. Kong, S. Meister, M. A. Kelly, Z.-X. Shen and Y. Cui, *Nano Lett.*, 2010, **10**, 3118–3122.
36 M. Pazoki, M. B. Johansson, H. Zhu, P. Broqvist, T. Edvinsson, G. Boschloo and E. M. J. Johansson, *Journal of Physical Chemistry C*, 120 AD, 29039–46.
37 M. Pazoki and T. Edvinsson, *Sustainable Energy & Fuels*, 2018, **00**, 1–16.
38 D. J. Thouless, M. Kohmoto, M. P. Nightingale and M. Den Nijs, *Phys. Rev. Lett.*, 1982, **49**, 405–408.
39 Y. Ando, *arXiv*, 2023, preprint, arXiv:arXiv:2307.14196, DOI: 10.48550/arXiv.2307.14196.
40 A. Isaeva, B. Rasche and M. Ruck, *Physica Rapid Research Ltrs*, 2013, **7**, 39–49.
41 A. Isaeva and M. Ruck, *Inorg. Chem.*, 2020, **59**, 3437–3451.
42 Y. Zhang, K. He, C.-Z. Chang, C.-L. Song, L.-L. Wang, X. Chen, J.-F. Jia, Z. Fang, X. Dai, W.-Y. Shan, S.-Q. Shen, Q. Niu, X.-L. Qi, S.-C. Zhang, X.-C. Ma and Q.-K. Xue, *Nature Phys*, 2010, **6**, 584–588.
43 A. Ptok, K. J. Kapcia and A. Ciechan, *J. Phys.: Condens. Matter*, 2021, **33**, 065501.
44 D. Hsieh, Y. Xia, D. Qian, L. Wray, J. H. Dil, F. Meier, J. Osterwalder, L. Patthey, J. G. Checkelsky, N. P. Ong, A. V. Fedorov, H. Lin, A. Bansil, D. Grauer, Y. S. Hor, R. J. Cava and M. Z. Hasan, *Nature*, 2009, **460**, 1101–1105.

45 S.-Y. Xu, M. Neupane, C. Liu, D. Zhang, A. Richardella, L. Andrew Wray, N. Alidoust, M. Leandersson, T. Balasubramanian, J. Sánchez-Barriga, O. Rader, G. Landolt, B. Slomski, J. Hugo Dil, J. Osterwalder, T.-R. Chang, H.-T. Jeng, H. Lin, A. Bansil, N. Samarth and M. Zahid Hasan, *Nature Phys*, 2012, **8**, 616–622.
46 C. Hao, L. Wang, F. Wen, J. Xiang, L. Li, W. Hu and Z. Liu, *Nanotechnology*, 2018, **29**, 085401.
47 V. G. Bhide, B. A. Patki and A. S. Nigavekar, *Journal of Physics and Chemistry of Solids*, 1971, **32**, 1565–1571.
48 J. E. Moore, *Nature*, 2010, **464**, 194–198.
49 J. Moore, *Nature Phys*, 2009, **5**, 378–380.
50 M. Kohmoto, .
51 L. Fu and C. L. Kane, *Phys. Rev. B*, 2007, **76**, 045302.
52 Shun-Qing Shen, *Topological Insulators, Dirac equation in condensed matter*, Hong kong, vol. 2017.
53 D. N.- Ashcroft, Neil W, Mermin, *Solid State Physics*, Harcourt College Publishers, 1976.
54 J. J. Sakurai and S. F. Tuan, *Modern quantum mechanics*, Addison-Wesley, Reading (Mass.), rev. ed., 1994.
55 S. Chege, P. Ning'i, J. Sifuna and G. O. Amolo, *AIP Advances*, 2020, **10**, 095018.
56 C. L. Kane and E. J. Mele, *Phys. Rev. Lett.*, 2005, **95**, 226801.
57 H. Tang, X. Yan, Y. Xiong, K. Dou, Y. Zhao, J. Jie, X. Wang, Q. Fu, J. Yang, M. Lu and D. Xu, *npj Quant Mater*, 2019, **4**, 1.
58 A. Yu. Kuntsevich, A. A. Gabdullin, V. A. Prudkogliad, Yu. G. Selivanov, E. G. Chizhevskii and V. M. Pudalov, *Phys. Rev. B*, 2016, **94**, 235401.
59 J. Moon, J. Kim, N. Koirala, M. Salehi, D. Vanderbilt and S. Oh, *Nano Lett.*, 2019, **19**, 3409–3414.
60 shanna Zhu, dechao menv, genhao liang and kehui wu, *Nanoscale*, 2018, **10**, 10041–10049.
61 D. Kumar and A. Lakhani, *Materials Research Bulletin*, 2017, **88**, 127–130.
62 J. Moon, N. Koirala, M. Salehi, W. Zhang, W. Wu and S. Oh, *Nano Lett.*, 2018, **18**, 820–826.
63 R. Yu, W. Zhang, H.-J. Zhang, S.-C. Zhang, X. Dai and Z. Fang, *Science*, 2010, **329**, 61–64.
64 J. Yu, X. Zeng, L. Zhang, K. He, S. Cheng, Y. Lai, W. Huang, Y. Chen, C. Yin and Q. Xue, *Nano Lett.*, 2017, **17**, 7878–7885.
65 L. Fu and C. L. Kane, *Phys. Rev. B*, 2007, **76**, 045302.
66 H. Peng, K. Lai, D. Kong, S. Meister, Y. Chen, X.-L. Qi, S.-C. Zhang, Z.-X. Shen and Y. Cui, *Nature Mater*, 2010, **9**, 225–229.
67 J. Besbas, K. Banerjee, J. Son, Y. Wang, Y. Wu, M. Brahlek, N. Koirala, J. Moon, S. Oh and H. Yang, *Advanced Optical Materials*, 2016, **4**, 1642–1650.
68 M.-X. Wang, C. Liu, J.-P. Xu, F. Yang, L. Miao, M.-Y. Yao, C. L. Gao, C. Shen, X. Ma, X. Chen, Z.-A. Xu, Y. Liu, S.-C. Zhang, D. Qian, J.-F. Jia and Q.-K. Xue, *Science*, 2012, **336**, 52–55.
69 J. R. Williams, A. J. Bestwick, P. Gallagher, S. S. Hong, Y. Cui, A. S. Bleich, J. G. Analytis, I. R. Fisher and D. Goldhaber-Gordon, *Phys. Rev. Lett.*, 2012, **109**, 056803.
70 S. R. Lee, P. A. Sharma, A. L. Lima-Sharma, W. Pan and T. M. Nenoff, *Chem. Mater.*, 2019, **31**, 26–51.
71 A. Mercado, S. Sahoo and M. Franz, *Phys. Rev. Lett.*, 2022, **128**, 137002.
72 J.-P. Xu, M.-X. Wang, Z. L. Liu, J.-F. Ge, X. Yang, C. Liu, Z. A. Xu, D. Guan, C. L. Gao, D. Qian, Y. Liu, Q.-H. Wang, F.-C. Zhang, Q.-K. Xue and J.-F. Jia, *Phys. Rev. Lett.*, 2015, **114**, 017001.

View Article Online
DOI: 10.1039/D5MA00876J

73 A. Jain, Y. Shin and K. A. Persson, *Nat Rev Mater*, 2016, **1**, 15004.
74 B. Focassio, G. R. Schleder, F. C. de Lima, C. Lewenkopf and A. Fazzio, *Phys. Rev. B*, 2021, **104**, 214206.
75 D. Wu, J. Liu, R. Lian, G. Xu, K. Zhong, J.-M. Zhang and Z. Huang, *J. Phys.: Conf. Ser.*, 2017, **827**, 012007.
76 S. Koley and S. Basu, *Journal of Magnetism and Magnetic Materials*, 2020, **499**, 166294.
77 M. G. Vergniory, M. M. Otrokov, D. Thonig, M. Hoffmann, I. V. Maznichenko, M. Geilhufe, X. Zubizarreta, S. Ostanin, A. Marmodoro, J. Henk, W. Hergert, I. Mertig, E. V. Chulkov and A. Ernst, *Phys. Rev. B*, 2014, **89**, 165202.
78 S. Grimme, *J Comput Chem*, 2006, **27**, 1787–1799.
79 A. Ambrosetti, A. M. Reilly, R. A. DiStasio and A. Tkatchenko, *The Journal of Chemical Physics*, 2014, **140**, 18A508.
80 Z. Yu, L. Wang, Q. Hu, J. Zhao, S. Yan, K. Yang, S. Sinogeikin, G. Gu and H. Mao, *Sci Rep*, 2015, **5**, 15939.
81 M. Z. Mohyedin, N. A. Malik, M. F. M. Taib, M. Mustaffa, O. H. Hassan, A. M. M. Ali, B. U. Haq and M. Z. A. Yahya, *Computational Condensed Matter*, 2020, **25**, e00510.
82 A. Lawal and A. Shaari, *Mal. J. Fund. Appl. Sci.*, DOI:10.11113/mjfas.v12n3.424.
83 M. Jurczyszyn, M. Sikora, M. Chrobak and L. Jurczyszyn, *Applied Surface Science*, 2020, **528**, 146978.
84 H. Zhang, C.-X. Liu, X.-L. Qi, X. Dai, Z. Fang and S.-C. Zhang, *Nature Phys*, 2009, **5**, 438–442.
85 T. K. Reid, S. P. Alpay, A. V. Balatsky and S. K. Nayak, *Phys. Rev. B*, 2020, **101**, 085140.
86 Z.-H. Pan, E. Vescovo, A. V. Fedorov, D. Gardner, Y. S. Lee, S. Chu, G. D. Gu and T. Valla, *Phys. Rev. Lett.*, 2011, **106**, 257004.
87 K. Shirali, W. A. Shelton and I. Vekhter, *J. Phys.: Condens. Matter*, 2021, **33**, 035702.
88 S. V. Eremeev, M. G. Vergniory, T. V. Menshchikova, A. A. Shaposhnikov and E. V. Chulkov, *New J. Phys.*, 2012, **14**, 113030.
89 Y. V. Lysogorskiy, A. G. Kijamov, O. V. Nedopekin and D. A. Tayurskii, *J. Phys.: Conf. Ser.*, 2012, **394**, 012022.
90 B. Monserrat and D. Vanderbilt, *Phys. Rev. Lett.*, 2016, **117**, 226801.
91 A. Lawal, A. Shaari, R. ahmed, M. H. ALi and N. Jarkoni, 2017, 2017.
92 T. Ayadi, L. Debbichi, M. Badawi, M. Said, D. Rocca and S. Lebègue, *Applied Surface Science*, 2021, **538**, 148066.
93 W. Zhang, R. Yu, H.-J. Zhang, X. Dai and Z. Fang, *New J. Phys.*, 2010, **12**, 065013.
94 I. Grimaldi, D. Pacilè, S. V. Eremeev, O. De Luca, A. Policicchio, P. Moras, P. M. Sheverdyaeva, A. K. Kundu, Z. S. Aliev, P. Rudolf, R. G. Agostino, E. V. Chulkov and M. Papagno, *Phys. Rev. B*, 2020, **102**, 085118.
95 M. Michiardi, I. Aguilera, M. Bianchi, V. E. de Carvalho, L. O. Ladeira, N. G. Teixeira, E. A. Soares, C. Friedrich, S. Blügel and P. Hofmann, *Phys. Rev. B*, 2014, **90**, 075105.
96 S. Nakajima, *Journal of Physics and Chemistry of Solids*, 1963, **24**, 479–485.
97 V. V. Marchenkov, A. V. Lukoyanov, S. T. Baidak, A. N. Perevalova, B. M. Fominykh, S. V. Naumov and E. B. Marchenkova, *Micromachines*, 2023, **14**, 1888.
98 M. Eddrief, F. Vidal and B. Gallas, *J. Phys. D: Appl. Phys.*, 2016, **49**, 505304.
99 I. A. Nechaev, R. C. Hatch, M. Bianchi, D. Guan, C. Friedrich, I. Aguilera, J. L. Mi, B. B. Iversen, S. Blügel, P. Hofmann and E. V. Chulkov, *Phys. Rev. B*, 2013, **87**, 121111.
100 J. M. Crowley, J. Tahir-Kheli and W. A. Goddard, *J. Phys. Chem. Lett.*, 2015, **6**, 3792–3796.
101 S. A. Abolade, S. B. Akinpelu, D. O. Obada, S. Kumar R and A. Akande, *Results in Physics*, 2024, **64**, 107891.

View Article Online
DOI: 10.1039/D5MA00876J

102 Z. Wang, T. Lin, P. Wei, X. Liu, R. Dumas, K. Liu and J. Shi, *Applied Physics Letters*, 2010, **97**, 042112.
103 C. Fan, K. Sakamoto and P. Krüger, *Applied Surface Science*, 2024, **643**, 158699.
104 E. Uesugi, T. Uchiyama, H. Goto, H. Ota, T. Ueno, H. Fujiwara, K. Terashima, T. Yokoya, F. Matsui, J. Akimitsu, K. Kobayashi and Y. Kubozono, *Sci Rep*, 2019, **9**, 5376.
105 Y.-L. Wang, Y. Xu, Y.-P. Jiang, J.-W. Liu, C.-Z. Chang, M. Chen, Z. Li, C.-L. Song, L.-L. Wang, K. He, X. Chen, W.-H. Duan, Q.-K. Xue and X.-C. Ma, *Phys. Rev. B*, 2011, **84**, 075335.
106 P. Lostak, C. Drasar, I. Klichova, J. Navratil and T. Cernohorsk, *phys. stat. sol. (b)*, 1997, **200**, 289–296.
107 C. Kulsi, K. Kargupta, S. Ganguly and D. Banerjee, *Current Applied Physics*, 2017, **17**, 1609–1615.
108 K. Mazumder, A. Sharma, Y. Kumar, P. Bankar, M. A. More, R. Devan and P. M. Shirage, *Phys. Chem. Chem. Phys.*, 2018, **20**, 18429–18435.
109 G. R. Hyde, H. A. Beale and I. L. Spain, .
110 Y. H. Choi, N. H. Jo, K. J. Lee, H. W. Lee, Y. H. Jo, J. Kajino, T. Takabatake, K.-T. Ko, J.-H. Park and M. H. Jung, *Applied Physics Letters*, 2012, **101**, 152103.
111 A. Akrap, M. Tran, A. Ubaldini, J. Teyssier, E. Giannini, D. Van Der Marel, P. Lerch and C. C. Homes, *Phys. Rev. B*, 2012, **86**, 235207.
112 T. Uchiyama, H. Goto, E. Uesugi, A. Takai, L. Zhi, A. Miura, S. Hamao, R. Eguchi, H. Ota, K. Sugimoto, A. Fujiwara, F. Matsui, K. Kimura, K. Hayashi, T. Ueno, K. Kobayashi, J. Akimitsu and Y. Kubozono, *Sci Rep*, 2023, **13**, 537.
113 T. J. Jacobsson, M. Pazoki, A. Hagfeldt and T. Edvinsson, *JPCC*, 2015, **119**, 25673–25683.
114 M. Pazoki, T. J. Jacobsson, A. Hagfeldt and G. Boschloo, *Physical Review B*, 2016, **93**, 144105.
115 C. M. Acosta, M. P. Lima, A. J. R. da Silva, A. Fazzio and C. H. Lewenkopf, *Phys. Rev. B*, 2018, **98**, 035106.
116 M. Hasan and M. A. Majidi, *IOP Conf. Ser.: Mater. Sci. Eng.*, 2020, **902**, 012061.
117 J. Bouaziz, M. dos Santos Dias, J. Ibañez-Azpiroz and S. Lounis, *Phys. Rev. B*, 2018, **98**, 035119.
118 Z. Wang, Z.-G. Fu, S.-X. Wang and P. Zhang, *Phys. Rev. B*, 2010, **82**, 085429.
119 J. Burschka, N. Pellet, S.-J. Moon, R. Humphry-Baker, P. Gao, M. K. Nazeeruddin and M. Grätzel, *Nature*, 2013, **499**, 316–9.
120 M. Liu, F. Y. Liu, B. Y. Man, D. Bi and X. Y. Xu, *Applied Surface Science*, 2014, **317**, 257–261.
121 S. Razzaque, M. D. Khan, M. Aamir, M. Sohail, S. Bhoyate, R. K. Gupta, M. Sher, J. Akhtar and N. Revaprasadu, *Inorg. Chem.*, 2021, **60**, 1449–1461.
122 Y. Liu, L. Cao, J. Zhong, J. Yu, J. He and Z. Liu, *Journal of Applied Physics*, 2019, **125**, 035302.
123 B. Pradhan, A. Dalui, S. Paul, D. Roy and S. Acharya, *Mater. Res. Express*, 2020, **6**, 124005.
124 S. Liu, Z. Huang, H. Qiao, R. Hu, Q. Ma, K. Huang, H. Li and X. Qi, *Nanoscale Adv.*, 2020, **2**, 906–912.
125 C. S. Knox, M. T. Vaughan, N. R. Fox, A. Yagmur, S. Sasaki, J. E. Cunningham, E. H. Linfield, A. G. Davies and J. R. Freeman, *Nanophotonics*, 2024, **13**, 1843–1850.
126 D. Brito, A. Pérez-Rodriguez, I. Khatri, C. J. Tavares, M. Amado, E. Castro, E. Diez, S. Sadewasser and M. S. Claro, *Journal of Applied Physics*, 2022, **132**, 115107.
127 S.-K. Jerng, K. Joo, Y. Kim, S.-M. Yoon, J. H. Lee, M. Kim, J. S. Kim, E. Yoon, S.-H. Chun and Y. S. Kim, *Nanoscale*, 2013, **5**, 10618.

128 J. Y. Park, G.-H. Lee, J. Jo, A. K. Cheng, H. Yoon, K. Watanabe, T. Taniguchi, M. Kim, P. Kim and G.-C. Yi, *2D Mater.*, 2016, **3**, 035029.
129 K. S. Wickramasinghe, C. Forrester and M. C. Tamargo, *Crystals*, 2023, **13**, 677.
130 J. Liu, X. Yang, H. Xue, X. Gai, R. Sun, Y. Li, Z.-Z. Gong, N. Li, Z.-K. Xie, W. He, X.-Q. Zhang, D. Xue and Z.-H. Cheng, *Nat Commun*, 2023, **14**, 4424.
131 E. Wang, H. Ding, A. V. Fedorov, W. Yao, Z. Li, Y.-F. Lv, K. Zhao, L.-G. Zhang, Z. Xu, J. Schneeloch, R. Zhong, S.-H. Ji, L. Wang, K. He, X. Ma, G. Gu, H. Yao, Q.-K. Xue, X. Chen and S. Zhou, *Nature Phys*, 2013, **9**, 621–625.
132 G. Springholz, S. Wimmer, H. Groiss, M. Albu, F. Hofer, O. Caha, D. Kriegner, J. Stangl, G. Bauer and V. Holý, *Phys. Rev. Materials*, 2018, **2**, 054202.
133 Z. J. Li, Y. Liu, S. C. White, P. Wahl, X. M. Xie, M. H. Jiang and C. T. Lin, *Physics Procedia*, 2012, **36**, 638–643.
134 V. K. Maurya, C. L. Dong, C. L. Chen, K. Asokan and S. Patnaik, *Journal of Magnetism and Magnetic Materials*, 2018, **456**, 1–5.
135 P. Lošťák, J. Horák, J. Navrátil and J. Šrámková, *Phys. Stat. Sol. (a)*, 1993, **136**, K121–K125.
136 X. Hong, J. Shen, X. Tang, Y. Xie, M. Su, G. Tai, J. Yao, Y. Fu, J. Ji, X. Liu, J. Yang and D. Wei, *Optical Materials*, 2021, **117**, 111118.
137 M. Dc, J.-Y. Chen, T. Peterson, P. Sahu, B. Ma, N. Mousavi, R. Harjani and J.-P. Wang, *Nano Lett.*, 2019, **19**, 4836–4844.
138 M. A. Tumelero, M. B. Martins, P. B. Souza, R. D. Della Pace and A. A. Pasa, *Electrochimica Acta*, 2019, **300**, 357–362.
139 I. A. Mihailovic, K. Klösel and C. Hierold, *J. Micromech. Microeng.*, 2021, **31**, 095004.
140 H. Zhou, L. Che, Z. Guo, M. Wu, W. Li, W. Xu and L. Liu, *ACS Sustainable Chem. Eng.*, 2018, **6**, 4863–4870.
141 S. E. Friedensen, W. M. Parkin, J. T. Mlack and M. Drndić, *ACS Nano*, 2018, **12**, 6949–6955.
142 Y.-M. Hwang, C.-T. Pan, B.-S. Chen, P. H. Le, N. N. Uyen, L. T. C. Tuyen, V. Nguyen, C.-W. Luo, J.-Y. Juang, J. Leu and S.-R. Jian, *Coatings*, 2020, **10**, 958.
143 P. Orgiani, C. Bigi, P. Kumar Das, J. Fujii, R. Ciancio, B. Gobaut, A. Galdi, C. Sacco, L. Maritato, P. Torelli, G. Panaccione, I. Vobornik and G. Rossi, *Applied Physics Letters*, 2017, **110**, 171601.
144 B. R. Sankapal, R. S. Mane and C. D. Lokhande, .
145 R. Ahmed, Y. Xu, M. G. Sales, Q. Lin, S. McDonnell and G. Zangari, *J. Phys. Chem. C*, 2018, **122**, 12052–12060.
146 W. Zheng, T. Xie, Y. Zhou, Y. L. Chen, W. Jiang, S. Zhao, J. Wu, Y. Jing, Y. Wu, G. Chen, Y. Guo, J. Yin, S. Huang, H. Q. Xu, Z. Liu and H. Peng, *Nat Commun*, 2015, **6**, 6972.
147 H. Cui, H. Liu, X. Li, J. Wang, F. Han, X. Zhang and R. I. Boughton, *Journal of Solid State Chemistry*, 2004, **177**, 4001–4006.
148 Z. Ali, C. Cao, J. Li, Y. Wang, T. Cao, M. Tanveer, M. Tahir, F. Idrees and F. K. Butt, *Journal of Power Sources*, 2013, **229**, 216–222.
149 Y. Zhang, L. P. Hu, T. J. Zhu, J. Xie and X. B. Zhao, *Crystal Growth & Design*, 2013, **13**, 645–651.
150 S. K. Batabyal, C. Basu, A. R. Das and G. S. Sanyal, *Materials Letters*, 2006, **60**, 2582–2585.
151 H. Xu, G. Chen, R. Jin, D. Chen, Y. Wang, J. Pei, Y. Zhang, C. Yan and Z. Qiu, *CrystEngComm*, 2014, **16**, 3965–3970.
152 L. Zhu, K.-Y. Cho and W.-C. Oh, *Fullerenes, Nanotubes and Carbon Nanostructures*, 2016, **24**, 622–629.

153 M. Zhang, L. Lv, Z. Wei, C. Guo, X. Yang and Y. Zhao, *Materials Letters*, 2014, **123**, 87–89.
154 X. Wang, G. Dai, B. Liu, H. Zou, Y. Chen, X. Mo, X. Li, J. Sun, Y. Liu, Y. Liu and J. Yang, *Physica E: Low-dimensional Systems and Nanostructures*, 2019, **114**, 113620.
155 C.-C. Wang, F.-S. Shieu and H. C. Shih, *Nanomaterials*, 2021, **11**, 1352.
156 Y. Yan, Z.-M. Liao, F. Yu, H.-C. Wu, G. Jing, Z.-C. Yang, Q. Zhao and D. Yu, *Nanotechnology*, 2012, **23**, 305704.
157 L. D. Alegria and J. R. Petta, *Nanotechnology*, 2012, **23**, 435601.
158 W. Wang, X. Wang, N. Wang, X. Ning, H. Li, D. Lu, X. Liu, Q. Zhang and Y. Huang, *Nanoscale Res Lett*, 2018, **13**, 295.
159 S. Gautam, V. Aggarwal, B. Singh, V. P. S. Awana, R. Ganesan and S. S. Kushvaha, *Scientific Reports*.
160 J. Zhang, Z. Peng, A. Soni, Y. Zhao, Y. Xiong, B. Peng, J. Wang, M. S. Dresselhaus and Q. Xiong, *Nano Lett.*, 2011, **11**, 2407–2414.
161 D. Sharma, M. M. Sharma, R. S. Meena and V. P. S. Awana, *Physica B: Condensed Matter*, 2021, **600**, 412492.
162 J. Sánchez-Barriga, A. Varykhalov, J. Braun, S.-Y. Xu, N. Alidoust, O. Kornilov, J. Minár, K. Hummer, G. Springholz, G. Bauer, R. Schumann, L. V. Yashina, H. Ebert, M. Z. Hasan and O. Rader, *Phys. Rev. X*, 2014, **4**, 011046.
163 V. B. Nascimento, V. E. De Carvalho, R. Paniago, E. A. Soares, L. O. Ladeira and H. D. Pfannes, *Journal of Electron Spectroscopy and Related Phenomena*, 1999, **104**, 99–107.
164 L. V. Yashina, J. Sánchez-Barriga, M. R. Scholz, A. A. Volykhov, A. P. Sirotina, V. Neudachina S., M. E. Tamm, A. Varykhalov, D. Marchenko, G. Springholz, G. Bauer, A. Knop-Gericke and O. Rader, *ACS Nano*, 2013, **7**, 5181–5191.
165 Y. Zhao, Y. Lu, H. Li, Y. Zhu, Y. Meng, N. Li, D. Wang, F. Jiang, F. Mo, C. Long, Y. Guo, X. Li, Z. Huang, Q. Li, J. C. Ho, J. Fan, M. Sui, F. Chen, W. Zhu, W. Liu and C. Zhi, *Nat Commun*, 2022, **13**, 752.
166 T. Takahashi, T. Sagawa and H. Hamanaka, .
167 S. Tyagi, M. Dreyer, D. Bowen, D. Hinkel, P. J. Taylor, A. L. Friedman, R. E. Butera, C. Krafft and I. D. Mayergoyz, *IEEE Magn. Lett.*, 2021, **12**, 1–4.
168 R. Tao, Y.-J. Yan, X. Liu, Z.-W. Wang, Y. Ando, Q.-H. Wang, T. Zhang and D.-L. Feng, *Phys. Rev. X*, 2018, **8**, 041024.
169 R. Meija, V. Lazarenko, A. Skrastina, Y. Rublova, J. Andzane, V. Voikiva, A. Viksna and D. Erts, *Batteries*, 2022, **8**, 25.
170 K. Jacob John, B. Pradeep and E. Mathai, *Solid State Communications*, 1993, **85**, 879–881.
171 M. E. Kamminga, S. J. Cassidy, P. P. Jana, M. Elgaml, N. D. Kelly and S. J. Clarke, *Dalton Trans.*, 2021, **50**, 11376–11379.
172 L. Veyrat, F. Iacovella, J. Dufouleur, C. Nowka, H. Funke, M. Yang, W. Escoffier, M. Goiran, B. Eichler, O. G. Schmidt, B. Büchner, S. Hampel and R. Giraud, *Nano Lett.*, 2015, **15**, 7503–7507.
173 J.-D. Musah, X. Yanjun, A. M. Ilyas, T. G. Novak, S. Jeon, C. Arava, S. V. Novikov, D. S. Nikulin, W. Xu, L. Liu, A. Md, K.-H. Lam, X. Chen, C.-M. L. Wu and V. A. L. Roy, *ACS Appl. Mater. Interfaces*, 2019, **11**, 44026–44035.
174 T. Asaba, B. J. Lawson, C. Tinsman, L. Chen, P. Corbae, G. Li, Y. Qiu, Y. S. Hor, L. Fu and L. Li, *Phys. Rev. X*, 2017, **7**, 011009.
175 Y. Sun, H. Cheng, S. Gao, Q. Liu, Z. Sun, C. Xiao, C. Wu, S. Wei and Y. Xie, *J. Am. Chem. Soc.*, 2012, **134**, 20294–20297.
176 Q. Liu, S. S. Nanthakumar, B. Li, T. Cheng, F. Bittner, C. Ma, F. Ding, L. Zheng, B. Roth and X. Zhuang, *J. Phys. Chem. C*, 2024, **128**, 16265–16273.

177 R. E. Taylor, B. Leung, M. P. Lake and L.-S. Bouchard, *J. Phys. Chem. C*, 2012, **116**, 17300–17305.
178 P. Sharma, N. K. Tailor, S. K. Saini, K. Kumar, M. Kumar, L. Goswami, R. Srivastava, T. Sharma, S. Choudhary and S. Satapathi, *ACS Appl. Electron. Mater.*, 2024, acsaelm.4c01135.
179 V. S. Kamboj, A. Singh, T. Ferrus, H. E. Beere, L. B. Duffy, T. Hesjedal, C. H. W. Barnes and D. A. Ritchie, *ACS Photonics*, 2017, **4**, 2711–2718.
180 Y. Zheng, T. Xu, X. Wang, B. Han and Z. Sun, *Crystal Growth & Design*, 2024, **24**, 6583–6591.
181 E. J. Winder, A. B. Ellis and G. C. Lisensky, *J. Chem. Educ.*, 1996, **73**, 940.
182 S. Cho, N. P. Butch, J. Paglione and M. S. Fuhrer, *Nano Lett.*, 2011, **11**, 1925–1927.
183 Y. Sun, S. Kittaka, T. Sakakibara, K. Machida, J. Wang, J. Wen, X. Xing, Z. Shi and T. Tamegai, *Phys. Rev. Lett.*, 2019, **123**, 027002.
184 S. N. Shirodkar, G. M. Stephen, A. T. Hanbicki, A. L. Friedman and P. Dev, *J. Phys. Chem. C*, 2022, **126**, 16877–16884.
185 L. A. Walsh, A. J. Green, R. Addou, W. Nolting, C. R. Cormier, A. T. Barton, T. R. Mowll, R. Yue, N. Lu, J. Kim, M. J. Kim, V. P. LaBella, C. A. Ventrice, S. McDonnell, W. G. Vandenberghe, R. M. Wallace, A. Diebold and C. L. Hinkle, *ACS Nano*, 2018, **12**, 6310–6318.
186 Y. Xiong, G. Zhou, N.-C. Lai, X. Wang, Y.-C. Lu, O. V. Prezhdo and D. Xu, *ACS Nano*, 2021, **15**, 2791–2799.
187 Y. Huang, J. D. Querales-Flores, S. W. Teitelbaum, J. Cao, T. Henighan, H. Liu, M. Jiang, G. De La Peña, V. Krapivin, J. Haber, T. Sato, M. Chollet, D. Zhu, T. Katayama, R. Power, M. Allen, C. R. Rotundu, T. P. Bailey, C. Uher, M. Trigo, P. S. Kirchmann, É. D. Murray, Z.-X. Shen, I. Savić, S. Fahy, J. A. Sobota and D. A. Reis, *Phys. Rev. X*, 2023, **13**, 041050.
188 S.-D. Yang, L. Yang, Y.-X. Zheng, W.-J. Zhou, M.-Y. Gao, S.-Y. Wang, R.-J. Zhang and L.-Y. Chen, *ACS Appl. Mater. Interfaces*, 2017, **9**, 29295–29301.
189 J. Yang, B. Zheng, Z. Chen, W. Xu, R. Wang and H. Xu, *J. Phys. Chem. C*, 2020, **124**, 6253–6259.
190 T. Li, B. Li, Y. Yang, Z. Jin, Z. Zhang, P. Wang, L. Deng, Y. Zhan, Q. Zhang and J. Liang, *Nat Commun*, 2024, **15**, 9435.
191 P. H. R. Gonçalves, T. Chagas, V. B. Nascimento, D. D. Dos Reis, C. Parra, M. S. C. Mazzoni, Â. Malachias and R. Magalhães-Paniago, *J. Phys. Chem. Lett.*, 2018, **9**, 954–960.
192 L. E. Dresselhaus-Marais, B. Kozioziemski, T. S. Holstad, T. M. Ræder, M. Seaberg, D. Nam, S. Kim, S. Breckling, S. Choi, M. Chollet, P. K. Cook, E. Folsom, E. Galtier, A. Gonzalez, T. Gorkhover, S. Guillet, K. Haldrup, M. Howard, K. Katagiri, S. Kim, S. Kim, S. Kim, H. Kim, E. B. Knudsen, S. Kuschel, H. J. Lee, C. Lin, R. S. McWilliams, B. Nagler, M. M. Nielsen, N. Ozaki, D. Pal, R. Pablo Pedro, A. M. Saunders, F. Schoofs, T. Sekine, H. Simons, T. Van Driel, B. Wang, W. Yang, C. Yildirim, H. F. Poulsen and J. H. Eggert, *Sci Rep*, 2023, **13**, 17573.
193 Z. Bielecki, K. Achtenberg, M. Kopytko, J. Mikołajczyk, J. Wojtas and A. Rogalski, *Bulletin of the Polish Academy of Sciences Technical Sciences*, 2022, 140534–140534.
194 W. Si, W. Zhou, X. Liu, K. Wang, Y. Liao, F. Yan and X. Ji, *Micromachines*, 2024, **15**, 427.
195 H. Zhang, X. Zhang, C. Liu, S.-T. Lee and J. Jie, *ACS Nano*, 2016, **10**, 5113–5122.
196 F. Wang, P. Luo, Y. Zhang, Y. Huang, Q. Zhang, Y. Li and T. Zhai, *Sci. China Mater.*, 2020, **63**, 1537–1547.

197 X. Wang, Y. Tang, W. Wang, H. Zhao, Y. Song, C. Kang and K. Wang, *Nanomaterials*, 2022, **12**, 1824.
198 A. Sharma, B. Bhattacharyya, A. K. Srivastava, T. D. Senguttuvan and S. Husale, *Sci Rep*, 2016, **6**, 19138.
199 J. L. Liu, H. Chen, X. Li, H. Wang, Z. K. Zhang, W. W. Pan, G. Yuan, C. L. Yuan, Y. L. Ren and W. Lei, *Journal of Alloys and Compounds*, 2020, **818**, 152819.
200 M. Yang, Q. Han, X. Liu, J. Han, Y. Zhao, L. He, J. Gou, Z. Wu, X. Wang and J. Wang, *Adv Funct Materials*, 2020, **30**, 1909659.
201 B. Das, N. S. Das, S. Sarkar, B. K. Chatterjee and K. K. Chattopadhyay, *ACS Appl. Mater. Interfaces*, 2017, **9**, 22788–22798.
202 M. Li, Z. Wang, X. P. A. Gao and Z. Zhang, *J. Phys. Chem. C*, 2020, **124**, 10135–10142.
203 C. Lu, M. Luo, W. Dong, Y. Ge, T. Han, Y. Liu, X. Xue, N. Ma, Y. Huang, Y. Zhou and X. Xu, *Advanced Science*, 2023, **10**, 2205460.
204 W. Tang, A. Politano, C. Guo, W. Guo, C. Liu, L. Wang, X. Chen and W. Lu, *Adv Funct Materials*, 2018, **28**, 1801786.
205 F. Wang, L. Li, W. Huang, L. Li, B. Jin, H. Li and T. Zhai, *Adv Funct Materials*, 2018, **28**, 1802707.
206 W. Huang, C. Xing, Y. Wang, Z. Li, L. Wu, D. Ma, X. Dai, Y. Xiang, J. Li, D. Fan and H. Zhang, *Nanoscale*, 2018, **10**, 2404–2412.
207 C. Zang, X. Qi, L. Ren, G. Hao, Y. Liu, J. Li and J. Zhong, *Applied Surface Science*, 2014, **316**, 341–347.
208 C. Liu, H. Zhang, Z. Sun, K. Ding, J. Mao, Z. Shao and J. Jie, *J. Mater. Chem. C*, 2016, **4**, 5648–5655.
209 X. Wang, G. Dai, B. Liu, H. Zou, Y. Chen, X. Mo, X. Li, J. Sun, Y. Liu, Y. Liu and J. Yang, *Physica E: Low-dimensional Systems and Nanostructures*, 2019, **114**, 113620.
210 J. Han, Z. Fu, J. Wei, S. Han, W. Deng, F. Hu, Z. Wang, H. Zhou, H. Yu, J. Gou and J. Wang, *Light Sci Appl*, 2025, **14**, 362.
211 Z. Yan, H. Yang, Z. Yang, C. Ji, G. Zhang, Y. Tu, G. Du, S. Cai and S. Lin, *Small*, 2022, **18**, 2200016.
212 Z. Zeng, D.-B. Wang, X. Fang, J.-M. Cao, B.-K. Zhang, J.-W. Pan, D.-H. Liu, S.-H. Liu, S.-J. Jiao, T.-Y. Chen, G. Liu, L.-C. Zhao and J.-Z. Wang, *Rare Met.*, 2024, **43**, 2349–2370.
213 J. Ghosh, P. Priyadarshini, Z. T. Younus, Q. Jia, W. Nie, J. L. MacManus-Driscoll and R. L. Z. Hoye, *MRS Energy & Sustainability*, 2025, **12**, 233–253.
214 P. Deorani, J. Son, K. Banerjee, N. Koirala, M. Brahlek, S. Oh and H. Yang, *Phys. Rev. B*, 2014, **90**, 094403.
215 P. Kumar, R. Kumar, S. Kumar, M. K. Khanna, R. Kumar, V. Kumar and A. Gupta, *Magnetochemistry*, 2023, **9**, 73.
216 J. A. Krieger, Y. Ou, M. Caputo, A. Chikina, M. Döbeli, M.-A. Husanu, I. Keren, T. Prokscha, A. Suter, C.-Z. Chang, J. S. Moodera, V. N. Strocov and Z. Salman, *Phys. Rev. B*, 2019, **99**, 064423.
217 H. Wu, A. Chen, P. Zhang, H. He, J. Nance, C. Guo, J. Sasaki, T. Shirokura, P. N. Hai, B. Fang, S. A. Razavi, K. Wong, Y. Wen, Y. Ma, G. Yu, G. P. Carman, X. Han, X. Zhang and K. L. Wang, *Nat Commun*, 2021, **12**, 6251.
218 C. Jozwiak, J. A. Sobota, K. Gotlieb, A. F. Kemper, C. R. Rotundu, R. J. Birgeneau, Z. Hussain, D.-H. Lee, Z.-X. Shen and A. Lanzara, *Nat Commun*, 2016, **7**, 13143.
219 A. R. Mellnik, J. S. Lee, A. Richardella, J. L. Grab, P. J. Mintun, M. H. Fischer, A. Vaezi, A. Manchon, E.-A. Kim, N. Samarth and D. C. Ralph, *Nature*, 2014, **511**, 449–451.
220 S. Abhirami, E. P. Amaladass, K. Saravanan, C. David, S. Amirthapandian, R. M. Sarguna and A. Mani, *Journal of Alloys and Compounds*, 2021, **885**, 161145.

221 C. H. Li, O. M. J. Van 'T Erve, J. T. Robinson, Y. Liu, L. Li and B. T. Jonker, *Nature Nanotech*, 2014, **9**, 218–224.
222 W. Han, *APL Materials*, 2016, **4**, 032401.
223 M. He, H. Sun and Q. L. He, *Front. Phys.*, 2019, **14**, 43401.
224 Y. Ando, *J. Phys. Soc. Jpn.*, 2013, **82**, 102001.
225 Y. Liu and Q. Shao, *ACS Nano*, 2020, **14**, 9389–9407.
226 J. Han, A. Richardella, S. A. Siddiqui, J. Finley, N. Samarth and L. Liu, *Phys. Rev. Lett.*, 2017, **119**, 077702.
227 M. Dc, R. Grassi, J.-Y. Chen, M. Jamali, D. Reifsnyder Hickey, D. Zhang, Z. Zhao, H. Li, P. Quarterman, Y. Lv, M. Li, A. Manchon, K. A. Mkhoyan, T. Low and J.-P. Wang, *Nature Mater*, 2018, **17**, 800–807.
228 W. Liu, D. West, L. He, Y. Xu, J. Liu, K. Wang, Y. Wang, G. Van Der Laan, R. Zhang, S. Zhang and Kang. L. Wang, *ACS Nano*, 2015, **9**, 10237–10243.
229 J. Moon, J. Kim, N. Koirala, M. Salehi, D. Vanderbilt and S. Oh, *Nano Lett.*, 2019, **19**, 3409–3414.
230 Abasaheb Garware Arts and Science College, Pune 411 004, A. T. Supekar, P. K. Bhujbal, S. A. Salunke, S. M. Rathod, Abasaheb Garware Arts and Science College, Pune 411 004, S. P. Patole and H. M. Pathan, *ES Energy Environ.*, DOI:10.30919/esee8c848.
231 B. Xu, G. Wang and H. Fu, *Sci Rep*, 2016, **6**, 23395.
232 E. Singh, K. S. Kim, G. Y. Yeom and H. S. Nalwa, *RSC Adv.*, 2017, **7**, 28234–28290.
233 A. Abdolhay, A. Kashaninia and M. Banihashemi, *IET Optoelectronics*, 2023, **17**, 61–69.
234 M. Wang, Q. Fu, L. Yan, W. Pi, G. Wang, Z. Zheng and W. Luo, *ACS Appl. Mater. Interfaces*, 2019, **11**, 47868–47877.
235 D.-B. Li, L. Hu, Y. Xie, G. Niu, T. Liu, Y. Zhou, L. Gao, B. Yang and J. Tang, *ACS Photonics*, 2016, **3**, 2122–2128.
236 Z. Yuan, Z. Wu, S. Bai, W. Cui, J. Liu, T. Song and B. Sun, *Organic Electronics*, 2015, **26**, 327–333.
237 M. A. Saifee, U. Latief, J. Ali and Mohd. S. Khan, *Discov Energy*, 2024, **4**, 4.
238 S. Zhao, Z. Wang, L. Ye, H. Yan, J. Han and H. Lin, *ACS Appl. Energy Mater.*, 2024, **7**, 10155–10162.
239 X. Zhao, C. Zhang, G. Yang, Y. Wu, Q. Fu, H. Zhao and Y. Lei, *Inorg. Chem. Front.*, 2021, **8**, 4267–4275.
240 T. Yang, J. Liu, D. Yang, Q. Mao, J. Zhong, Y. Yuan, X. Li, X. Zheng, Z. Ji, H. Liu, G. Wang and R. Zheng, *ACS Appl. Energy Mater.*, 2020, **3**, 11073–11081.
241 P. Kumari, R. Singh, K. Awasthi, T. Ichikawa, M. Kumar and A. Jain, *Journal of Alloys and Compounds*, 2020, **838**, 155403.
242 G. Han, Z.-G. Chen, D. Ye, L. Yang, L. Wang, J. Drennan and J. Zou, *J. Mater. Chem. A*, 2014, **2**, 7109.
243 F. Mao, J. Guo, S. Zhang, F. Yang, Q. Sun, J. Ma and Z. Li, *RSC Adv.*, 2016, **6**, 38228–38232.
244 D. Li, J. Zhou, X. Chen and H. Song, *ACS Appl. Mater. Interfaces*, 2018, **10**, 30379–30387.
245 Z. Zou, Z. Yu, C. Chen, Q. Wang, K. Zhu, K. Ye, G. Wang, D. Cao and J. Yan, *ACS Nano*, 2023, **17**, 13769–13783.
246 Y. Zhu, Y. Wu, J. Zhao, X. Zeng, J. Mao and J. Chen, *Sustainability*, 2023, **15**, 16210.
247 M. Ni, M. Leung, D. Leung and K. Sumathy, *Solar Energy Materials and Solar Cells*, 2006, **90**, 2000–2009.
248 F. Zhu, H. Shi, C. Wang, X. Zhou, X. Zhang and F. Yang, *Sensors and Actuators B: Chemical*, 2021, **332**, 129454.

View Article Online
DOI: 10.1039/D5MA00876J

249 A. D. Savariraj, V. Vinoth, R. V. Mangalaraja, T. Arun, D. Contreras, A. Akbari-Fakhrabadi, H. Valdés and F. Banat, *Journal of Electroanalytical Chemistry*, 2020, **856**, 113629.
250 L. Xiao, A. Zhu, Q. Xu, Y. Chen, J. Xu and J. Weng, *ACS Appl. Mater. Interfaces*, 2017, **9**, 6931–6940.
251 Z. Wang, J. Dai, J. Wang, X. Li, C. Pei, Y. Liu, J. Yan, L. Wang, S. Li, H. Li, X. Wang, X. Huang and W. Huang, *Research*, 2022, **2022**, 2022/9767651.
252 B. Du, W. Kang, Y. He, Y. Wang, X. Yang, G. Meng, Z. Zhu, X. Lin, Y. Tan, C. Liang, X. Guo, J. Jian, Y. Guo and M. Zhou, *iScience*, 2023, **26**, 106387.
253 S. Yi, C. Chen, M. Yu, J. Hao and Y. Wang, *Front. Chem.*, 2024, **12**, 1425693.
254 T.-S. Jiang, X.-Y. Li, C.-H. Zhu and H.-Q. Zhao, *Advanced Agrochem*, 2024, S2773237123001041.
255 T. A. Nasser, R. Adel, A. Badr, M. Teleb, A. A. Bekhit, K. A. Elkhodairy, A. S. Abdelhamid and A. O. Elzoghby, *ACS Omega*, 2023, **8**, 4491–4507.
256 Z. Li, J. Liu, Y. Hu, K. A. Howard, Z. Li, X. Fan, M. Chang, Y. Sun, F. Besenbacher, C. Chen and M. Yu, *ACS Nano*, 2016, **10**, 9646–9658.
257 Z. Guo, Y. Liu, H. Zhou, K. Zheng, D. Wang, M. Jia, P. Xu, K. Ma, C. Cui and L. Wang, *Colloids and Surfaces B: Biointerfaces*, 2019, **184**, 110546.
258 J. Yao, T. Muñoz-Ortiz, F. Sanz-Rodríguez, E. Martín Rodríguez, D. H. Ortgies, J. García Solé, D. Jaque and R. Marin, *ACS Photonics*, 2022, **9**, 559–566.
259 F. Mao, L. Wen, C. Sun, S. Zhang, G. Wang, J. Zeng, Y. Wang, J. Ma, M. Gao and Z. Li, *ACS Nano*, 2016, **10**, 11145–11155.
260 J. Li, F. Jiang, B. Yang, X.-R. Song, Y. Liu, H.-H. Yang, D.-R. Cao, W.-R. Shi and G.-N. Chen, *Sci Rep*, 2013, **3**, 1998.
261 Y. Yao, P. Li, J. He, D. Wang, J. Hu and X. Yang, *ACS Appl. Mater. Interfaces*, 2021, **13**, 28650–28661.
262 H. Zhao, L. Li, J. Zhang, C. Zheng, K. Ding, H. Xiao, L. Wang and Z. Zhang, *ACS Appl. Mater. Interfaces*, 2018, **10**, 31124–31135.
263 Q. Wang, J. Du, R. Ouyang, B. Liu, Y. Miao and Y. Li, *Coordination Chemistry Reviews*, 2023, **492**, 215281.
264 N. Shukla, A. K. Singh, Kavita, D. K. Verma, B. Kumar, J. L. Maurya, D. Tiwary and R. B. Rastogi, *ACS Appl. Eng. Mater.*, 2023, **1**, 1322–1334.
265 P. Subramanyam, B. Meena, D. Suryakala and C. Subrahmanyam, *ACS Appl. Nano Mater.*, 2021, **4**, 739–745.
266 J. Kosmaca, J. Andzane, M. Baitimirova, F. Lombardi and D. Erts, *ACS Appl. Mater. Interfaces*, 2016, **8**, 12257–12262.
267 T. Jia, L. Yang, J. Zhang, H. Kimura, H. Zhao, Q. Guo and Z. Cheng, *Nanomaterials*, 2023, **13**, 2504.
268 V. Mishra, V. Baranwal, R. K. Mishra, S. Sharma, B. Paul and A. C. Pandey, *Sci Rep*, 2017, **7**, 18032.
269 A. Nowak-Terpiłowska, M. Akhtar, G. Hussain, A. Piasecki, P. Błaszkiewicz, M. Tuliński, E. Wolarz, T. Karpiński and M. L. Wyganowska, *Sci Rep*, 2025, **15**, 21741.
270 B. Sun, G. Xu, Z. Yang, C. Guan, X. Ji, S. Chen, X. Chen, Y. Ma and J. Feng, *Microsyst Nanoeng*, 2025, **11**, 31.
271 D. Kim, J. Seo, S. Yer, S. Baek, W. Cho, S. Zheng, Y.-H. Kim, M. Zhao and H. Yang, *Nat Commun*, 2025, **16**, 1879.
272 J. Stensberg, X. Han, Z. Ni, X. Yao, X. Yuan, D. Mallick, A. Gandhi, S. Oh and L. Wu, *Phys. Rev. B*, 2024, **109**, 245112.
273 L. Maisel Licerán, F. García Flórez, L. D. A. Siebbeles and H. T. C. Stoof, *Sci Rep*, 2023, **13**, 6337.

274 I. Mucha and W. Gawel, *Sci Rep*, 2024, **14**, 29009.

View Article Online
DOI: 10.1039/D5MA00876J